A STUDY OF AIR-OIL TWO-PHASE FLOW IN A
HORIZONTAL STRAIGHT PIPE

BY

JENNIFER L. PAWLOSKI,
B.Eng.Socty.

AIR-OIL TWO-PHASE FLOW IN A

HORIZONTAL STRAIGHT PIPE

A STUDY OF AIR-OIL TWO-PHASE FLOW IN A HORIZONTAL STRAIGHT PIPE

By

Jennifer L. Pawloski, B.Eng.Socty

A Thesis

Submitted to the School of Graduate Studies

In Partial Fulfillment of the Requirements

for the Degree

Masters of Engineering

McMaster University

Hamilton, Ontario, Canada

MASTER OF ENGINEERING (2001)   McMaster University
(Mechanical Engineering)   Hamilton, Ontario

TITLE: A Study of Air-Oil Two-Phase Flow in a Horizontal

                   Straight Pipe

AUTHOR: Jennifer L. Pawloski, B.Eng.Scty. (McMaster University)

SUPERVISOR: Dr. C. Ching and Dr. M. Shoukri

NUMBER OF PAGES: xv, 118

ABSTRACT

Air-oil flows are found in many industrial applications, including lubrication systems for high-speed machining and jet engines. Understanding the interaction of the two phases, and the effect flow characteristics have on pressure drop, are important to design lubrication systems. Applying pressure drop models without taking flow regime into account has been shown to result in large prediction errors.

The overall objective of this research is to gain a better understanding of air-oil two-phase flow in a ½" ID horizontal straight pipe. The two key goals are to correct flow regime identification and pressure drop predictions. A new air-oil two-phase experimental facility was designed and commissioned. The facility can accommodate multiple test section geometries. Pressure drops for a wide range of test conditions were measured. Flow regimes were identified with the aid of a high-speed video camera.

A capacitance sensor was developed to measure instantaneous void fraction and to obtain useful information to identify flow regimes. Three existing flow regime maps used for identification were evaluated using the current air-oil data. Significant errors in the prediction of the transitional boundaries of these maps were found. Corrections to the transitional boundaries to improve the overall prediction accuracy of the maps are suggested. The Mandhane et. al. (1974) flow regime map with suggested corrections was found to most accurately predict the transitional boundaries.

Several existing pressure drop models were evaluated with data from the new test facility. The Chisholm (1973) and Martinelli (1948) models were found to have the highest accuracy with ±40% RMSE. A correction factor was applied to the Martinelli model, resulting in ±19% RMSE. Recommendations on the appropriate model for each identified flow regime are also made. Particular attention is paid to the prediction of pressure drop in the mist flow regime, due to the industrial applications of the regime.

ACKNOWLEDGEMENTS

TABLE OF CONTENTS

LIST OF TABLES

LIST OF FIGURES

NOMECLATURE

English (SI)

A   cross-sectional area (m^2)

B   Baroczy variable

C   Chisholm coefficient

A_p plate area (m^2)

C_{ap} Capacitance (pF)

C_R coefficient of resistance

d   tube inner diameter (m)

d_p distance between plates (m)

dP   pressure drop (N/m^2)

dz   length over which pressure drop is measured (m)

E   Friedel equation variable.

e   error

F   Taitel and Dukler parameter

Fr   Froud number

f   frequency

f friction factor

g   gravity (m/s^2)

G   mass flux ($kg/m^2.s$)

H   Friedel equation variable

j   superficial velocity (m/s)

K	Taitel and Dukler parameter
K_2	Martinelli and Chawla variable
k	roughness factor
l	length (m)
M	Mandhane correction variable
$\overset{\circ}{m}$	mass flow rate (kg/s)
n	Olujic variable
P	pressure (N/m^2)
Q	volume flow rate (m^3/s)
R	density ratio
Re	Reynolds number
u	phase velocity (m/s)
s	slip ratio
T	Taitel and Dukler parameter
t	instantaneous time (s)
V	velocity (m/s)
We	Weber number
X	Martinelli number
$\overset{\cdot}{X}$	Mandhane plotting parameter
$\overset{\cdot}{Y}$	Mandhane plotting parameter

Subscript

air	air properties
F	friction
G	gravitational
g	gas phase
go	gas only
H	homogenous
H_2O	water properties
i	phase
l	liquid phase
lo	liquid only
M	momentum
R	resistance
SG	superficial gas
TP	two phase

Greek

λ	Baker map plotting parameter
Ψ	Baker map plotting parameter
ρ	density (kg/m^3)

σ surface tension (N/m)

μ viscosity (Pa.s)

α void fraction

φ two-phase multiplier

β volume flow rate ratio

θ viscosity ratio

ε Olujic variable

Γ_o Olujic variable

Γ_c Chisholm variable

ε_o permitivity free space

κ dielectric constant

τ time (s)

Flow Regimes

A   annular

BTS   blow through slug

D   dispersed

F   froth

FS   foam slug

M   mist

P   plug

S   slug

SBZ   slug building zone

ST   stratified

W   wavy

Chapter One: Introduction

Air-oil two-phase flows are encountered in many industries, including oil and gas production, automotive, and aerospace. In the oil and gas industry, numerous flow conditions can be encountered, affecting the efficiency of pumps and other instrumentation on the pipelines. To avoid failure of equipment, maximizing production and efficiency while minimizing cost, there is a need to accurately identify the flow regimes encountered and predict pressure losses (Baker et. al., 1988). Many high-speed machining applications use oil droplets suspended in air (mist flow) as a lubrication technique. Small quantities of oil are introduced into a constant air flow by one of two methods (Figures 1.1 and 1.2) and are carried to lubrication points (Figure 1.3) (Schrama, 1993). The compressed air both pressurizes the bearing cavity, preventing contaminants from reaching the moving surfaces, and cools it (Schrama, 1993). A similar technique is used for lubrication of aero engine bearing chambers. High-speed air flow is used to pressurize the chamber, leading to entrainment of oil droplets in the air stream (Glahn and Wittig, 1996). To maximize performance of the engine, the oil must be separated from the air, and the air returned to the main air stream (Glahn et. al., 1996). The design of such systems requires knowledge of the air-oil flow characteristics to predict the pressure losses in the oil separation system.

A wide range of flow conditions are encountered in industrial air-oil two-phase flow applications, however, the majority of current two-phase flow data is based on air-water flows. There is a need for a comprehensive study of air-oil two-phase flow over a

1
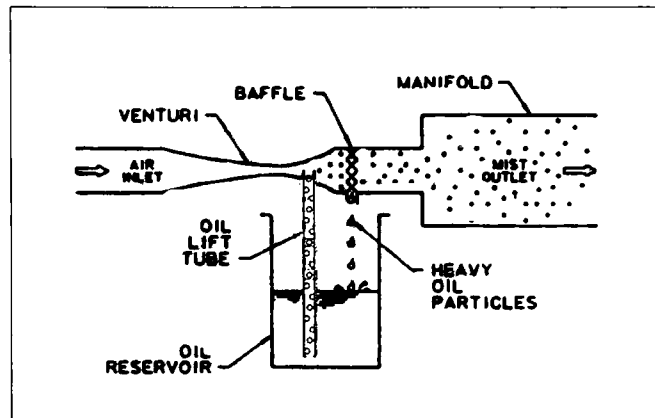
Figure 1.1: Oil Mist Flow Application (Schrama, 1993)
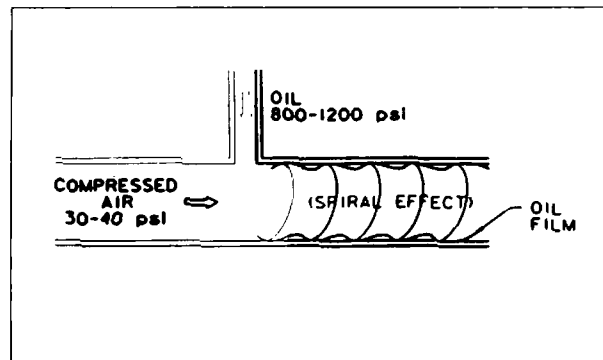
Figure 1.2: Air-Oil Flow Application (Schrama, 1993)

wide range of flow conditions and test geometries. Such a project is beyond the scope of this thesis; however, as a first step the study of air-oil two-phase flow in a horizontal straight pipe is studied.

Two areas of importance are the identification of the flow regimes and the prediction of pressure losses under different flow conditions. Existing data for air-oil two-phase flow regimes suggest that many of the flow regimes encountered are different in appearance than as defined for air-water two-phase flow (Schrama, 1993). This leads
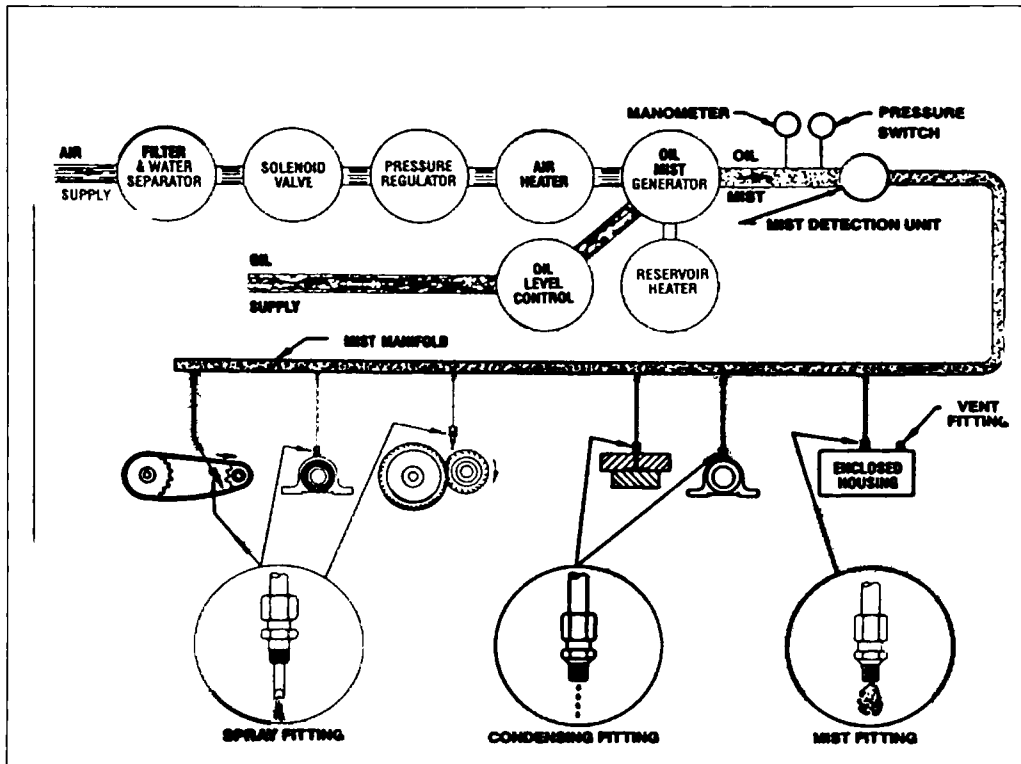
Figure 1.3: Example of Oil Mist Lubrication System (Schrama, 1993)

to increased difficulty in visual identification of flow regimes. Hence, there is a need to review current methods of flow regime identification and prediction for air-oil two-phase flow. The development of proper instrumentation and inversion algorithms to objectively identify the flow regimes will greatly facilitate the modeling of these flows. Pressure drop in two-phase flow has been shown to be dependent on the flow regime by many researchers, suggesting a review of common pressure drop prediction models is warranted. Pressure drop models for the mist flow regime are specifically examined, as this flow regime is commonly encountered in industry but is not often examined in the literature.

1.1 Overview Of The Thesis

This thesis represents the first phase of an extensive investigation of air-oil two-phase flow in the McMaster University Two-Phase Flow Laboratory. A significant effort was devoted to the design, construction, and development of the test facility and instrumentation. Identification of flow regimes using high-speed video observations and capacitance sensor measurements of instantaneous void fraction were investigated. One of the key motivations for the research is to develop effective pressure drop models for air-oil flow. Additionally, the ability of prominent frictional pressure drop models to predict pressure losses in the mist flow regime are examined due to the use of this regime within many industrial applications.

1.2 Project Objectives

The overall goal of this study is twofold: to make recommendations on the use of pressure drop prediction models for the mist flow regime, and to present introductory information and data for use in future air-oil two-phase studies in the McMaster Two-Phase Flow Laboratory.

The specific objectives of the present research are as follows:

1) Design and construct an air-oil two-phase experimental facility capable of supporting multiple test section geometries and producing a wide range of flow conditions.

2) Develop instantaneous void fraction measurement techniques for flow regime identification.

3) Evaluate existing techniques for flow regime prediction for air-oil two-phase flow.

4) Evaluate current two-phase pressure drop models and develop a pressure drop model for air-oil two-phase flow.

5) Evaluate pressure drop models for the mist flow regime.

1.3 Organization of Thesis

This thesis consists of eight chapters. Chapters 2 and 3 present comprehensive reviews of two-phase flow regime prediction and pressure drop prediction methods, respectively. An overview of the air-oil two-phase research facility designed and constructed for the project is presented in Chapter 4. The development of the capacitance sensor for instantaneous void fraction measurement and flow regime identification is detailed in Chapter 5. Results for the flow regime predictive maps are presented in Chapter 6, with recommendations for improving the accuracy of the transition boundaries. Similarly, Chapter 7 presents the frictional pressure drop model results. Several models are evaluated for all flow regimes and specifically for the mist flow regime. A preliminary suggestion for use of the models based on flow regime is made. Finally, Chapter 8 summarizes the results presented in earlier chapters and provides conclusions and recommendations for future research.

Chapter Two: Two-Phase Flow Regimes and Flow Maps

This chapter provides an introduction to the definition and identification of two-phase flow regimes. The definitions used for the current air-oil research are discussed. Flow regime maps, a predictive technique, are then introduced and three specific maps are selected for study.

2.1 Two-Phase Flow Regimes

In two-phase flow, the distinct distribution of the phases as they travel along a channel is called a flow regime. The properties and relative flow rates of the two phases determine the flow regime. Despite the complexity of gas/liquid flows in horizontal straight pipes, six major types of flow regimes have been identified: dispersed, plug, stratified, wavy, slug and annular (Whalley, 1990). As the relative gas and liquid flow rates increases, the flow transitions between regimes as identified in Figure 2.1.
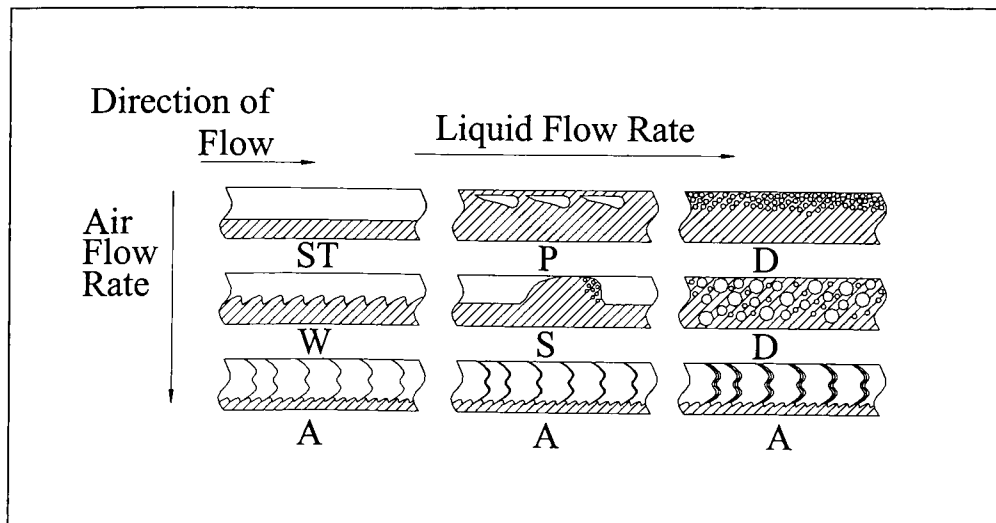
Figure 2.1: Flow Regimes in Horizontal Flow in Pipes

6
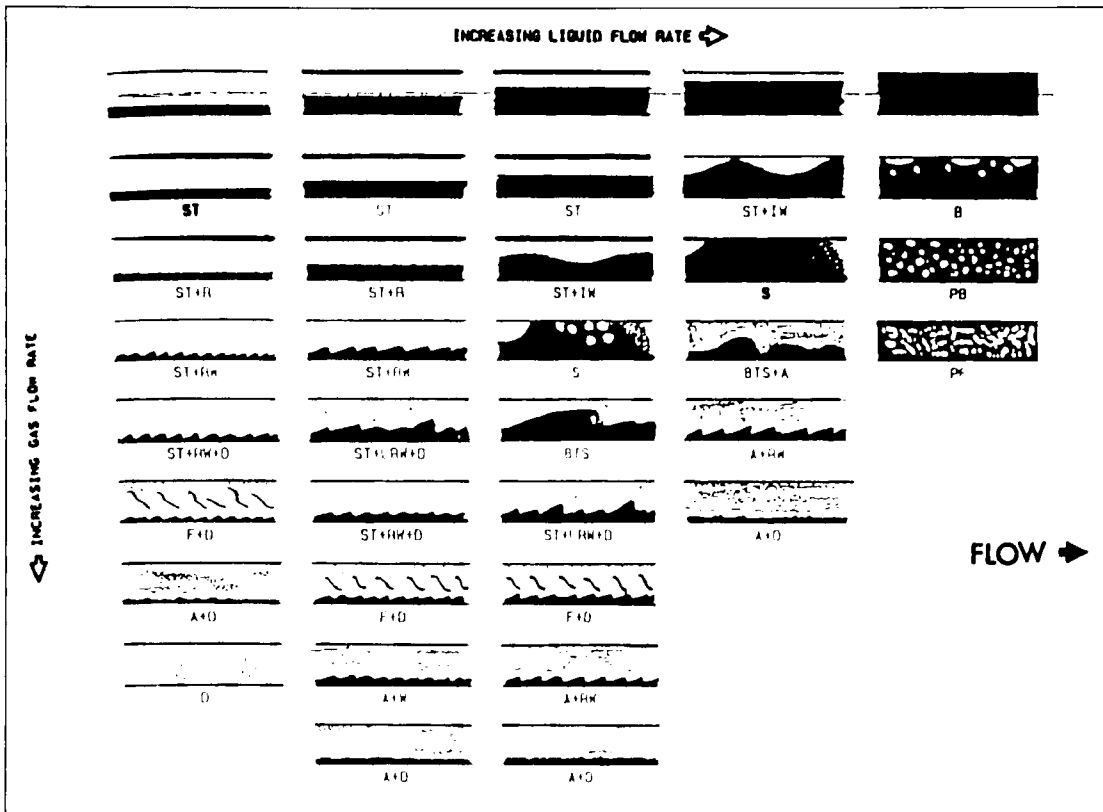
Figure 2.2: Spedding and Hand (1993) Defined Flow Regimes

2.1.1 Flow Regimes Used In Present Research

Many researchers have further divided the six main flow regimes into sub-regimes. For example, Hand and Spedding (1993) identified 31 sub-regimes for horizontal gas-liquid flow (Figure 2.2). Unfortunately this practice can lead to multiple names from different researchers for the same observed flow regime. In order to simplify the number of flow regimes presented in this work, the following common descriptions will be used for the eight major flow regimes:

Stratified (ST): Air and oil flow at very low velocities along the tube, with the air occupying the top half of the tube (Picture a – all pictures refer to Figure 2.3).
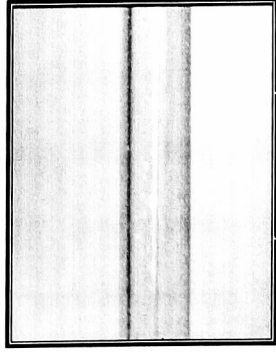
a: Stratified Flow

b: Wavy Flow
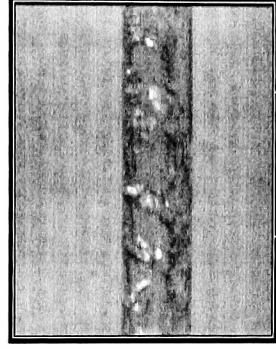
c: Annular Flow
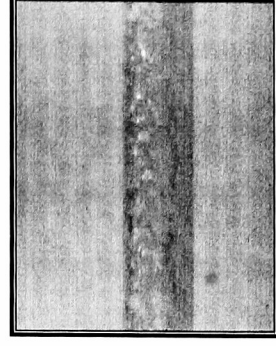
d: Mist Flow

e: Plug Flow
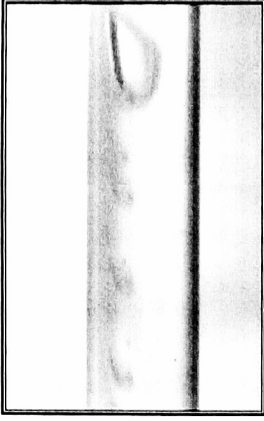
f: Dispersed Flow
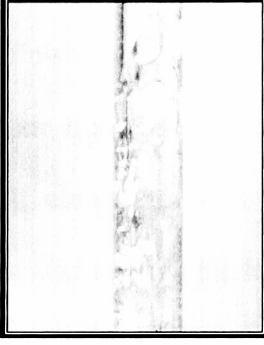
g: Froth Flow
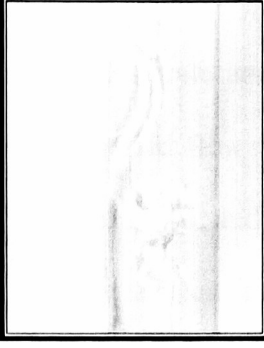
h: Slug Flow
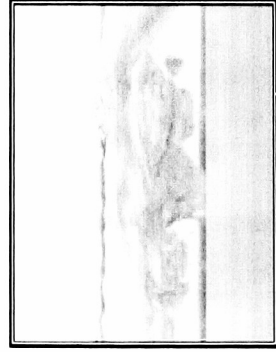
i: Slug Building Zone
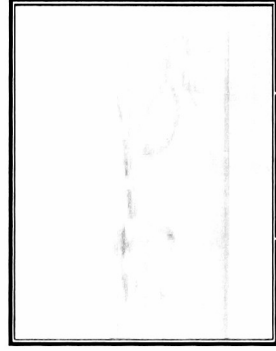
j: Foam Slug
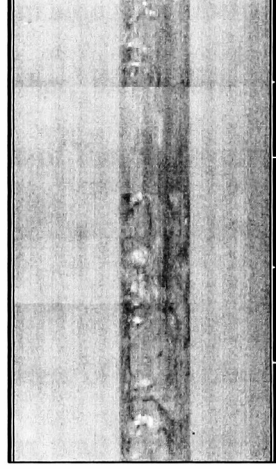
k: Blow Through Slug

Figure 2.3: Flow Regimes Defined For Thesis

Wavy (W): Maintaining the oil flow rate and increasing the air flow rate causes the interface of the two phases in stratified flow to become wavy (Picture b). The higher velocity air both pushes the oil ahead of it, and entrains oil behind it, forming waves. At high enough air flow rates, the oil in the center of the tube is depressed, forcing oil to rise along the sides of the tube and resulting in a thin oil film along the tube walls.

Annular (A): As the air flow rate is increased further, the transition from wavy to annular flow occurs. The air flows along the center of the tube with most of the oil forced into a film flowing along the tube walls (Picture c). The oil film has a characteristic crescent shape, and is often thicker at the bottom of the tube. Occasionally waves are visible at the interface between this bottom layer of oil and the air.

Mist (M): Often referred to as "droplet" flow (Chang and Tremblay, 1976; Hand and Spedding, 1993), the air velocity is now sufficiently high enough to shear the oil off the walls, forming small drops entrained in the air flow. A very thin oil film continues to be present along the tube, but the film has no discernible structure (unlike annular flow). If the oil flow rate is also increased, the transparent tube becomes opaque due to the high velocity of the oil film along the tube walls (Picture d).

Plug (P): A stratified flow will transition to plug flow if the oil flow rate is increased while the air flow rate is maintained. The oil level rises in the tube as the oil flow rate increases, until it fills it completely. This forces the air into flowing as bubbles (called plugs) of varying sizes along the top of the tube at relatively slow speeds. The plugs, regardless of size, have a characteristic shape, rounded at the front edge and tapered at the trailing edge (Picture e).

Dispersed (D): Further increasing the oil flow rate forces the plugs to break apart and form very small bubbles that flow along the center of the tube (Picture f). This regime is often called dispersed bubble or simply bubble flow in the literature. At very low air flow rates, this regime can be characterized by a pulsing of the bubbles, when the bubbles cease flowing for brief periods of time and then resume. This is due to the higher liquid phase pressure, which retards air flow until the air has built-up significant pressure to overcome the back-pressure.

Froth (F): At air flow rates equal to those of annular flow, the dispersed flow regime transitions to the froth flow regime. The bubbles are now very small and evenly dispersed, resulting in a "froth" appearance for the flow regime. While the froth and mist flow regimes can be similar in appearance, there are two ways to tell them apart: the pulsing appearance of the froth regime, and the significantly higher air flow rates of the mist regime (Picture g).

Slug (S): If during the wavy flow regime the air flow rate is kept constant and the oil flow rate is increased, larger waves move along the tube. When these waves grow large enough to touch the top of the tube, they are called slugs. At high enough oil velocities, small slugs of oil occupying the entire diameter of the tube are both preceded and followed by pockets of air. The slugs can be of varying length, and can be of any form from pure liquid to highly aerated. Once the slug front has passed, the oil level in the tube slowly rises until the next slug passes (Picture h).

In addition to the eight major flow regimes, three minor or sub-category slug flow regimes will be used. This is necessary due to the wide-range of structures observed in the slug flow regime.

Slug Building Zone (SBZ): Very short slugs of oil occur after three or four large waves that don't completely fill the tube (Picture i). Between waves the phase interface is smooth.

Foam Slug (FS): At very high oil flow rates, the slugs are highly aerated and have a very similar appearance to a breaking wave. Immediately following the slug, the flow has no discernible structure and large bubbles may occupy almost the full diameter of the tube (Picture j).

Blow Through Slug (BTS): Slugs moving at the same high velocity as the air travel down the length of the tube, disrupting the otherwise annular appearance of the flow (Picture k). This is actually the transition region between slug and annular flow, but has such a constant structure regardless of air and oil flow rates that it is often identified as a specific regime.

Any additional observed flow regimes will be classified as transitional regimes, featuring characteristics of more than one of the eleven defined flow regimes. It should be noted that one of the most commonly observed types of flow regimes in two-phase and three-phase horizontal flows where oil is one of the phases is that of slug flow (Herm-Stapelbert and Mewes, 1994). The importance of slug flow is illustrated in the current research by the need for four unique definitions to differentiate between the types of slug

flow observed. The specific impact slug flow has on developing predictive pressure drop models is discussed in Chapter Three.

2.1.2 Flow Regime Identification Methods

There are three main approaches to identifying flow regimes:

1) Visual observation of the flow by the naked eye, with photography or using a high-speed video camera.

2) Measurement of the pressure fluctuations using pressure transducers or the instantaneous and averaged local void fraction using techniques like capacitance sensors and probes, hot-wire probes, and x-ray or γ-ray attenuation.

3) Tomography methods that reconstruct the distribution of the phases inside the tube using capacitance sensors, ultrasonic techniques, and x-ray or γ-ray attenuation.

All three approaches have specific advantages and disadvantages to them. Visual observation is a simple technique but subjective and difficult to make, especially at high phase velocities. A high-speed imaging system can alleviate some of the difficulties associated with visual observation. With the proper image processing, large amounts of detail about the flow regime structure can be determined from the captured images (Levy, 1999). Measurement of local pressure fluctuations as a function of time has shown great success in distinguishing the points of transition between flow regimes (Hand and Spedding, 1993). Hubbard and Dukler (1966) first introduced the technique by applying

$$R_{PP}(\tau) = {}_T\varlimsup_{\infty} \frac{1}{T} \int_0^T p(t)p(t+\tau)dt$$

$$G_{PP}(f) = 2\int_{-\infty}^{\infty} R_{PP}(\tau)\exp(-i2\pi f\tau)d\tau = 4\int_0^{\infty} R_{PP}(\tau)\cos(2\pi f\tau)d\tau$$
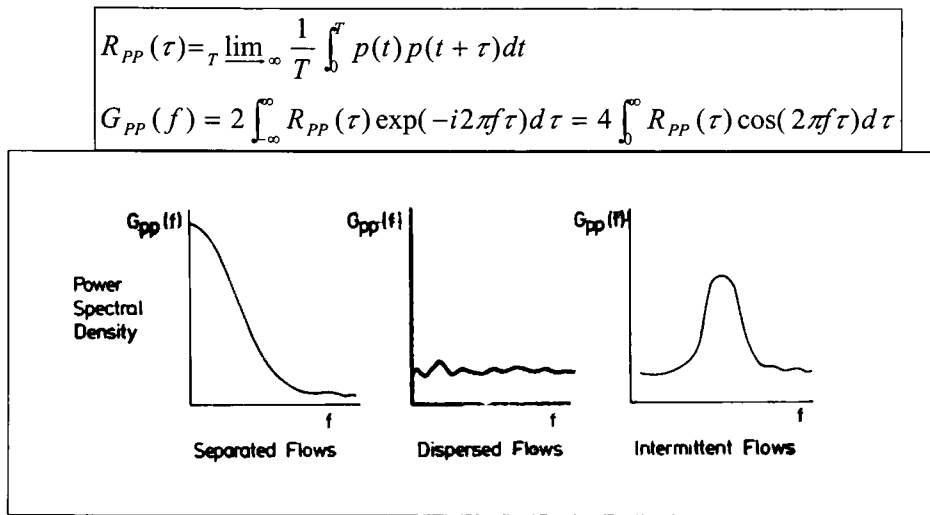
Figure 2.4: Hubbard and Dukler (1966) Frequency Distributions

a correlation to the local pressure p(t) and converting the readings into a power spectral density. Figure 2.4 shows the three distinct frequency distributions Hubbard and Dukler (1966) found for separated (ST, W), dispersed (D, A) and intermittent (P, S, BTS) flows. More recent research has found that most power spectral density plots are not as clear as those found by Hubbard and Dukler (Hetsroni, 1982). Pressure waves can reflect at the test section outlet, interfering with the reading (Hubbard and Dukler, 1966). The flow regimes hardest to interpret are often also the flow regimes that are difficult to observe visually (Hetsroni, 1982).

Similarly, the void fraction or liquid hold-up fluctuations can be measured using techniques like capacitance sensors, x-ray or gamma ray absorption. Chapter Five will discuss the use of capacitance sensors in detail. In x-ray or γ-ray absorption techniques, a beam of radiation is passed through the flow and the attenuation measured by a detector. As liquid content decreases, fewer x-rays (or γ-rays) are absorbed by the flow, and the voltage signal from the detector increases, indicating a higher instantaneous void fraction

(Hetsroni, 1982). One method of analyzing the voltage signal from the detector is to determine the probability density function (PDF) for void fraction. Jones and Zuber (1975) found three distinct distributions for the PDF:

1) A single peak at low void fraction indicates dispersed flow

2) A single peak at high void fraction indicates annular flow

3) Double peaks indicate intermittent (S, P, BTS) flow

While the radiation absorption technique is well defined in the literature, the use of radiation can make this technique unacceptable for experimental use (Hetsroni, 1982).

The third approach involves the measurement of phase distribution spatially as well as temporally. This technique, called tomography, produces an image of the spatial phase distribution in the channel over time. Several tomography methods have been well developed, including capacitance and x-ray techniques. Capacitance methods measure the varying capacitance between plates arranged around the channel. An example of the arrangement used by Xie et. al. (1989) is shown in Figure 2.5. By comparing the known capacitance of the two phases to the measured values between plates, a computer program is used to reconstruct the phase distribution (Chang et. al., 1995). Harvel et. al. (1999) used a similar approach to measure the variation in a x-ray multibeam system. Multiple detectors measure and compare the x-ray beams intensity, and a computer program reconstructs the spatial phase distribution over time.
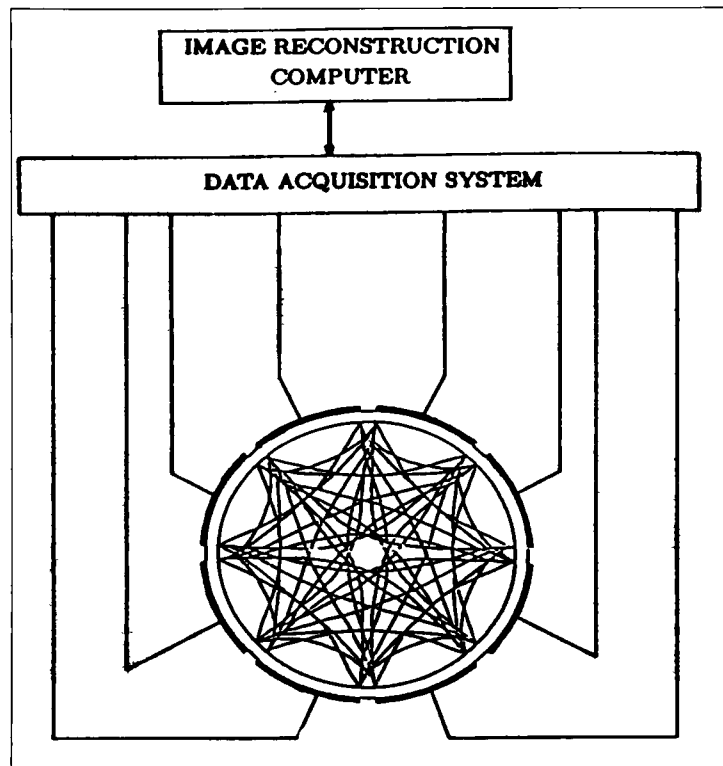
Figure 2.5: Capacitance Sensor Arrangement (Xie et. al., 1989)

In general, void fraction and liquid hold-up measurement techniques have been shown to indicate the transition boundaries with a high degree of accuracy (Hand and Spedding, 1993). Visual observations combined with one or more other techniques can be used to accurately identify the flow regimes. In the current research only visual observation of the flow using a high-speed video camera is made to distinguish between flow regimes. A second technique of flow regime identification using void fraction measurement with a capacitance sensor has been developed as part of this thesis and preliminary results are discussed in detail in Chapter Five.

2.2 Flow Regime Maps

Flow regime maps have been developed to predict the transition between regimes under various flow conditions. The two basic approaches are either empirical or semi-theoretical in nature. Empirical flow regime maps use experimental data and observations plotted with some defined parameter to distinguish the transition from one flow regime to another. By postulating the mechanisms that control/influence transition between flow regimes, and producing sets of equations for each transition, semi-theoretical flow regime maps can be developed. The four main plotting parameters for the maps are mass flux, momentum flux, superficial velocities, and some form of dimensionless parameters (Froude number, ratio of volumetric flow rates, etc). The most commonly used empirical maps are those of Baker (1954) and Mandhane et al. (1974), while the most commonly used semi-theoretical map is the one developed by Taitel and Dukler (1976).

A great deal of work has been done in developing and comparing different flow regime maps (Barnea et. al., 1979; Spedding and Nguyen, 1980; Rouhani and Sohal, 1983; Hand and Spedding, 1993). Unfortunately, no map has been found to perform well under all test conditions and for all possible gas-liquid combinations. Spedding and Nguyen (1980) suggest that there are four possible causes:

1) Phase properties for different types of gas and liquids influence the transition boundaries.

2) Test facilities vary in set-up and capabilities. For example, the phase mixing process can affect which flow regimes a facility can produce.

3) Parameter definitions vary between different researchers.

4) Error in the drawing of transition boundaries on the original map (work incorrectly presented in original paper causes reproduction problems).

Many maps, both semi-theoretical and empirical, use air-water properties in order to plot the transition boundaries. Spedding and Nguyen (1980) found that these maps perform poorly when applied to flows using air and higher viscosity liquids, particularly in the prediction of transition to slug flow. Recent studies by Nadler and Mewes (1995) and Andritsos et al. (1989) have found that for higher viscosity fluids, transition to slug flow occurs at lower liquid velocity values than predicted by most maps. One possible explanation for this phenomenon is the fact that most plotting parameters do not take viscosity into account.

Two other important parameters in predicting transition boundaries not often accounted for in most flow regime maps are pipe diameter and length. While superficial velocity indirectly takes diameter into account, Mandhane et. al. (1974) found that as diameter increased, the accuracy of their map decreased. They suggest that some additional diameter factor must be included in the transition boundary equations. Weisman et al. (1979) found that pipe diameter must be included in predicting transition boundaries, and adapted the theoretical map of Taitel and Dukler (1976) to include pipe diameter. This adaptation was then compared with experimental data and found to give more accurate results (Weisman et. al., 1979). A more recent study on 2.54 and 9.53 cm I.D. tubes (considered small diameter) found that diameter only plays a role in low gas velocity transitions (Lin and Hanratty, 1987). Taitel and Dukler (1987) revisited their

own semi-theoretical flow map equations and found that pipe length is an important

factor in determining transition from stratified to intermittent (plug and slug) or annular

flows for high viscosity liquids. Fully developed intermittent flow in these high viscosity

liquids was found to take much longer to occur than in air-water flows, upon which most

maps are based (Taitel and Dukler, 1987).

Due to the problems associated with existing flow regime maps, the first objective

of the current research is to compare the actual flow regime transition boundaries for the

present system with those predicted by two of the most widely used and recommended

flow regime maps. The empirical map of Mandhane et al. (1974) and the semi-

theoretical map of Taitel and Dukler (1976) have both been evaluated by numerous

authors and are selected for this reason. For ease of comparison, both maps are presented

using superficial phase velocities as the plotting parameters. A third flow regime map

developed by Spedding and Nguyen (1980) is also evaluated because of its use of

dimensionless plotting parameters, which has been cited as being more effective in

predicting transitional boundaries (Lin and Hanratty, 1987; Spedding and Spence, 1993).

2.2.1 Mandhane et al. (1974) Flow Regime Map

The Mandhane et al. (1974) flow regime map is based on the flow regime map

developed by Baker (1954). The Baker map is based on a wide range of data for various

air-liquid and pipe diameter combinations (Whalley, 1990). Each data point is plotted

using the individual mass flux (kg/m^{2}s) of the phase multiplied by a dimensionless

property correlation variable. Baker (1954) introduced the dimensionless variables in an

effort to adjust the transition boundaries for fluids other than water. The plotting

parameters are defined as follows:

$$m_i = \rho V A \qquad \text{Phase mass flow rate (kg/s)} \qquad 2.1$$

$$A = \frac{\pi d^2}{4} \qquad \text{Tube cross-sectional Area (m}^2\text{)} \qquad 2.2$$

$$G_i = \frac{m_i}{A} \qquad \text{Mass Flux (kg/m}^2\text{s)} \qquad 2.3$$

$$\lambda = \left(\frac{\rho_g \rho_l}{\rho_{air} \rho_{H2O}} \right)^{0.5} \qquad 2.4$$

$$\psi = \frac{\sigma_{H2O}}{\sigma_l} \left[\left(\frac{\mu_l}{\mu_{H2O}} \right) \left(\frac{\rho_{H2O}}{\rho_l} \right)^2 \right]^{1/3} \qquad 2.5$$

$$\frac{G_g}{\lambda} \qquad \text{y plotting parameter}$$

$$G_l \psi \qquad \text{x plotting parameter}$$

The Mandhane et al. (1974) flow regime map was developed, with use of a large data

bank, to simplify the plotting parameter structure by making use of superficial velocities.

The superficial velocity is defined as the mass flux of a phase divided by the density of

the phase.

$$j_i = \frac{G_i}{\rho_i} \ \text{(m/s)} \qquad 2.6$$

This is the velocity of the gas or liquid obtained by considering it as the only phase

flowing in the channel. Figure 2.6 shows the resulting flow map. In order to take into

account the effect of physical properties on the transition boundaries, Mandhane et. al.

(1974) proposed two correction factors based on early work by Glover and Aziz (1974)

and with the addition of viscosity terms.

$$X' = (\frac{\rho_g}{0.0808})^{0.2} (\frac{72.4\rho_l}{62.4\sigma})^{0.25} (\frac{\mu_g}{0.018})^{0.2} \qquad 2.7$$

$$Y' = (\frac{\mu_l}{1.0})^{0.2} (\frac{72.4\rho_l}{62.4\sigma})^{0.25} \qquad 2.8$$

It should be noted that the constants in the equations are based on imperial units, and all physical properties should be in these units. The transition boundaries are expressed as a series of co-ordinates listed in Table 2.1. To account for changes in physical properties, the superficial velocity co-ordinate is multiplied by the suggested physical property correction as listed in Table 2.1.

$$j_i' = Mj_i \qquad 2.9$$

Table 2.1 Co-ordinates for Mandhane et. al. (1974) Map Transition Boundaries

Transition Boundary	j_g (ft/s)	j_l (ft/s)	Physical Property Correction M
Stratified to Plug	0.1	0.5	Y'^{-1}
	5.0	0.5	Y'^{-1}
Wave to Slug	7.5	0.3	Y'
	40.0	0.3	Y'
Plug and Slug to Dispersed	0.1	14.0	Y'
	230.0	14.0	Y'
Stratified and Plug to Wave and Slug	35.0	0.01	X'
	14.0	0.1	X'
	10.5	0.2	X'
	2.5	1.15	X'
	2.5	4.8	X'
	3.25	14.0	X'
Wave and Slug to Annular-Mist	70.0	0.01	X'
	60.0	0.1	X'
	38.0	0.3	X'
	40.0	0.56	X'
	50.0	1.0	X'
	100.0	2.5	X'
	230.0	14.0	X'
Dispersed to Annular-Mist	230.0	14.0	X'
	269.0	30.0	X'
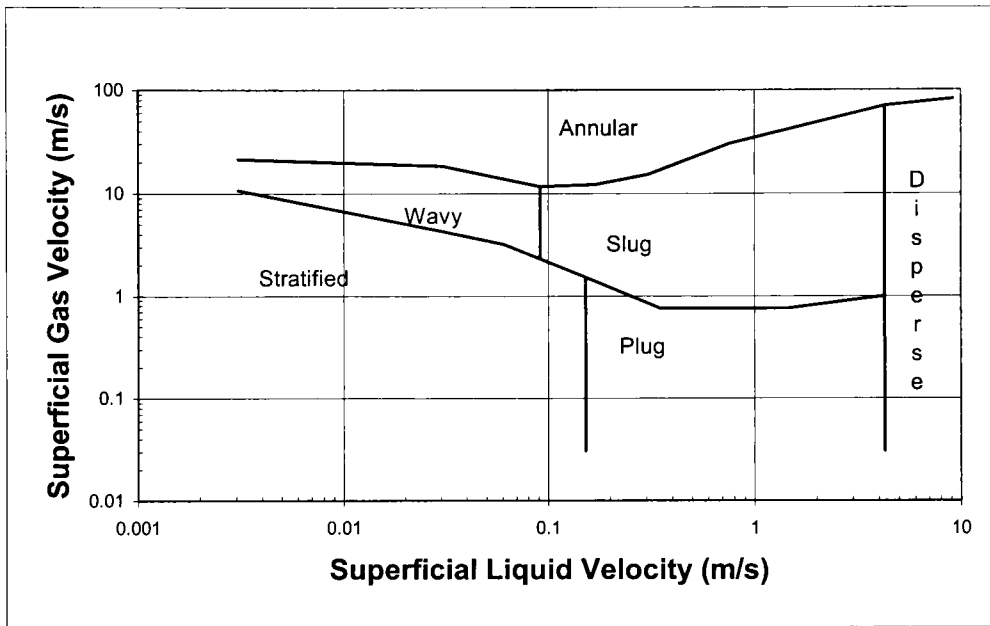
Figure 2.6: Mandhane et. al. (1974) Flow Regime Map
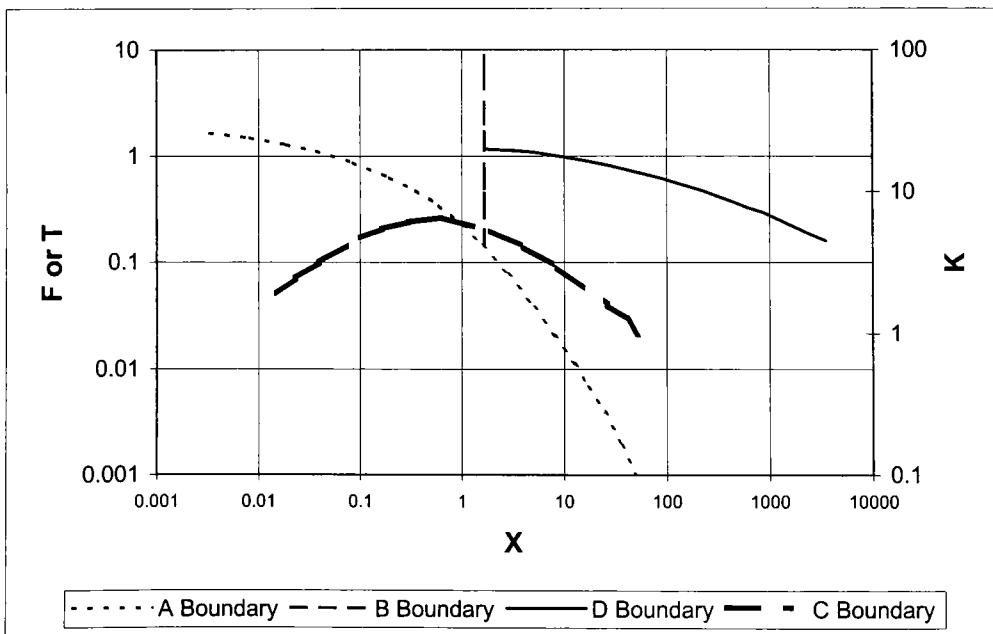
Figure 2.7: Taitel and Dukler (1976) Flow Regime Map

2.2.2 Taitel and Dukler (1976) Flow Regime Map

The Taitel and Dukler (1976) flow regime map (Figure 2.7) is the most widely recommended semi-theoretical flow regime map because each transitional boundary is defined by two parameters representing the transition mechanism. It is, however, more complicated than the Mandhane et al. (1974) map, requiring the calculation of four dimensionless numbers. The horizontal axis uses the Martinelli number (X), which is based on the frictional pressure drops for the liquid and gas. The pressure drops are determined by calculating the single-phase Reynolds number (Re) and friction factor (f) for a round tube.

$$\text{Re}_i = \frac{G_i d}{\mu_i} \qquad\qquad 2.10$$

$$f_i = \frac{16}{\text{Re}_i} \qquad \text{if } \text{Re}_i \leq 2000 \qquad\qquad 2.11$$

$$f_i = \frac{0.079}{\text{Re}_i^{0.25}} \qquad \text{if } \text{Re}_i \geq 2000 \qquad\qquad 2.12$$

$$\left(\frac{dP}{dz}\right)_i = -\frac{2 f_i G_i^2}{d \rho_i} \qquad\qquad 2.13$$

The above friction factor and pressure drop equations are those defined by Whalley (1990). Once the individual phase pressure drops are determined, the Martinelli number can then be found as:

$$X = \left[\frac{\left(\dfrac{dP}{dz}\right)_l}{\left(\dfrac{dP}{dz}\right)_g} \right]^{0.5} \qquad\qquad 2.14$$

The vertical axis is one of three numbers, depending on the flow regime transition. The numbers are based on the phase properties and mass flux, and are defined as:

$$Fr = \frac{G_g}{\left[\rho_g(\rho_l - \rho_g)dg\right]^{0.5}}$$ 2.16

$$T = \left[\frac{\left|\left(\frac{dP}{dz}\right)_l\right|}{d(\rho_l - \rho_g)}\right]^{0.5}$$ 2.17

$$K = Fr\left[\frac{G_l d}{\mu_l}\right]^{0.5}$$ 2.18

Each equation was developed by examining the individual mechanisms that cause transition from one flow regime to another (Taitel and Dukler, 1976). Table 2.2 lists the parameters used for each transition boundary.

Table 2.2 Taitel and Dukler Transition Boundary Parameters

Boundary	Required Equations	Transition Boundary
A	X, F	Wavy to Annular
B	X, F	Intermittent to Annular
C	X, K	Stratified to Wavy
D	X, T	Intermittent to Dispersed

Due to the complexity of determining the dimensionless variables, Taitel and Dukler (1976) recalculated the transitional boundaries in terms of superficial velocities (Figure 2.8) for air-water flow in a 2.5 cm pipe at atmospheric conditions. Several more recent studies have been conducted to investigate the effects of pipe diameter and length on the Taitel and Dukler map. Only the study of Taitel and Dukler (1987) suggested possible changes to the existing plotting parameter equations. However these changes
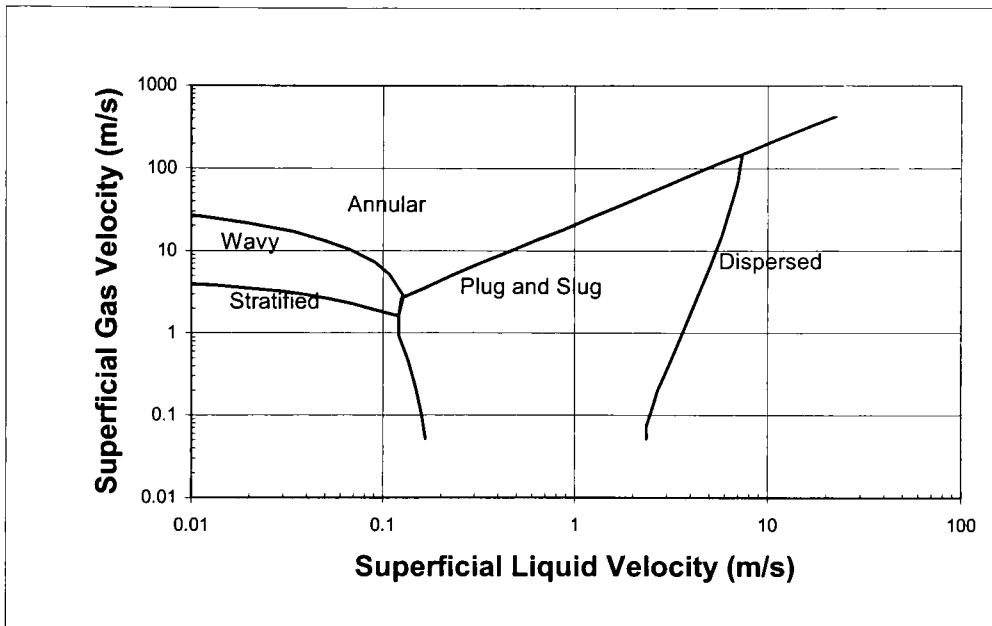
Figure 2.8: Taitel and Dukler (1976) Flow Regime Map Replotted
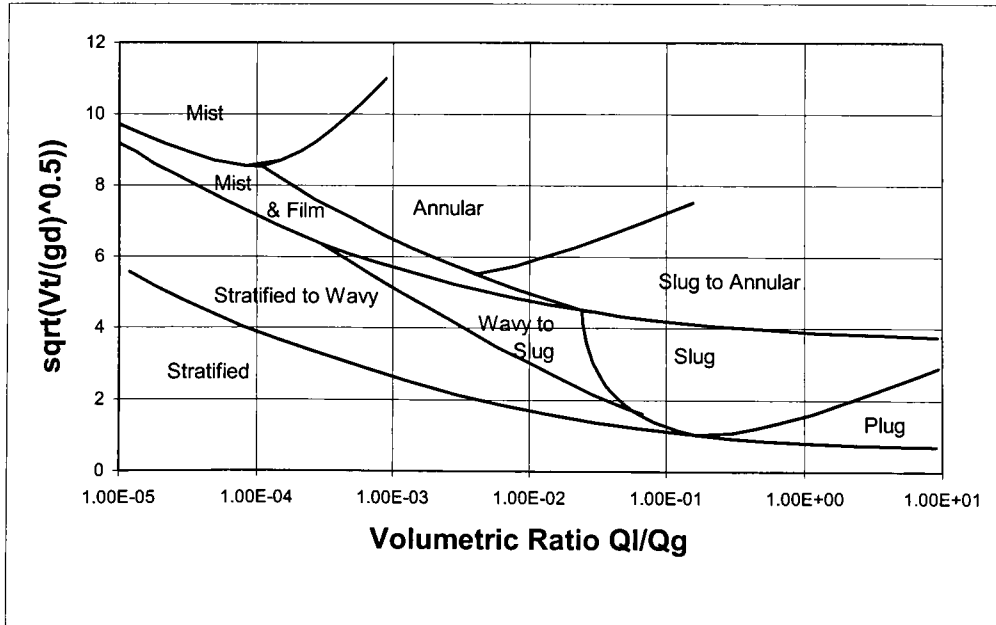
Figure 2.9: Spedding and Nguyen (1980) Flow Regime Map

were recommended for use only with liquids viscosities above 50 cP and therefore do not apply to the oil (28 cP) being used in this study.

2.2.3 Spedding and Nguyen (1980) Flow Regime Map

Developed as a result of a study comparing existing flow regime maps in 1980, the Spedding and Nguyen map uses dimensionless plotting parameters. By simplifying the flow patterns to four basic types, Spedding and Nguyen identified five important variables for transition: Q_L, Q_G, β_{dry}, Q_L/Q_G, and the Froude Number (Spedding and Spence, 1993). The value β_{dry} represents the volumetric dryness fraction and Q_i the volume flow rate of the phase. The Froude number is defined as:

$$Fr = \frac{V_T}{\sqrt{gd}} \qquad\qquad 2.19$$

Unlike the logarithmic scales for the superficial velocity maps, the Froude number is plotted in a square root form and the volumetric flow rate ratio in logarithmic form (Figure 2.9). The defined flow regimes are different than the previously presented maps, with both BTS and W-S flow transitions represented as flow regions instead. Later studies have found that the map predicts the transition boundaries well for all intermittent and stratified patterns, but fails to take diameter effects into account for high gas flow rate transitions (Lin and Hanratty, 1987; Spedding and Spence, 1993). Dispersed flow is also excluded from the map, decreasing the application of the map to various flow conditions.

Chapter Three: Predictive Pressure Drop Models

The second objective of the research presented here is to develop an accurate method of predicting pressure drop for air/oil flow in horizontal pipes. There are three components of the basic pressure drop equation: frictional, gravitational, and momentum.

$$\left(\frac{dP}{dz}\right)_{TP} = \left(\frac{dP}{dz}\right)_F + \left(\frac{dP}{dz}\right)_G + \left(\frac{dP}{dz}\right)_M \qquad 3.1$$

The gravitational term does not apply to horizontal flow and can be neglected. Additionally for adiabatic flow, many researchers have found that the momentum term (due to expansion/contraction of the gas phase) is relatively small in comparison to the frictional term (Herm-Stapelbert and Mewes, 1994; Nicholson et. al., 1978; Souza et. al., 1993; Whalley, 1990). Further the acceleration term is only significant in heated two-phase flows. While the momentum component should be taken into account to achieve the most accurate prediction of pressure drop, it is often neglected without greatly reducing the accuracy of the prediction model (Herm-Stapelbert and Mewes, 1994; Nicholson et. al., 1978; Hetsroni, 1982). Therefore, it is often only the frictional pressure drop being predicted by the most common models in use today.

As with the flow regime maps, predictive pressure drop models are traditionally categorized as either empirical or semi-theoretical. Yet over the years the most common theoretical equations have had some form of an empirical correction factor applied to them, making them semi-theoretical. Thus the distinction between theoretical and empirical models has become blurred, and is usually based on the number of flow

26

regimes to which the models can be accurately applied. Generally empirical models are considered those that are developed to predict the pressure drop in specific flow regimes, most commonly intermittent (e.g. slug) flows. These models are often based on basic theoretical models that have been considerably altered by experimentally determined correction factors. For the current research, the model of Chang and Tremblay (1976) for mist flow can be considered an empirical model.

A more simplistic approach to differentiating between models is based on how each model addresses the two-phase mixture. There are two types of models; those that assume common mixture properties and those that assume separated phase properties. The general homogeneous model and the Chang and Tremblay model both assume common mixture properties. All other models presented in this chapter assume separated properties. Unless otherwise noted, all theory presented in sections 3.1 and 3.3 is referenced to the individual papers that first presented the model being discussed and the general references of Levy (1999), Whalley (1990), and Hetsroni (1982).

3.1 The Homogeneous Model

The homogeneous model assumes that the two-phase mixture can be characterized with one set of common properties because the velocities of the phases are assumed to be equal. The homogenous properties are determined from the mass flow rates, densities and viscosities of the liquid and gas. Quality of mixture, void fraction, density and viscosity are calculated as follows:

$$x = \frac{m_g}{(m_l + m_g)} \qquad\qquad 3.2$$

$$\alpha_H = \frac{x\rho_l}{(x\rho_l + (1-x)\rho_g)} \qquad\qquad 3.3$$

$$\rho_H = \alpha_H \rho_g + (1 - \alpha_H)\rho_l \qquad\qquad 3.4$$

$$\mu_H = \frac{(\frac{\mu_g}{\mu_l})}{\left[(x\mu_l) + \frac{(1-x)}{\mu_g} \right]} \qquad\qquad 3.5$$

The void fraction is the time-averaged fraction of the volume of the tube occupied by the gas phase. Once the homogenous properties are determined, the total frictional pressure drop can be found by calculating the Reynolds number and friction factor.

$$G_T = \frac{4(m_g + m_l)}{\pi d^2} \qquad\qquad 3.7$$

$$\mathrm{Re}_H = \frac{G_T^2 d}{\mu_H} \qquad\qquad 3.9$$

$$f_H = \frac{16}{\mathrm{Re}_H} \ \text{if } \mathrm{Re}_H < 2000 \qquad\qquad 3.8$$

$$f_H = \frac{0.079}{\mathrm{Re}_H^{0.25}} \ \text{if } \mathrm{Re}_H > 2000 \qquad\qquad 3.9$$

$$\left(\frac{dP}{dz} \right)_F = -\frac{2 f_H G_T^2}{d \rho_H} \qquad\qquad 3.10$$

There is general agreement that the homogenous model can only satisfactorily predict the pressure drop of flow regimes of very low or very high void fraction (almost total liquid or total gas) (Cotton et. al., 1996; Ferguson and Spedding, 1995). This is due to the fact

that the common mixture properties are largely influenced by the phase occupying the greater proportion of the channel. However, it is a good point from which to start the analysis of the various pressure drop models, as it is relatively simple to use.

3.1.1   Two-Phase Multipliers

Often in comparing results of the model to the actual pressure drop a variable called a two-phase multiplier is used. The two-phase multiplier (Φ_{lo}^2) is the factor by which the single-phase pressure gradient must be multiplied to determine the two-phase pressure gradient. In this case, the sub-script (lo) refers to liquid single-phase flow calculated using the total (gas + liquid) mass flux of the two-phase flow. Similar multipliers for liquid (l) (liquid mass flux only), gas (g) (gas mass flux only) and gas (go) (total mass flux) can be found.

While the basic calculation of the two-phase multiplier requires the total pressure gradient and the liquid-only pressure gradient, for the homogenous model it can be shown that:

$$\Phi_{lo}^2 = \frac{\rho_l}{\rho_H} \qquad\qquad 3.11$$

To find Φ_{lo}^2 for the measured pressure drop, the pressure gradient for the liquid is determined. The friction factors for the total flow and the liquid only flow are assumed equal.

$$f_H = f_{lo}$$
$$\left(\frac{dP}{dz}\right)_{lo} = -\frac{2f_H G_T^2}{d\rho_l} \qquad\qquad 3.12$$

$$\Phi_{lo}^{2} = \frac{\left(\dfrac{dP}{dz}\right)_{Factual}}{\left(\dfrac{dP}{dz}\right)_{lo}} \qquad\qquad 3.13$$

Two-phase multipliers will not be used for comparison of pressure drop models in this work but are introduced here because of the frequent use of them in defining separated flow model equations.

3.2 The Chang and Tremblay (1976) Model

Developed specifically to predict the pressure drop of air-oil mist flow along a straight pipe, this model is based on the homogeneous model. The major change to the homogeneous model is the introduction of an experimentally defined coefficient of resistance C_R with the pressure drop equation given as:

$$\left(\frac{dP}{dz}\right)_{Pred} = C_R \frac{\rho_g u_g^{2}}{2d} \qquad\qquad 3.14$$

The coefficient of resistance C_R is based on the superficial Reynolds numbers for the two phases.

$$\text{Re}'_i = \frac{4 m_i}{\pi d \mu_i} \qquad\qquad 3.15$$

$$\log C_R = a_1 \log \text{Re}'_l + a_0 \qquad\qquad 3.16$$

Starting from equation 3.16, and determining constants a_1 and a_0 from experimental data, the value for C_R was found. In this case, a_1 and a_0 are functions of Re'_g the superficial gas velocity.

$$C_R = 0.02397\,\mathrm{Re'}_g^{\,0.1252}\,\mathrm{Re'}_l^{\,X} \qquad\qquad 3.17$$

$$X = 21.1836\,\mathrm{Re'}_g^{\,-0.3384} + 0.1622 \qquad\qquad 3.18$$

It is important to remember that this model is only applicable to the air-oil mist flow regime, and applying it to a different regime or using an alternative liquid would result in large prediction errors (Chang and Tremblay, 1976).

3.3 The Common Separated Flow Models

There are numerous models that consider the two phases separately. The inherent assumption in all separated flow models is that the two phases reach constant but not necessarily equal velocities. The accuracy of this approach is highly dependent on the flow regime, as clearly defined phase velocity separation is being assumed. While many models of this type have been developed, the three most commonly recommended are those of Friedel (1979), Martinelli (1948) and Chisholm (1973). Each of these separated flow models have been found to be acceptably accurate only when certain flow criteria are met. After applying these three models to the Heat Transfer and Fluid Flow Service proprietary data bank, Whalley suggested the following guidelines for usage (Hetsroni, 1982):

- For $\mu_L/\mu_G < 1000$, the Friedel (1979) correlation should be used.

- For $\mu_L/\mu_G > 1000$ and $G > 100$ kg/m^{2}s, the Chisholm (1973) correlation should be used.

- For $\mu_L/\mu_G > 1000$ and $G < 100$ kg/m^{2}s, the Martinelli (1948) correlation should be used.

For the air-oil flows studied for this thesis, the viscosity ratio is greater than 1000 and thus the Friedel model will not be evaluated. However, the Friedel model is still presented for reference, as later air-oil studies at higher temperatures will lower the viscosity ratio.

3.3.1 The Friedel (1979) Model

The Friedel model is an empirical model based on a 25000-point data bank (Friedel, 1979). The model makes use of phase properties, mass flux, and quality to determine the two-phase multiplier:

$$\Phi_{lo}^2 = E + \frac{3.24FH}{Fr^{0.045}We^{0.035}} \qquad 3.19$$

where:

$$E = (1-x)^2 + x^2 \left(\frac{\rho_l f_{go}}{\rho_g f_{lo}} \right) \qquad 3.20$$

$$F = x^{0.78}(1-x)^{0.224} \qquad 3.21$$

$$H = \left(\frac{\rho_l}{\rho_g} \right)^{0.91} \left(\frac{\mu_g}{\mu_l} \right)^{0.19} \left(1 - \frac{\mu_g}{\mu_l} \right)^{0.7} \qquad 3.22$$

$$Fr = \frac{G_T^2}{gd\rho_H^2} \qquad 3.23$$

$$We = \frac{G_T^2 d}{\rho_H \sigma} \qquad 3.24$$

The friction factors f_{go} and f_{lo} are determined by the same method as for the homogeneous flow model; however, the Reynolds number is based on the total mass flux and the viscosity of the individual phase.

$$\text{Re}_i = \frac{G_T d}{\mu_i} \qquad\qquad 3.25$$

The pressure drop for liquid only can then be determined, and the total pressure drop predicted.

$$\left(\frac{dP}{dz}\right)_{lo} = \frac{2f_{lo}G_T^2}{d\rho_l} \qquad\qquad 3.26$$

$$\left(\frac{dP}{dz}\right)_{\text{Pred}} = \Phi_{lo}^2\left(\frac{dP}{dz}\right)_{lo} \qquad\qquad 3.27$$

3.3.2 The Martinelli (1948) Model

This model uses the properties of the two phases and the quality of the mixture to determine a parameter called the Martinelli number. This is the same parameter used in the Taitel & Dukler flow regime map. The general form of the equation is give by 3.28 while equation 3.29 gives an alternative form suggested by Chisholm (1967).

$$X^2 = \left[\frac{\left(\dfrac{dP}{dz}\right)_l}{\left(\dfrac{dP}{dz}\right)_g}\right] \qquad\qquad 3.28$$

$$X = \left(\frac{\mu_g}{\mu_l}\right)^{n/2}\left(\frac{1-x}{x}\right)^{(2-n)/2}\left(\frac{\rho_g}{\rho_l}\right)^{0.5} \qquad\qquad 3.29$$

The value for n is 0.25 based on the smooth pipe value for friction factors. In order to determine the pressure drop, the slip ratio and a variable C must be found. The slip ratio is the ratio of phase velocities, which is unity for homogeneous flow, and usually greater than one for separated flow (gas velocity > liquid velocity). Chisholm (1972) developed a simple correlation for determining slip ratio when the phase velocities are not known.

$$s = \left[1 - x \left(1 - \frac{\rho_l}{\rho_g} \right) \right]^{0.5} \qquad\qquad 3.30$$

Chisholm (1967) also developed relations for Φ_l^2 and Φ_g^2 by curve fits for the Lockhart and Martinelli (1949) correlation.

$$\Phi_l^2 = 1 + \frac{C}{X} + \frac{1}{X^2} \qquad\qquad 3.31$$

$$\Phi_g^2 = 1 + CX + X^2 \qquad\qquad 3.32$$

Combining the two equations, Chisholm arrived at the simpler form given by:

$$C = \left(\frac{1}{s} \right) \left(\frac{\rho_l}{\rho_g} \right)^{0.5} + s \left(\frac{\rho_g}{\rho_l} \right)^{0.5} \qquad\qquad 3.33$$

For the Martinelli model, the two-phase multiplier is based on the assumption that only liquid traveling at the liquid mass flux is present in the pipe.

$$\left(\frac{dP}{dz} \right)_l = \frac{2 f_l G_l^2}{d \rho_l} \qquad\qquad 3.34$$

$$\left(\frac{dP}{dz} \right)_{Pred} = \Phi_l^2 \left(\frac{dP}{dz} \right)_l \qquad\qquad 3.35$$

The determination of the pressure drop and two-phase multiplier for only gas traveling with the gas mass flux should also lead to the same total predicted pressure drop.

3.3.3 The Chisholm (1973) Model

The third separated flow model considered is the Chisholm model, which again uses the properties of the two phases to determine the two-phase multiplier. Baroczy (1965) developed an empirical correlation that was presented in graphical form, making it difficult to use. Chisholm (1973) applied a curve fit (equation 3.36) that has been found to best represent the Baroczy correlation (Hetsroni, 1982). As in the Martinelli number, n is taken as 0.25 for smooth pipes.

$$\Phi_{lo}^2 = 1 + \left(\Gamma_c^2 - 1 \right)\left[B x^{(2-n)/2} (1-x)^{(2-n)/2} + x^{2-n} \right] \qquad 3.36$$

where:

$$\Gamma_c^2 = \frac{\left(\dfrac{dP}{dz} \right)_{go}}{\left(\dfrac{dP}{dz} \right)_{lo}} = \left(\frac{\rho_l}{\rho_g} \right)\left(\frac{\mu_g}{\mu_l} \right)^n \qquad 3.37$$

The Baroczy correlation variable B can be found using equation 3.38, or using the table (Table 3.1) based on the correlation and proposed by Chisholm (1973).

$$B = \frac{\left(C\Gamma_c - 2^{2-n} + 2 \right)}{\left(\Gamma_c^2 - 1 \right)} \qquad 3.38$$

Table 3.1 Proposed values for variable B

Γ_c	G (kg/m^{2}s)	B
9.5	< 500	4.8
	500 to 1900	2400/G
	1900	$55/G^{1/2}$
9.5 to 28	600	$520/(\Gamma_c G^{1/2})$
	> 600	$21/\Gamma_c$
Γ_c 28	----------	$15000/(\Gamma_c^2 G^{1/2})$

While the table provides a quick reference, it tends to give conservative values for B, and will not be used in the analysis. As with the Friedel separated flow model, the predicted pressure drop can be determined by multiplying $\Phi_{LO}{}^2$ and the liquid only pressure drop value.

3.4 Recent Findings

Over the years numerous review papers comparing different pressure drop models have been published. Friedel compared 14 of the leading pressure drop models in 1980 and found that most models are only applicable to a narrow range of test parameters. Other comparisons have shown that prediction accuracy varies with flow regime, and to a lesser extent with liquid viscosity and pipe diameter (Nicholson et. al., 1978; Dukler et. al., 1964). Yet most predictive models fail to take flow regime into account, unless specifically developed for a particular flow regime. In a recent paper, Ferguson and Spedding (1995) summarized earlier model comparison findings:

"In Summary, tests on the available models for pressure loss prediction show that the models are dependent on flow regime. It is not possible to satisfactorily predict pressure drop for all flow regimes across the whole range of flow rates".

The importance of flow regime on pressure drop is also noted by Herm-Stapelberg and Mewes (1994), who report that in slug flow, liquid plugs moving at approximately the same velocity as the gas phase determines the frictional pressure drop. Further, as the liquid superficial velocity increases, the frequency of the slugs increases; however, only approximately one out of four slugs are stable, influencing pressure losses as the unstable slugs dissipate (Herm-Stapelberg and Mewes, 1994). Thus the authors' conclude that pressure loss is more easily and accurately predicted by calculating for specific flow patterns (Herm-Stapelberg and Mewes, 1994). Chen and Guo (1999) reached a similar conclusion in their study of three-phase air-oil-water flow in helically coiled tubes and straight pipes.

In order to account for flow regime effects on pressure drop models, Ferguson and Spedding (1995) compared 14 models for accuracy in predicting pressure drop for 31 specific flow regimes. Using a simple statistical technique to compare the models, they found several models that work well for a number of flow regimes. The Olujic (1985) model is suggested as the most useful because it attempts to predict pressure drop based on one of two defined flow regions (Ferguson and Spedding, 1995).

3.4.1 The Olujic (1985) Model

This model combines the two pressure drop models developed by Olujic and Moussalli, and Olujic and Chawla (Olujic, 1985). The data is divided into two regions (alpha and beta) based on the Froude number and the phase volume-flow ratio. When the gas phase velocity is much greater than the liquid phase velocity ($u_g \gg u_l$), the region is designated as alpha. The beta region is assigned when the velocities are approximately equal. In terms of flow regimes, the beta region represents plug and dispersed flow (low air flow rates), and the alpha region all others.

Considering first the beta region, the Moussalli and Chawla (1976) model developed for plug flow is used with a new friction factor form (3.48) developed by Olujic.

$$\left(\frac{dP}{dz}\right)_{\text{Pred}} = f\left(\frac{G^2}{2d\rho_l}\right)[1 + x(R-1)][1 - x(R-1)(K_2 - 1)] \qquad 3.39$$

In order to determine the friction factor and the last two terms, the volumetric flow rate, density, and viscosity ratios are required.

$$\beta = \frac{Q_l}{Q_g} \qquad 3.40$$

$$R = \frac{\rho_l}{\rho_g} \qquad 3.41$$

$$\theta = \frac{\mu_l}{\mu_g} \qquad 3.42$$

$$\mu_{TP} = \frac{\mu_l}{[1 - x(1 - \theta)]} \qquad 3.43$$

While there are numerous two-phase viscosity equations available, the Olujic two-phase

viscosity (3.43) is simply a rearrangement of the commonly used McAdams et. al. (1942)

two-phase viscosity equation.

$$\frac{1}{\mu_{TP}} = \frac{x}{\mu_g} + \frac{(1-x)}{\mu_l} \qquad 3.44$$

The Reynolds number, K_2, and friction factor can then be found.

$$Re = \frac{Gd}{\mu_{TP}} \qquad 3.45$$

$$K_2 = 1.2\left[\frac{(7+8n)(7+15n)}{(7+9n)(7+16n)}\right] \qquad 3.46$$

$$n = \left(\frac{0.671}{\beta}\right)\left[1 + (1+0.907\beta)^{1/2}\right] \qquad 3.47$$

$$f = \left\{-2\log\left[\frac{\frac{k}{d}}{3.7} - \frac{5.02}{Re}\log\left(\frac{\frac{k}{d}}{3.7} + \frac{14.5}{Re}\right)\right]\right\} \qquad 3.48$$

Equation 3.39 is identical to the homogeneous model (3.10) with the exception of the last

two terms and the definition of the friction factor, and should therefore give

approximately the same result. Applying the friction factor (3.48) defined by Olujic

(1985), however, resulted in large over-prediction of the pressure drop. The Olujic

friction factor appears to be an iterative equation similar in form to other friction factors

for turbulent flows in rough pipes; however, the second "f" term expected on the right-

hand side of the equation is not present. Ferguson and Spedding (1995) do not suggest an

alternative to equation 3.48, but do note the large prediction errors encountered in the beta region model. It is therefore suggested here, based on the similarity of the model to the homogeneous model, to use the Darcy and Blausis friction factors for laminar and turbulent flow, respectively.

$$f = \frac{64}{\text{Re}} \text{ if Re} < 2000 \qquad\qquad 3.49$$

$$f = \frac{3.164}{\text{Re}^{0.25}} \text{ if Re} > 2000 \qquad\qquad 3.50$$

The Chawla and Olujic (1979) pressure drop model is used for the alpha region. It requires the calculation of the two-phase parameters ε and Γ_o, defined as:

$$\Gamma_o = \left(\frac{1-x}{x}\right)\left[\frac{G^2(1-x)^2}{\rho_l g d}\right]^{-1/4} R^{-1/2}\theta^{-1/8} \qquad\qquad 3.51$$

$$\varepsilon_1 = 0.77 R^{-0.55}\Gamma_o^{X}$$
$$\varepsilon_2 = 2.19 R^{-0.61}\Gamma_o^{Y}$$
$$X = 0.266 R^{0.057}$$
$$Y = 1.78 R^{-0.078}$$
$$\varepsilon = (\varepsilon_1^{-3} + \varepsilon_2^{-3})^{-1/3} \qquad\qquad 3.52$$

The parameter Γ_o given by equation 3.51 is different to Γ_c given by equation 3.37, and should not be confused. The friction factor and superficial gas-phase pressure drop can then be found, and used to obtain the two-phase pressure drop.

$$f = 0.3164\left(\frac{Gxd}{\mu_g}\right)^{-1/4} \qquad\qquad 3.53$$

$$\left(\frac{dP}{dz}\right)_{SG} = f\left[\frac{(Gx)^2}{2d\rho_g}\right] \qquad\qquad 3.54$$

$$\left(\frac{dP}{dz}\right)_{Pred} = \left(\frac{dP}{dz}\right)_{SG} \left[1 + \frac{(1-x)}{x\varepsilon R}\right]^{19/8} \qquad 3.55$$

The criterion used by Olujic (1985) to determine the flow region, and therefore which model to apply, is given as:

$$\frac{1}{\beta} \leq \frac{12Fr^{1/2}}{1 + \dfrac{Fr^{1/2}}{7}} \qquad 3.56$$

If the relation is true, then the data point is in the beta region.

$$Fr = \left(\frac{Gx}{\rho_l}\right)^2 \left(\frac{R}{gd}\right) \qquad 3.57$$

The Froude number in this instance is the liquid-only Froude number.

Chapter Four: The Experimental Facility

This chapter provides details of the new air-oil two-phase test facility designed and constructed for the current research. A general overview is given, along with the specific instrumentation details. Problems encountered in the development phases are also discussed.

4.1 Overview of Test Facility

A new air/oil two-phase flow loop was designed and constructed for the present investigation (Figure 4.1). It is designed to accommodate multiple test section geometries over a wide range of operating parameters. The facility operates at low-pressure (up to 415 kPa), with maximum air and oil flow rates of 43.5 kg/hr and 2760 kg/hr, respectively (Table 4.1).

Table 4.1: Loop Operating Parameters

Prameter	Minimum	Maximum
Air Flow Rate	0.0 kg/hr	43.5 kg/hr
	(0 SCFH)	(600 SCFH)
Oil Flow Rate	9.2 kg/hr	2760 kg/hr
	(0.05 USGPM)	(15 USGPM)
Pressure	atm	415 kPa
		(60 psi)
Temperature	room	150°C

4.1.1 Loop Layout

The oil is stored in the tank (1), which also acts as a separation chamber for the air and the oil. The oil passes through a fine 100 mesh (0.0001") filter (2) before entering the

Figure 4.1: Diagram Of The Experimental Facility

1   TANK
2   OIL FILTER
3   PUMP
4   DRAIN FLOW METERS
5   OIL HEATER
6   OIL/AIR MIXER
7   AIR FILTER AND REGULATOR
8   AIR ROTAMETERS
9   AIR HEATER
10 TEST SECTION
11 COOLER
12 OIL MIST FILTER
13 PRESSSURE TRANSDUCERS
14 BYPASS
15 EXTRA TEST SECTION LINE
P   PRESSURE GAGE
TC THERMOCOUPLE
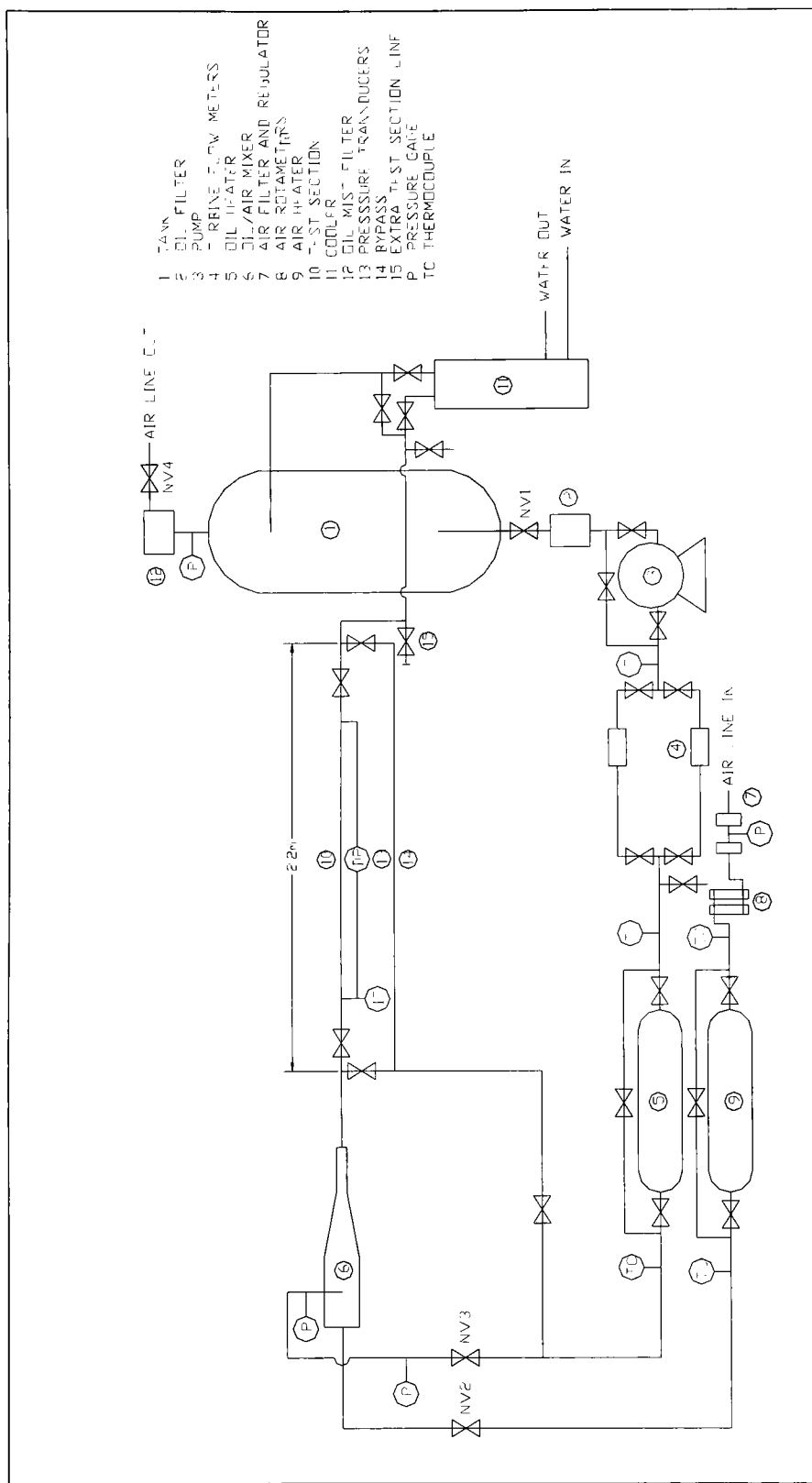
4180V-C-7 Tuthill 1800 RPM rotary gear pump (3), which is driven by a three-phase, 1 HP, 575V, 60 cycle electric motor. A Balador programmable speed controller is used to vary the power supplied to the motor, and thus the speed of the pump. A gate valve on a pump bypass line is used to regulate the amount of oil passing through the pump, allowing a finer control of the oil flow rate. A 100-psi house line provides the air for the system. The air is filtered and regulated (7) before entering the air/oil mixer (6). Electric heaters are installed on both the air and oil lines to permit operation at temperatures up to 150°C. The air heater is a single-phase, 4 kW heater (9) and the oil heater is a three-phase, 18 kW heater (5).

Once the air/oil mixture has passed through the test section (10), it can enter a cooler (11) or flow directly into the storage tank, where separation of the air and oil occurs. Finally an oil mist filter (12) removes any remaining oil in the air stream before it is vented to the outside. Figure 4.2 shows the actual experimental flow loop in the laboratory.

4.1.2 Mixers

The present 2" I.D. air/oil mixer (Figure 4.3a) is annular in design, with oil flowing around an inner1" I.D. perforated pipe. Air flows in the inner pipe and enters the oil stream through 380-1/32" dia. perforations. An earlier mixer (Figure 4.3b) of the same size was also annular in design; however, the oil and air were mixed abruptly at the open end of the inner pipe. This abrupt mixing resulted in a very unstable airflow, with large pressure spikes upstream of the mixer. The new mixer has been found to produce a steadier air/oil flow resulting in the elimination of the upstream air pressure spikes.

Power
Supply

Oil
Storage
Tank

Data
System

Video
Capture

Pressure
Trans.

Test
Section

Pressure
Tap
Lines
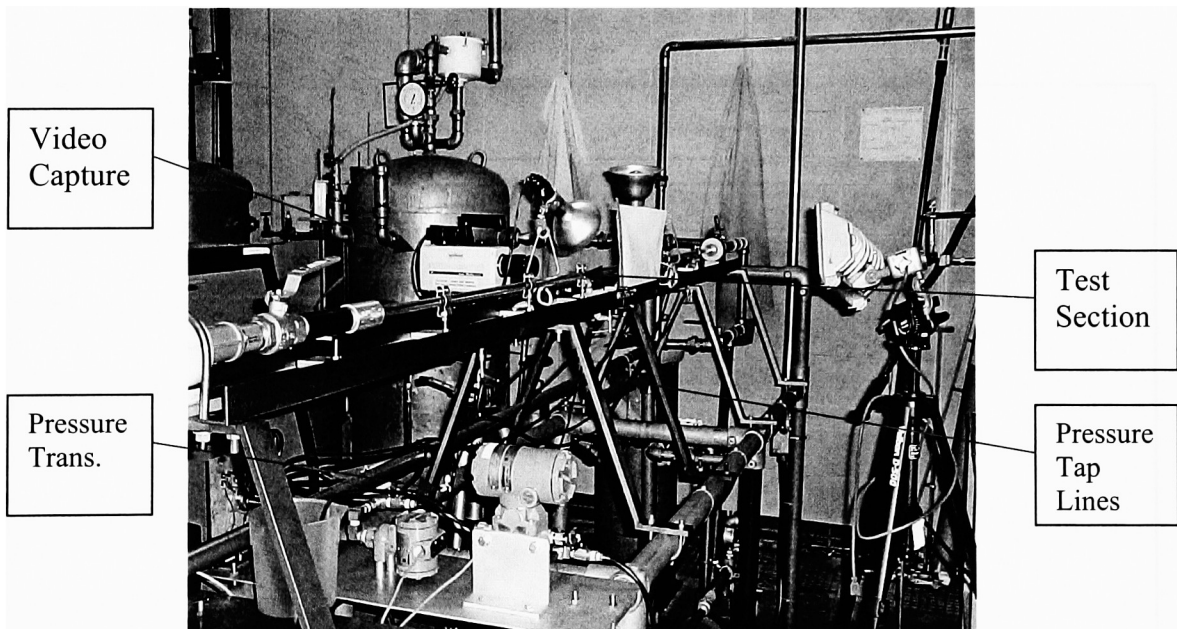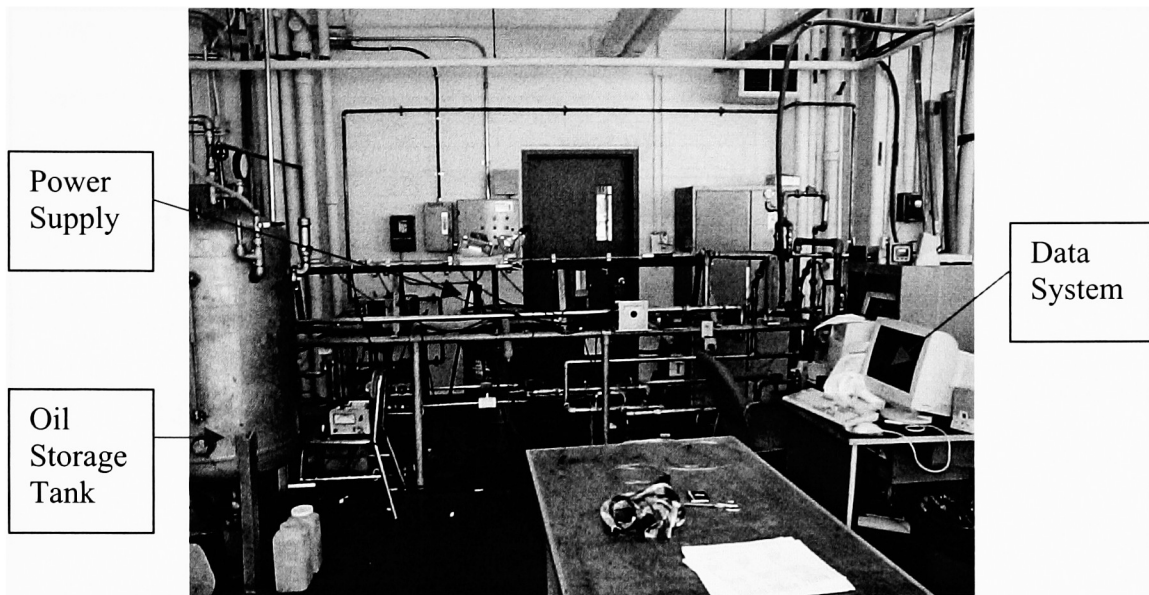
Figure 4.2: Pictures Of Test Facility
Top: View Of Full Facility
Bottom: Close-Up Of Test Section
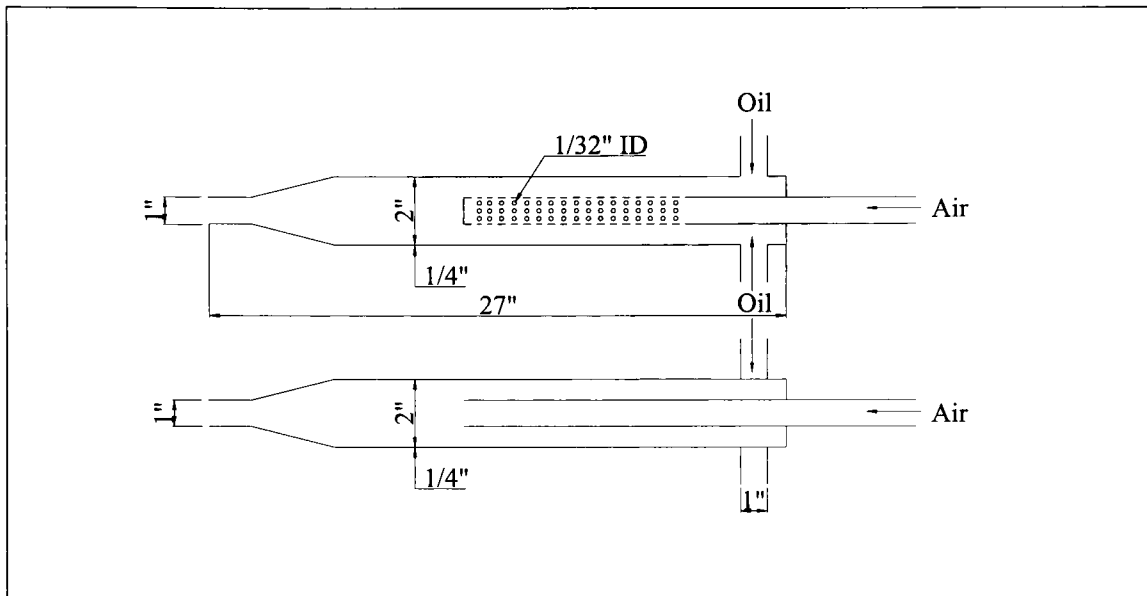
Figure 4.3: a) Current Mixer Design [Top]
b) Previous Mixer Design [Bottom]
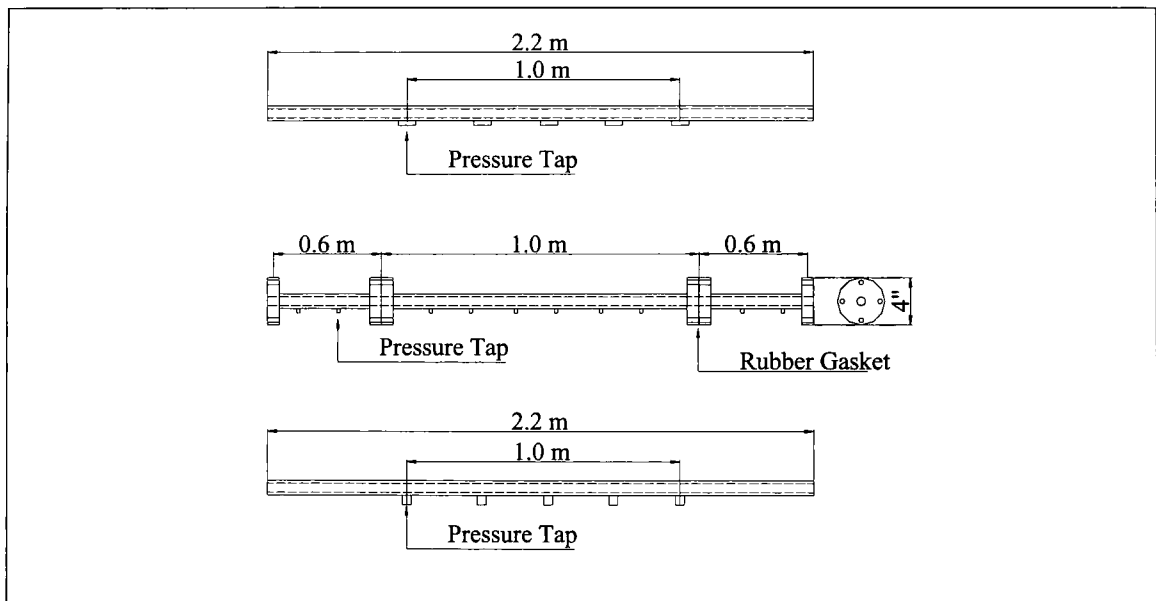
Figure 4.4: a) Current Test Section Design [Top]
b) First Test Section Design [Middle]
c) Second Test Section Design [Bottom]

Future phases of the program may use other mixer designs in order to compare mixing effectiveness. An initial study of the two mixers is presented in a later section of this thesis.

4.1.3 Test Section

Various piping configurations will be used throughout the test program, and the test section connections in the loop have been designed to accommodate a wide range of geometries. For this study, measurements were performed on a horizontal straight pipe section with a ½" inside diameter. The air/oil mixture is passed through an l/d = 73 section to allow flow regime development prior to entering the 1.0 m long test section (Figure 4.2). An l/d = 47 stabilization section follows immediately downstream of the test section. The entire test section is made of Lean® polycarbonate tubing to allow for complete flow visualization. In future phases aluminum test sections may be used to mimic the aero engine conditions, with view windows on either side of the test section to allow for flow visualization.

The present test section design (Figure 4.4a) is the culmination of results from testing done with two earlier designs that failed when installed on the loop. The first test section (Figure 4.4b) was made from acrylic and connected to the loop using flanges. This design failed in three ways; first the gaskets between the flanges allowed oil to leak out. Second the pressure taps were small tubes glued to the acrylic that easily broke off. Finally the flanges were too heavy for the test section tube, and it cracked under the weight. As a result of this last failure, the second test section design (Figure 4.4c) was

made out of lexan® plastic, which has triple the strength of acrylic. The flange design was replaced with a special tube holder (Figure 4.5) and the pressure taps were redone as plastic blocks. Failure of the second design occurred at the pressure taps (Figure 4.6a), which cracked because the plastic block was too thin. A correction was made to the pressure tap design (Figure 4.6b), leading to the present test section design. Additionally, Figure 4.7 shows the support frame for the entire test section that was added to ensure the test section was completely horizontal and straight.

4.1.4 Instrumentation Of Loop

The flow loop (Figure 4.1) has also been designed to accommodate changes to instrumentation as required by future test programs. Current measurements include air and oil flow rates, pressure drop along the test section, and fluid temperatures prior to the mixer. Two turbine flow meters (4) were used to measure the oil flow rates. The first is an OMEGA-FTB-791 turbine flow meter, with a range of 0.026 − 0.51 kg/s (0.5-10.0 USGPM), and an accuracy of ± 1% of the reading. The second is a Cole-Palmer 33110 low flow impeller sensor, with a range of 0.0036-0.2556 kg/s (0.07-5.0 GPM), and an accuracy of ± 1% of the full-scale reading. The two flow meters were installed in parallel to obtain the required resolution over the entire flow range.
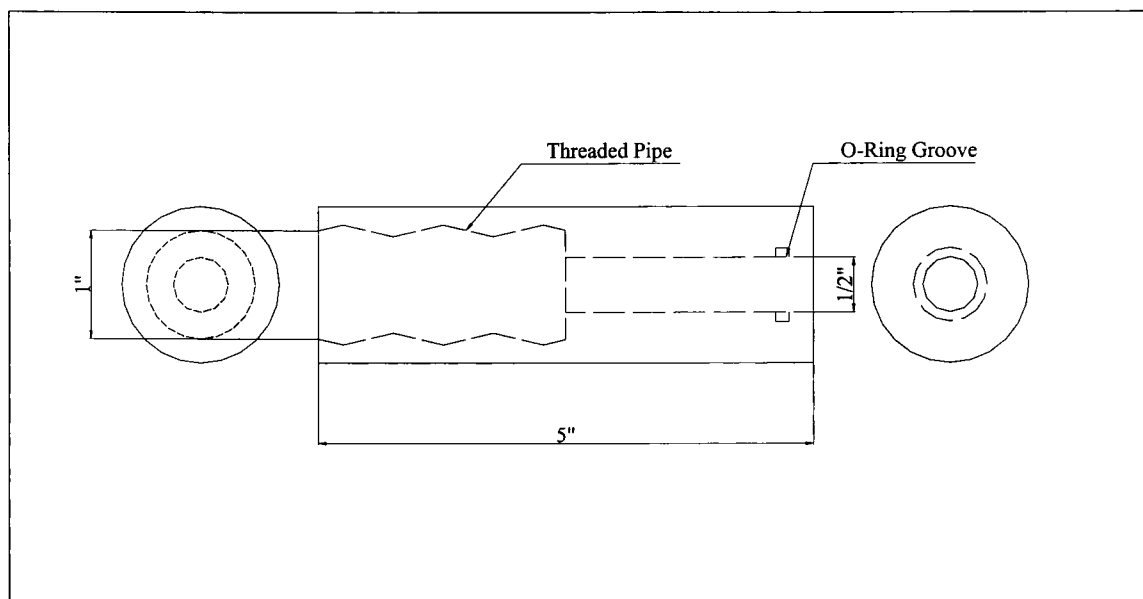
Figure 4.5: Special Test Section Tube Holder Design
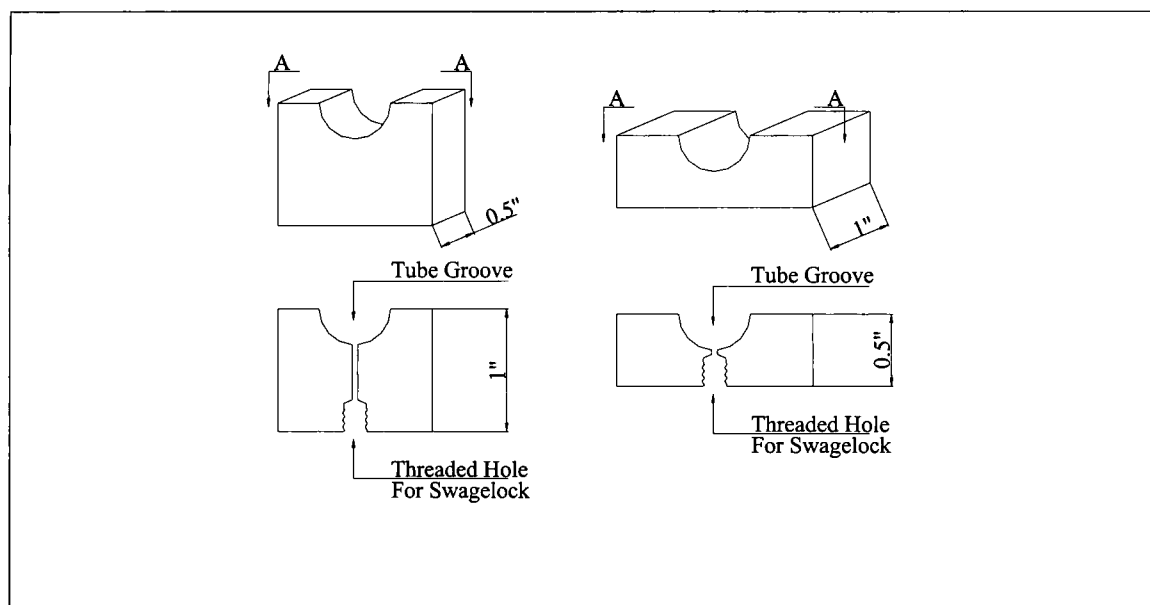
Figure 4.6: a) Original Pressure Tap Block Design [Left]
b) Current Pressure Tap Block Design [Right]
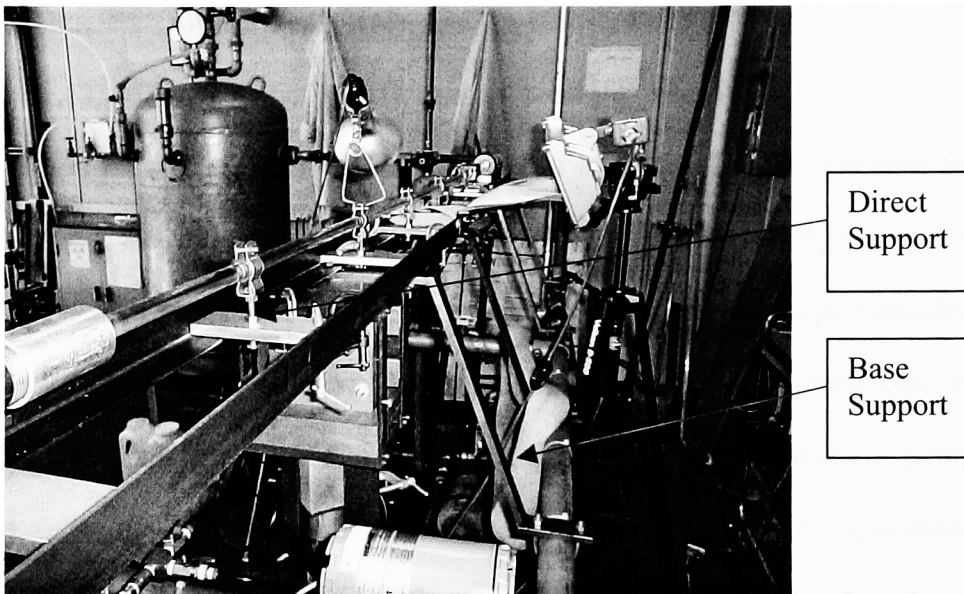
Figure 4.7: Test Section Supports

Figure 4.8: Scanivalve Pressure Wafer (From Above)

Four rotameters (8) in a bank were used to measure the airflow rates, with a range of 0.0 to 1.12E-02 kg/s (0-600 CFH), and an accuracy of ± 1% full scale. Two Rosemount pressure transducers (13) with an accuracy of ± 0.5% full scale were used for the measurement of the differential pressure and absolute pressure. A Scanivalve pressure wafer (Figure 4.8) was used to switch between the five pressure taps manually. Temperature was measured at various locations throughout the loop using type K thermocouples. Five standard liquid filled pressure gages were used to monitor pump pressure, inlet air pressure, inlet mixer conditions, and tank pressure. A capacitance meter to measure void fraction and identify flow regimes has been developed and recently installed on the test section. Chapter five discusses the development and preliminary results of the capacitance meter in detail. Currently flow regimes are identified by visual observation with the aid of a Kodak EKTAPRO 1000 frame/s high-speed video camera available in McMaster's two-phase flow laboratory.

4.1.5 Data Acquisition

While flow rates and pressure gage readings were manually recorded, the pressure drop, capacitance, and temperature measurements were recorded by a computer. The data was acquired using an AT-M10-16E-10DAQ board for the pressures and capacitance and a PCI-6034E board with SCB-68 connection block for the temperatures. All data was processed using National Instrument's LabVIEW software in a recorder program especially written for this research. The program allows the user to set the number of pressure taps and thermocouples to be read, the scan rate, number of samples,

and the output file path. For example 1000 samples at a scan rate of 10Hz could be taken for each of the pressure taps. The resolution of the reading is controlled by setting the voltage range recognized by the board, up to a maximum of ± 10 V. Both pressure transducers have an output voltage range of 0.8-4 V so a 0-5 V range was set for the board. This results in a 0.0012 V/bit resolution. Two other programs allow the monitoring of the instantaneous output signal from each device, and the recording of the instantaneous capacitance signal.

4.2 Calibration of the Instrumentation

In order to confirm the accuracy of the measurements, extensive calibration of the instrumentation was performed. The thermocouples and data acquisition board pre-set calibrations were confirmed using an ice bath and boiling water to test extreme conditions. More involved calibrations were required for the air and oil flow instruments, as well as the capacitance meter.

4.2.1 Air Flow Measurements

The air rotameters were calibrated in two steps. First air at a specific pressure was passed though a rotameter and then exhausted to the atmosphere through an orifice plate. For the high flow rate (0-400 SCFH) rotameter, a highly accurate water u-tube manometer was used to measure the pressure drop across the orifice plate for various airflow rates. This pressure drop was then compared against the orifice plate manufacture's pressure calibrations, and the airflow rate was determined. For the three

lower flow rate rotameters (two 0-90 CFH, one 0-10 CFH) a pressure transducer was used to measure the pressure drop. The transducer was calibrated for very low pressure drops, and outputed a voltage signal directly in mm H_2O (e.g. 0.020 VDC = 0.020 mm H_2O). Again the pressure drops recorded were compared against the orifice plate pressure calibrations to determine the airflow rate. No difference between the measured and listed air flow rate was found for the three lower flow rate rotameters, and therefore no correction factor was applied.

The second step in the air calibration was the correction for back pressure using the air pressure immediately downstream of the rotameter bank. Using equations 4.1 and 4.2 the mass flow rate can be determined.

$$Q_2 = Q_1 \sqrt{\frac{P_2}{P_1}}$$

4.1

$P_1 = atm$
$P_2 = P_{gage} + atm$

Q_1 = corrected volumetric flow rate determined in Step 1

$$m_g = Q_2 \rho_g$$

4.2

Since mass flow rate remains constant, regardless of area and density changes, it can be used to determine the velocity of the air at the test section entrance.

4.2.2 Oil Flow Measurements

The two turbine flow meters were calibrated by pumping the oil into a large container of known volume over the full range of flow rates. The time taken to fill the

same volume for each flow rate was compared with the calculated flow rate, and a calibration correlation was found. The turbine flow meters were then reset for the new calibration curve. Periodic recalibration of the turbine flow meters was performed to ensure the accuracy of the calibration.

4.2.3 Pressure Measurements

The pressure transducers pre-set calibrations were checked by recording the pressure drop for single-phase oil flow across the test section and comparing against the theoretically predicted pressure drop.

$$\frac{dP}{dZ} = \frac{f\rho_l V^2}{2d} \qquad\qquad 4.3$$

$$f = \frac{64}{Re} \quad \text{for Re<2000} \qquad\qquad 4.4$$

$$f = \frac{0.316}{Re^{0.25}} \quad \text{for Re>2000} \qquad\qquad 4.5$$

$$Re = \frac{Vd\rho_l}{\mu_l} \qquad\qquad 4.6$$

Several sampling frequencies and times were evaluated to determine the appropriate ones to obtain statistically steady values. It was found that the best results are given with 1000 voltage samples taken at 10 Hz (Figure 4.9).
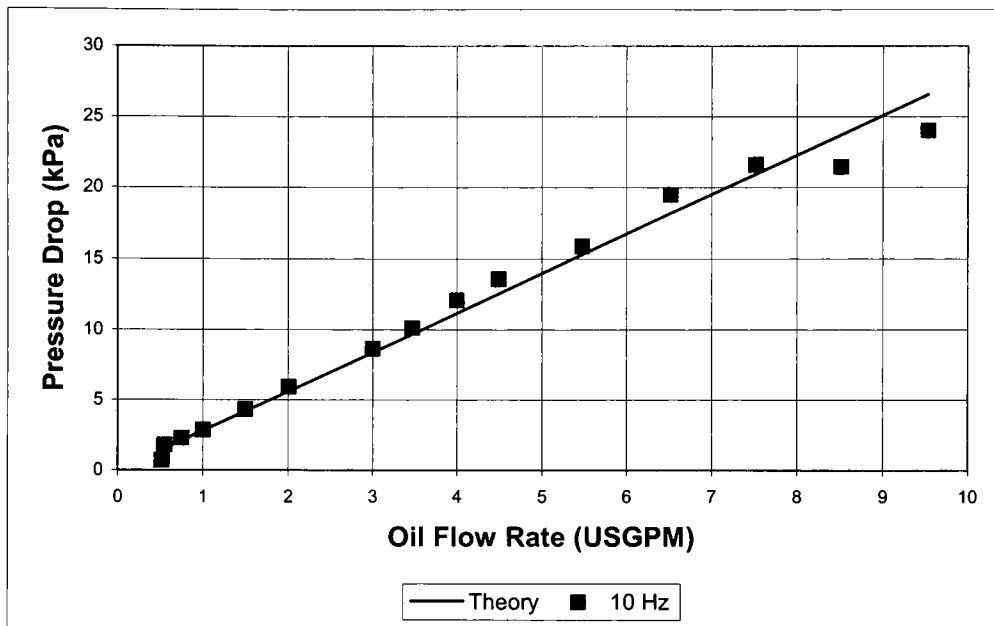
Figure 4.9: Single Phase Pressure Gradient Results

4.3 The Experimental Procedure

In order to ensure consistency in data collection, a specific series of steps were established. Starting from the loop being completely off, the following steps were taken.

1. Turn on the main power supply for the pump and heaters. Turn on the pump and set pump motor speed (oil flow rate), allowing the system to purge any air in the oil line. If the heaters were being used, the heater temperatures are also set and the heaters turned on.

2. Turn on data acquisition system and open the data recorder program. Set the number of points to be averaged, the frequency rate, and the direction path to save results to file.

3. The pressure tap lines were checked to make sure no air bubbles were present. The lines were purged if necessary.

4. Turn on the air supply, setting the pressure, and open the valve directly upstream of the mixer on the airline. Set the airflow rate. Allow the whole system to stabilize.

5. If using the high-speed camera, turn on the camera and check the settings. Also activate the computerized video recorder.

6. Start the data recorder program. Manually record the flow rates and pressure gauge values. An example of the data collection sheet is shown in Appendix A. Also start the video recorder, collecting both normal speed and slow motion video of the flow. Repeat steps 4-6 until all desired data points are collected.

7. Turn off the system starting with the camera and data acquisition systems. Shut off the air supply, closing the valve directly upstream of the mixer on the airline.

8. Stop the pump and if necessary the heaters. Finally turn off the main power supply.

All the data collected was transferred into a spreadsheet program for reduction and analysis.

4.4 Experimental Uncertainties

The different data acquisition instruments and their associated measurement errors are summarized in Table 4.2. Using the multivariate Taylor Series method, the uncertainties of various parameters can be quantified (see Appendix A). All major calculated values presented in this thesis are influenced by the uncertainties in the recorded pressures and mass flow rates (Table 4.3). Temperature was recorded to be 20°C for all experiments.

Table 4.2: Measurement Uncertainties

Device (Make, Type)	Minimum Uncertainty	Maximum Uncertainty
Oil Mass Flow Rate – TFM 1 (FTB-791, OMEGA turbine flow meter)	0.092 ± 0.0009 kg/s	0.323 ± 0.0032 kg/s
Oil Mass Flow Rate – TFM 2 (33110, Cole-Palmer low flow impeller)	0.026 ± 0.0003 kg/s	0.511 ± 0.0051 kg/s
Air Volume Flow Rate – Rots 1 to 3 (Cole-Palmer low flow rotameters)	0.000 ± 0.0000 m^3/s	$0.001 \pm 7.10\text{E-}06$ m^3/s
Air Volume Flow Rate – Rot 4 (Dysan)	0.000 ± 0.0000 m^3/s	$0.004 \pm 3.15\text{E-}05$ m^3/s
Inlet Pressure (2088, Rosemount Pressure Transmitter)	0.000 ± 0.000 kPa$_{gauge}$	413.0 ± 2.07 kPa$_{gauge}$
Differential Pressure (2024, Rosemount Pressure Transmitter)	0.000 ± 0.000 kPa$_{gauge}$	124.0 ± 0.62 kPa$_{gauge}$
Rotameter Pressure (liquid filled pressure gage)	0 ± 2.5 kPa$_{gauge}$	415 ± 5.0 kPa$_{gauge}$

Table 4.3: Error In Governing Parameters

Parameter		Error (%)
Oil Mass Flow Rate (all)		1.0
Air Mass Flow Rate	(min)	0.0
	(max)	7.1
Air Density (Rots)	(min)	0.0
	(max)	7.0
Air Density (Test)	(min)	0.0
	(max)	5.2

Chapter Five: Capacitance Sensor For Void Fraction Measurements

A capacitance sensor has been designed and developed to measure the instantaneous void fraction in air-oil two-phase flow. The calibration methods are described, and the signal processing tools used to identify the flow regimes introduced. Primary results for three commonly encountered flow regime transitions are then evaluated, and some preliminary recommendations made.

5.1 Theory Of Capacitance Measurement

Different methods of void fraction measurement were introduced and briefly discussed in Chapter 3. One method that has become increasingly popular is the capacitance sensor technique. The advantages of the capacitance sensor are the ability to capture fast transient phenomena without disrupting the flow while being relatively inexpensive to build (Chang et. al., 1995). While several different designs for capacitance sensors exist, the basic theory behind them is the same. All sensors can be modeled as a parallel plate capacitor where the capacitance is dependent on the area of the plates, distance between plates, and the dielectric constants of the phases. Dielectric constant of a fluid is related to capacitance by the equation:

$$\kappa = \frac{d_g C_{ap}}{A_p \varepsilon_o} \qquad\qquad 5.1$$

Since the electrode gap d_g, plate area A and permittivity of free space ε_o are fixed, variation in measured capacitance can be directly related to changes in the dielectric

58

constant of the fluid. As the volume ratio of the two phases changes, so does the dielectric constant of the mixture and the measured capacitance. Therefore the void fraction of the mixture can be directly related to variations in the capacitance recorded by the sensor.

5.2 Capacitance Sensor Design

The two most common capacitance sensor designs for use on round tubes are helically coiled electrodes and ring electrodes in series (Elkow and Rezkallah, 1996; Abdul-Razzak et. al., 1995). Figure 5.1 and 5.2 illustrate these two basic designs. For the helically coiled electrode model, the placement of guard electrodes to minimize edge effects and stray capacitance is very important (Geraets and Borst, 1988). This can make the design of such a sensor more complicated. The same is not true with the coiled ring design, as the entire sensor can simply be shielded to prevent stray capacitance and edge effects. Both types of sensors have been proven to produce accurate measurements of void fraction. Based on previous work conducted in the McMaster Two-Phase Flow Laboratory, the ring type sensor was selected for the current project.

Figure 5.3 shows the current sensor design developed for this project. The advantage of this design is the simplicity of fabrication and low material costs. Three sets of copper electrodes connected in parallel measure capacitance as shown in Figure 5.4a. The electrodes are housed in two pieces of acrylic to allow direct mounting on the test section. The sensor is shielded by completely covering the acrylic housing with copper tape, which is grounded, eliminating environmental capacitance interference.

This method of shielding reduced the effect of stray capacitance on the sensor output signal from ± 1-5 pF to ± 0.01-0.03 pF, as measured on a Booton-72B capacitance transducer (± 0.5% accuracy full scale).
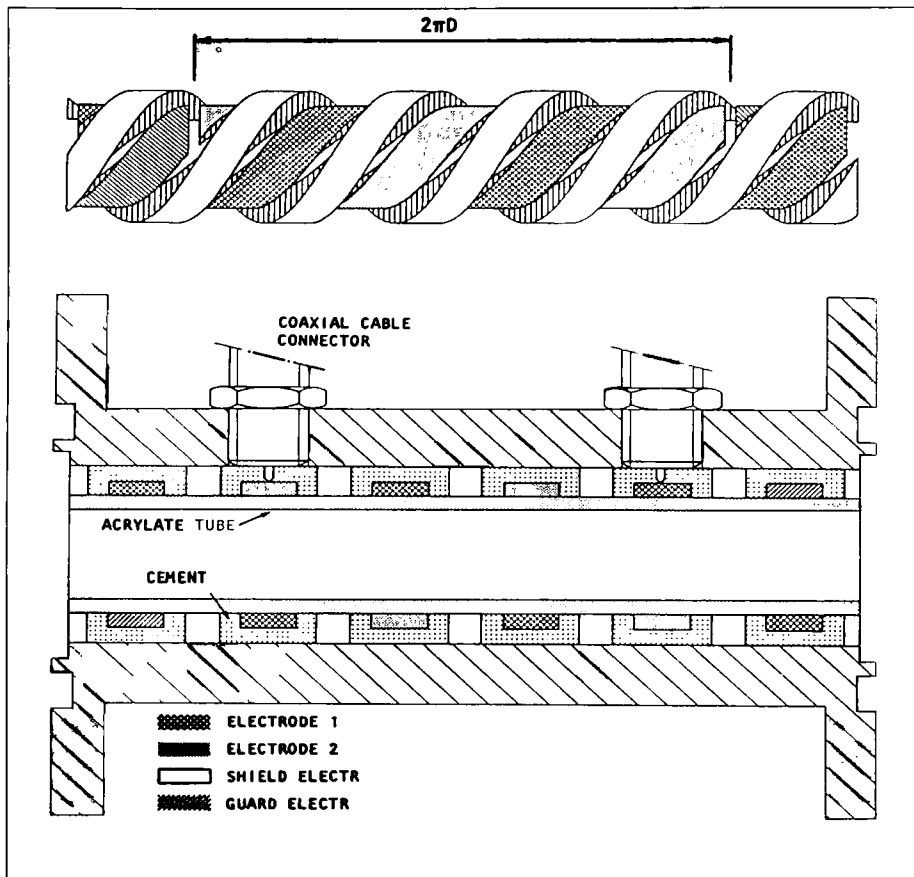
Figure 5.1: Helically Coiled Capacitance Sensor (Geraets and Borst, 1988)
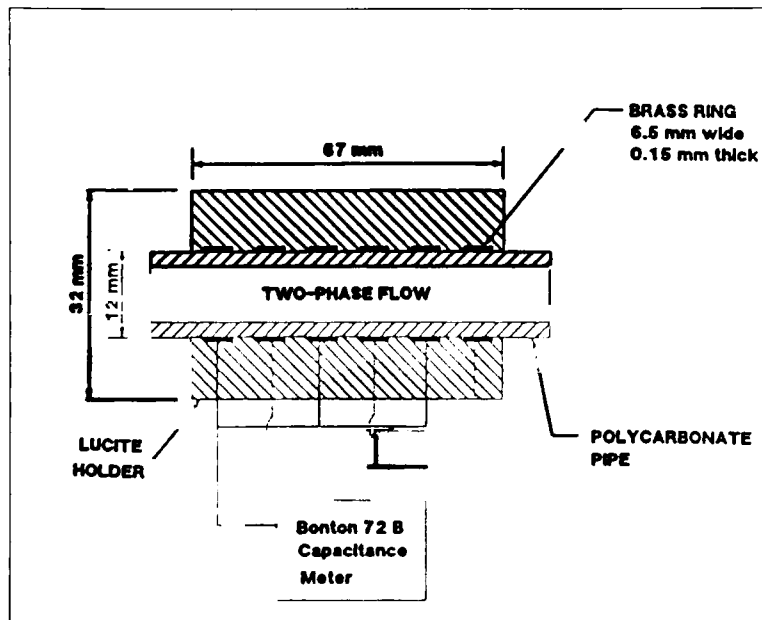
Figure 5.2: Ring Capacitance Sensor (Abdul-Razzak et. al., 1995)
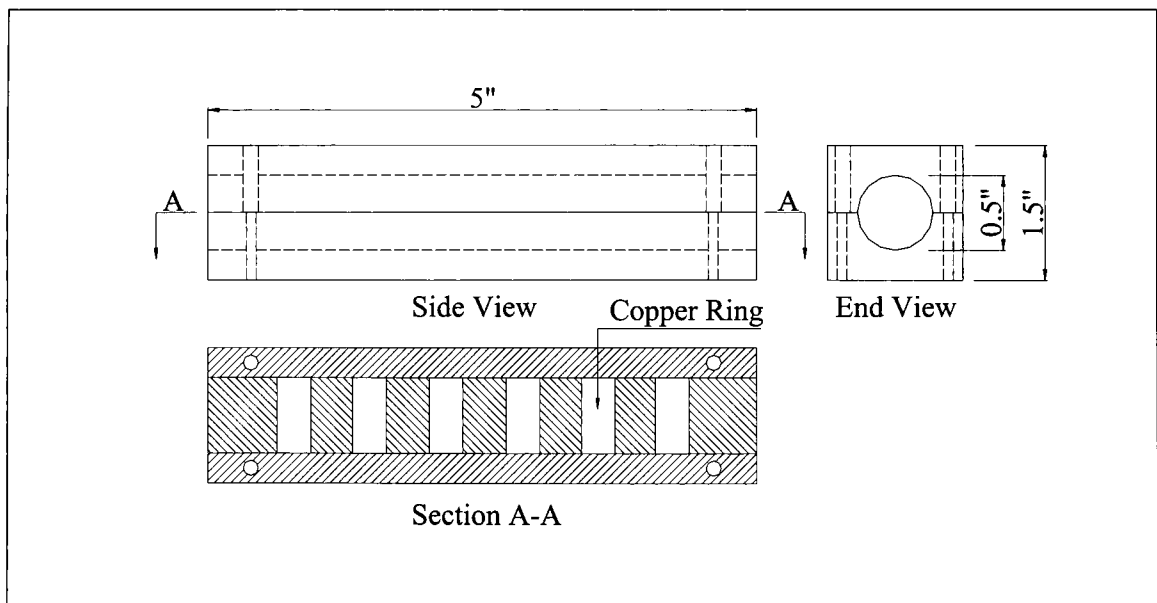
Figure 5.3: Capacitance Sensor Design For Present Project
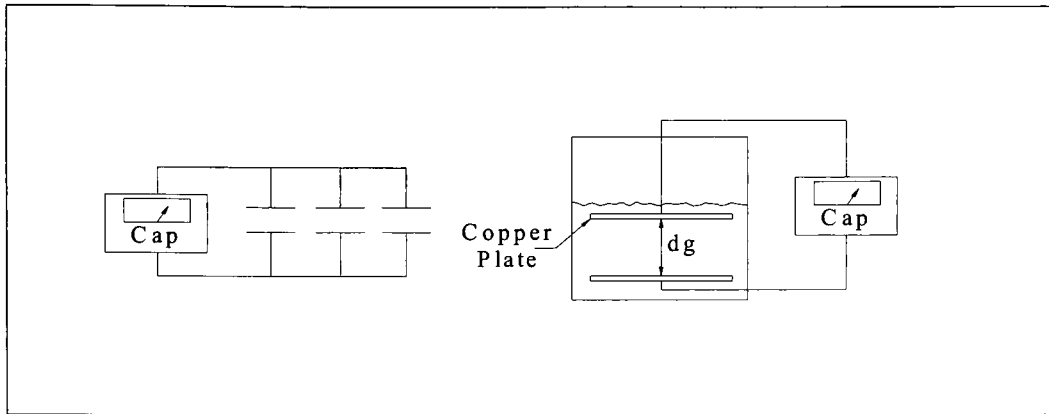
Figure 5.4: a) Electric Schematic For Rings [Left]
b) Oil Dielectric Constant Apparatus [Right]

5.3 Calibration Of The Capacitance Sensor

Calibration of the capacitance sensor was performed in three steps:

1) Determination of the dielectric constant of the specific oil being used.

2) Determination of the effect of flow regimes on the measured capacitance, if any.

3) Online calibration to determine the response of the sensor.

These three steps will be described in detail in the following sub-sections.

5.3.1 Dielectric Constant Of Oil

In order to calibrate the capacitance sensor, the dielectric constant of the ESSO 2380 turbine oil used in the test facility had to be determined. A dielectric is defined simply as a non-conducting material. Each dielectric material has a unique constant value, which is generally determined by placing the material between two parallel, electrically charged plates. Information provided by the supplier gave the dielectric constant for oil at 150°C; however, the dielectric constant does not change linearly with temperature. Therefore a simple extrapolation to 20°C was not possible. A simple apparatus consisting of two copper discs suspended in a container was constructed to

determine the dielectric constant (Figure 5.4b). The container was filled with oil, and the distance between the plates was varied while the capacitance between the plates was measured with the Booton-72B capacitance transducer. Rearranging equation 5.1 into the form:

$$\frac{d_g}{\kappa} = \frac{A_p \varepsilon_o}{C_{ap}}$$

5.2

the distance between the plates was plotted against the value of the right-hand side of equation 5.2. A linear fit was then applied to the data, with the slope of the line being equal to the dielectric constant of the oil (Figure 5.5). Testing both year old oil and new oil, the dielectric constant of oil was determined to be $\kappa = 5.45$.

5.3.2 Effect Of Flow Regime On Sensor

To determine the effect of flow regimes, if any, on the sensor an off-line calibration was conducted. Since the sensor should produce a different capacitance trace for different flow regimes, an off-line calibration provides a first check to assure the sensor is working correctly. To simplify the test and allow for easy measurement of different flow regimes, a solid material was selected to mimic the oil. Phenolic, a plastic material with the same dielectric constant as the oil was selected for its ease of machining and availability in the required diameter.

The stratified and annular flow regimes were simulated using the Phenolic due to the simplicity in fabricating these regime shapes. Eight annular and eleven stratified pieces with different volumes and cross-sectional areas to simulate different void

fractions were machined out of the Phenolic. Figure 5.6 shows the results of the calibration, with a linear least square regression applied for each regime. The difference between the two calibration lines is about 8%, indicating a small sensitivity to the flow regime in the capacitance measurement. These results are in agreement with those of Chang et. al. (1995). The offline testing also indicated a capacitance range from 0.2 pF for total air to 0.87 pF for total Phenolic (oil) in the tube.
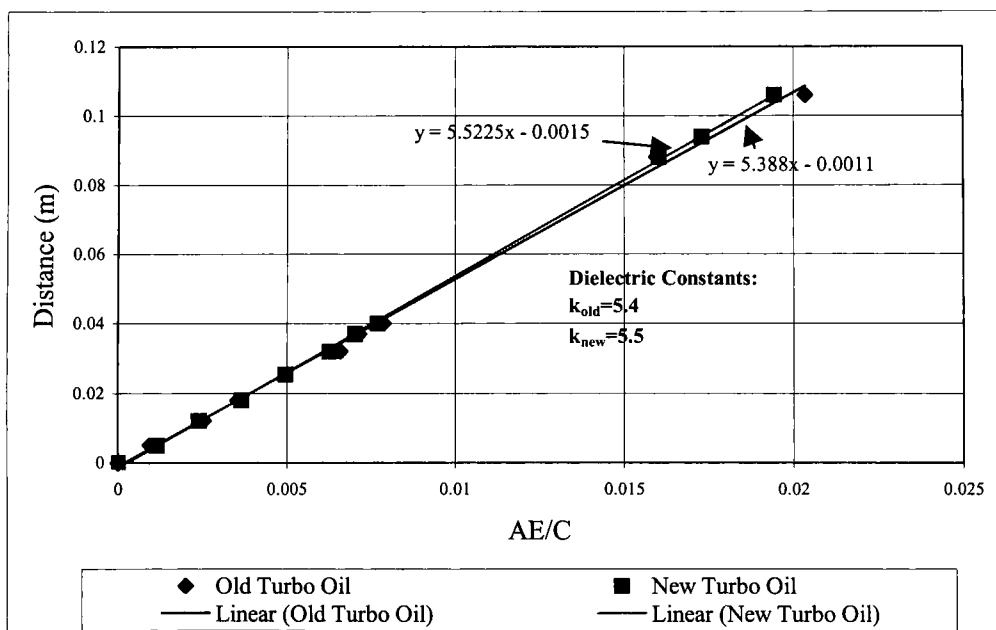
Figure 5.5: Oil Dielectric Constant Results
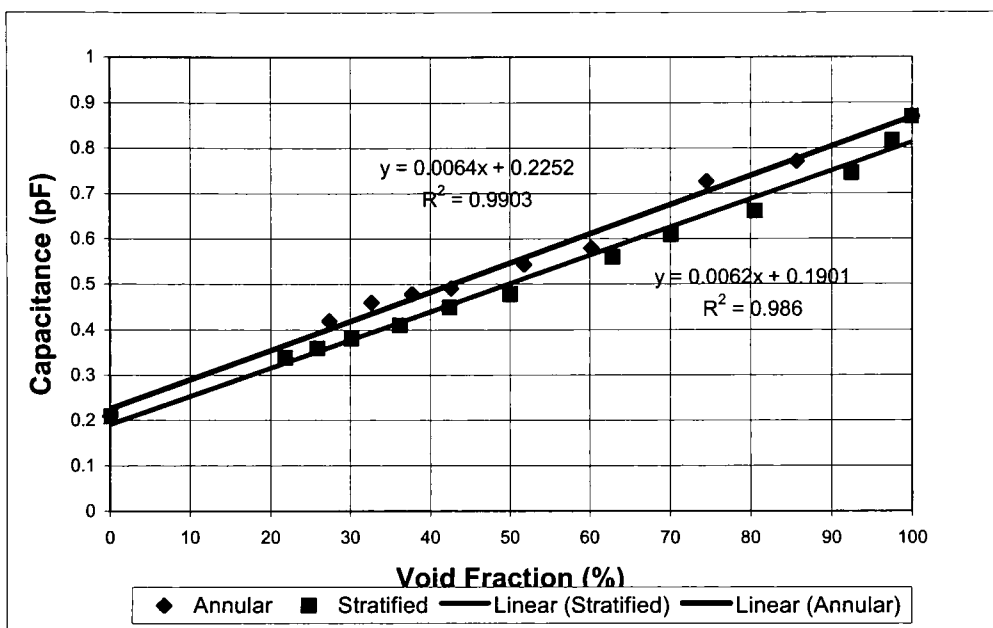
Figure 5.6: Offline Calibration Results
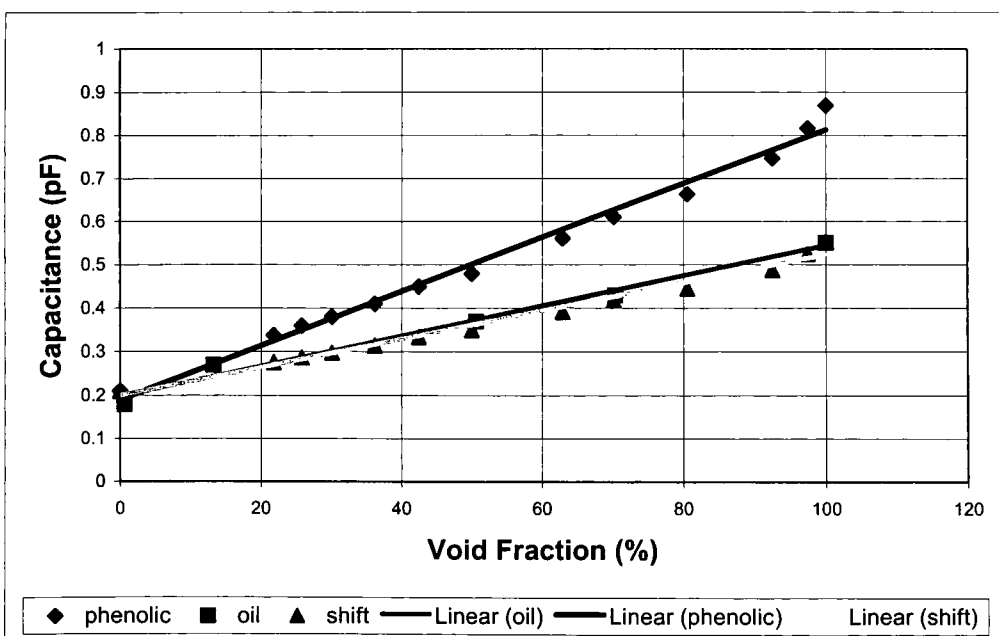
Figure 5.7: Online Static Calibration Results

5.3.3 Online Calibration Of Sensor

The final step in the calibration was to install the sensor on the test section to measure the capacitance of the air and oil online. The measurements were found to be 0.18 pF for all air and 0.55 pF for all oil in the tube. These results are different to those from the offline calibration, but were determined to be a result of different dielectric constants for the oil and Phenolic. While the dielectric constant of most materials is measured at a high frequency, the oil dielectric constant was measured at a frequency of 60 Hz. As the frequency applied by the capacitance meter is increased, the current passing through the material increases. This decreases the ability of the material to retard flow of charge between the two plates, decreasing the potential difference (capacitance) between the two plates. Since the dielectric constant of a material is directly proportional to the capacitance, the dielectric constant also decreases. Therefore, if Phenolic has a dielectric constant of $\kappa = 5.45$ at 1000 Hz, than the value would be higher at 60 Hz.

As a corrective measure for the dielectric constant discrepancy, the stratified flow regime results were projected onto a new trendline from 0.18-0.55 pF. Online static stratified flow regime data points were then taken, and the new results were found to have good agreement with the offline results (Figure 5.7). Dynamic measurements for the two limiting conditions of air and oil only were then taken, and the range was found to be 0.18 to 0.55 pF (Figure 5.8). This is in complete agreement with the static calibration and indicates that the sensor is not affected by the running of the flow loop. To check the response of the sensor, tests were conducted over a wide range of flow conditions using
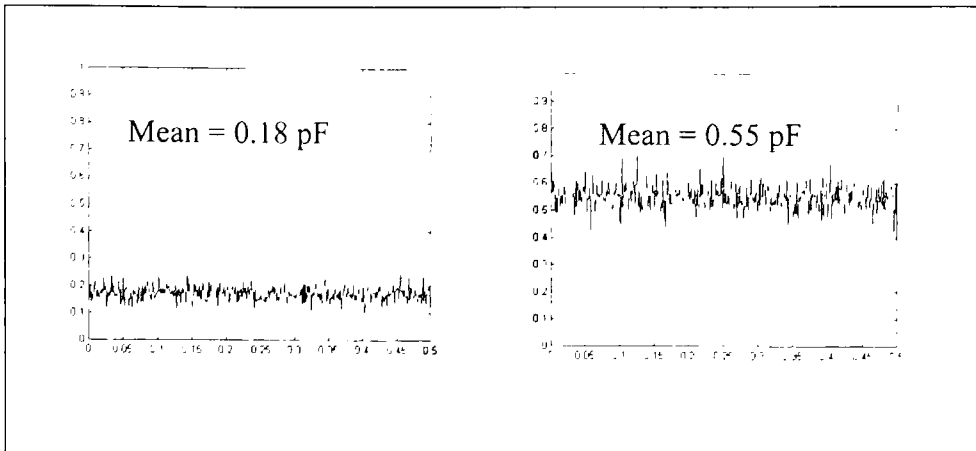
Figure 5.8: a) Capacitance Time Trace For All Air
b) Capacitance Time Trace For All Oil

several sampling frequencies. It was found that a sampling frequency of 1000 Hz was

sufficient to resolve the dynamic characteristics of the flow in this instance.

5.4 Signal Processing

One objective of the thesis was to develop flow regime identification techniques

using the dynamic capacitance signal. The mean, variance, power spectral density (PSD),

and probability density function (PDF) of the signal can be used to develop criteria for

flow regime identification. The signal processing techniques were developed by an

undergraduate research assistant as a separate project. These techniques are presented

here as reference for the discussion of the results in the next section, which is a

component of this thesis.
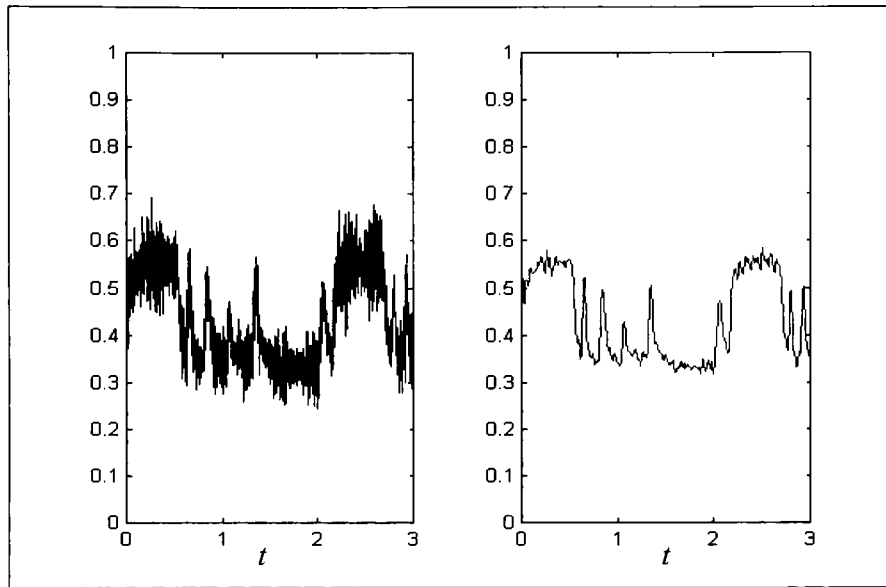
Figure 5.9: Example Of Signal Filtering Effect

5.4.1 Signal Filtering

Prior to any data analysis, the capacitance signals are digitally filtered using a wavelet-based filter applying an existing MatLab program code. This removes the high-frequency noise without affecting the dynamic characteristics of the signal. An example of the filtering is shown in Figure 5.9.

5.4.2 Power Spectral Density

While the filtered instantaneous capacitance signal often shows distinct patterns for certain flow regimes, allowing for relatively easy identification, this is not always the case. In order to better interpret the instantaneous capacitance signal, the power spectral density of the signal can be examined. This is accomplished by applying a Fourier transform to the data:

$$R_{cc}(\tau) =_T \lim_{\longrightarrow \infty} \frac{1}{T} \int_0^T C(t)C(t+\tau)dt \qquad\qquad 5.3$$

$$PSD(f) = 4 \int_0^\infty R_{cc}(\tau)\cos(2\pi f \tau)d\tau \qquad\qquad 5.4$$

The resulting power spectral density is shown in Figure 5.10. Hubbard and Dukler (1966) have shown that by examining the dominant frequency, if any, the flow regime can be identified.

5.4.3 Probability Density Function

Another useful tool for distinguishing the flow regime is the probability density function (PDF) of the void fraction signal. The void fraction can be obtained from the capacitance signal by applying the relation:

$$\alpha = \frac{C_{oil} - C_{measured}}{C_{oil} - C_{air}} \qquad\qquad 5.5$$

where:

C_{oil} = 0.55 pF
C_{air} = 0.18 pF

The PDF is shown in Figure 5.11, and the range and location of the peaks can be used to identify the flow regimes.
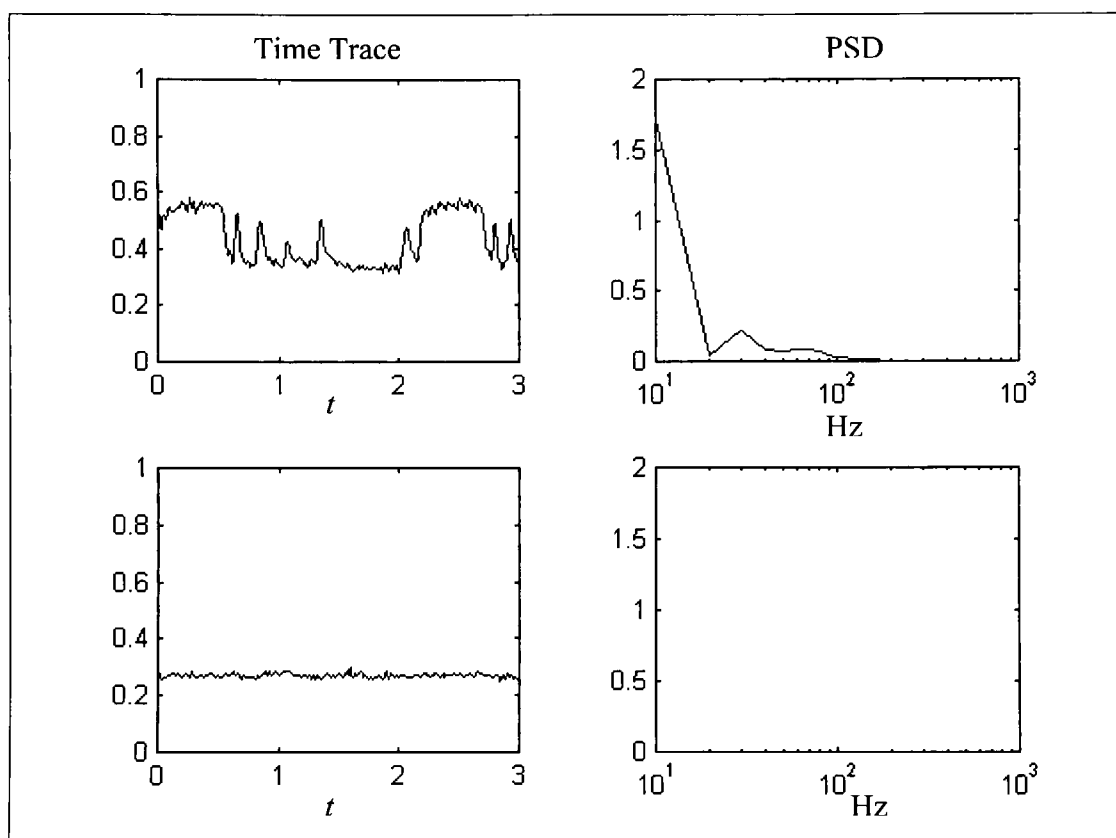
Figure 5.10: a) Example of PSD for Slug Flow [Top]
b) Example of PSD for Annular Flow [Bottom]
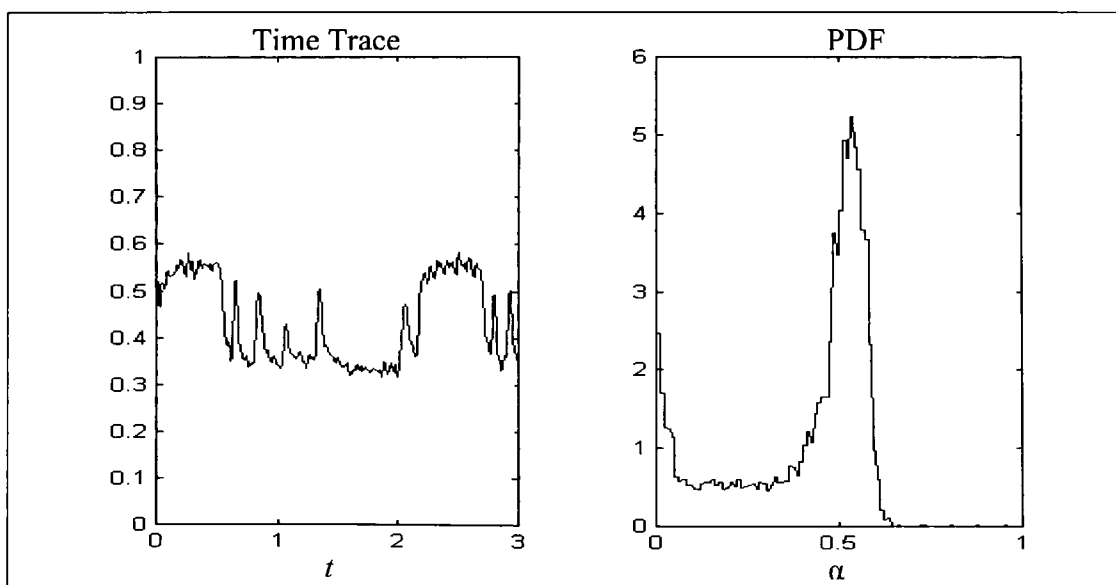
Figure 5.11: Example of PDF of Slug Flow

5.5 Discussion of Capacitance Sensor Results

The capacitance signals for transitions from slug to plug, slug to wavy, and slug to annular were investigated to develop a flow regime identification technique. These three transitions were chosen due to the ease of identifying each flow regime visually, which allows confirmation of the capacitance sensor results. For each transition case, three measurements were obtained, two within the flow regimes, and the third within the transitional zone.
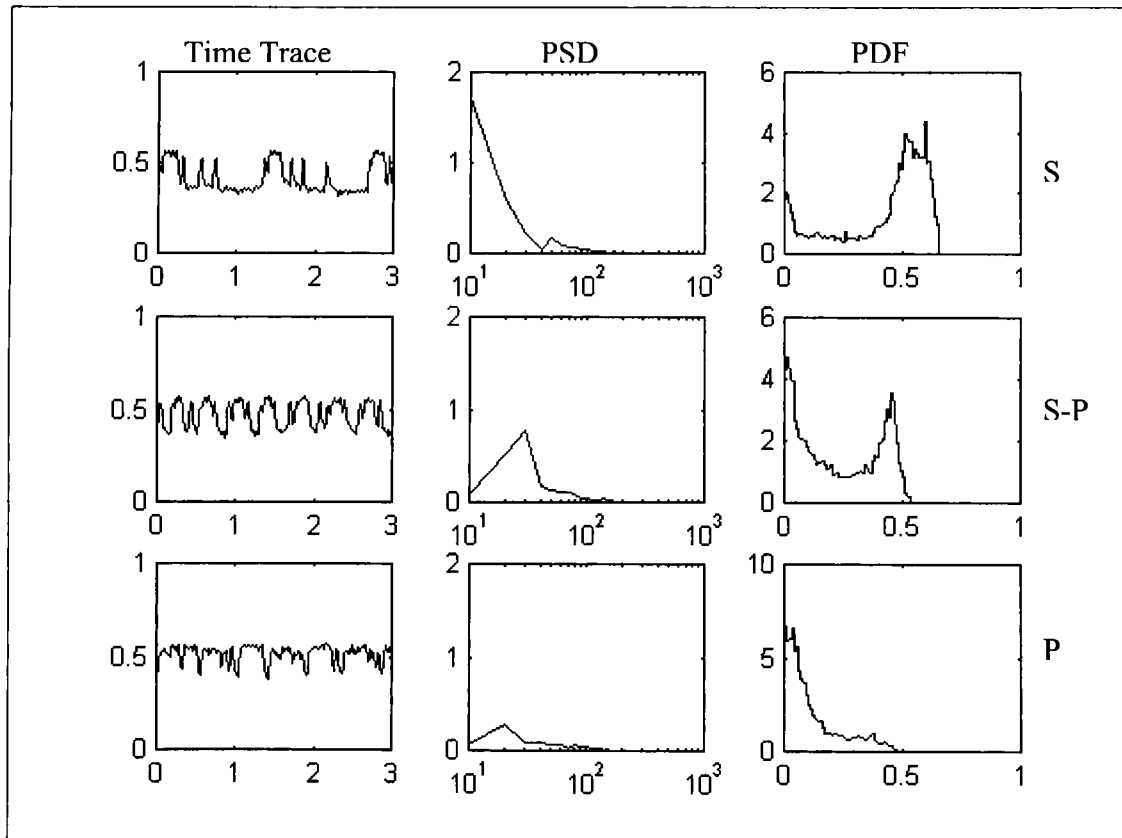
Figure 5.12: Transition From Slug To Plug Results

5.5.1 Slug To Plug Transition

The time traces for transition between slug and plug flow (Figure 5.12) are similar in appearance and indicate that both flow regimes exhibit some periodicity, with capacitance mean values increasing from 0.4 to 0.5 pF as the transition progresses. The PSD and PDF of the time traces, however, clearly show very distinct characteristics. A distinct decreasing PSD trace is observed for slug flow, while plug flow has a small frequency peak at about 20 Hz. The transitional PSD (middle) shows a slightly higher peak at about 30 Hz and elements of the other two PSD graphs.

For the PDF of slug flow, two peaks are observed: a larger one at a void fraction of about 0.5, and a smaller one at a very low void fraction. Plug flow has a much larger single peak at a very low void fraction (approximately 0.1). The transitional PDF shows characteristics of the both regimes, with two peaks at void fractions of about 0.1 and 0.45. Lowe and Rezkallah (1999) observed very similar results from capacitance signals in vertical upwards two-phase slug flow. This suggests that a slug flow PDF can be characterized as having two peaks, a small one at low void fraction, and a much larger one at higher void fractions. The low void fraction peak represents the tube when filled with oil, which occurs when a slug passes the sensor. The higher void fraction represents the flow regime the rest of the time, when the tube contains both air and oil in a stratified type of flow. By similar interpretation, the plug flow PDF has a peak at low void fraction as a result of the tube being filled with oil most of the time.
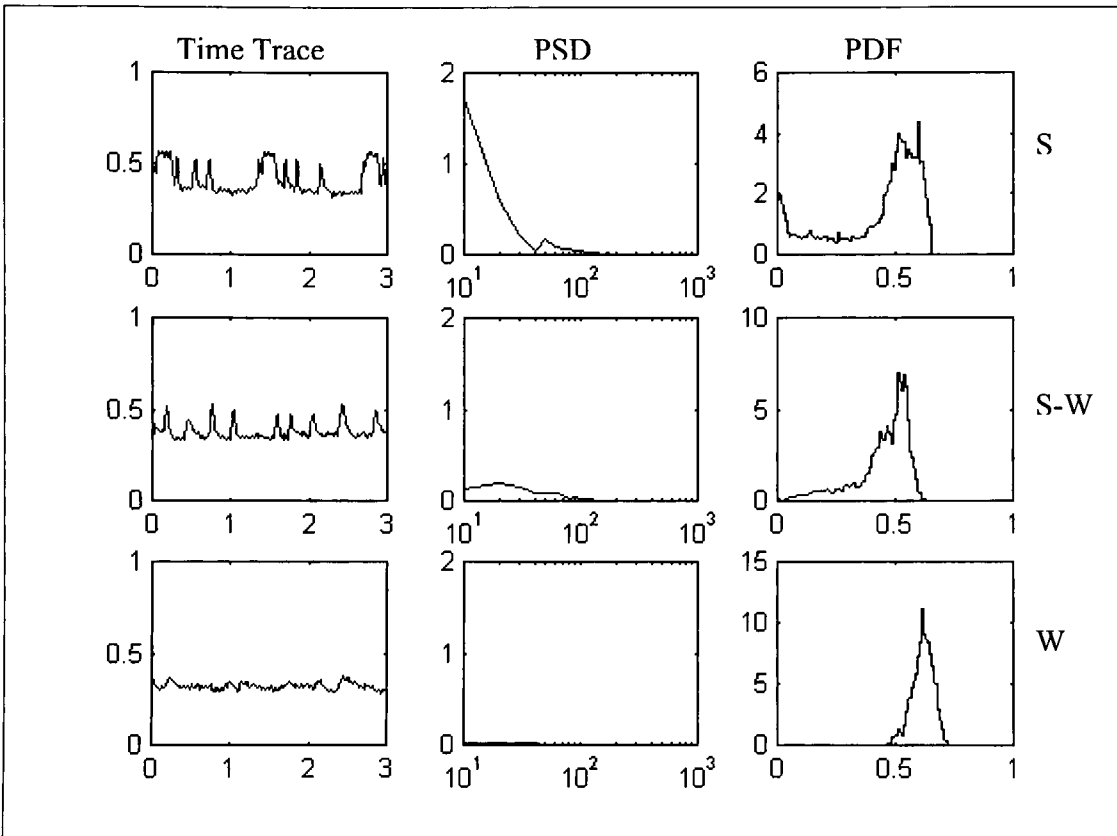
Figure 5.13: Transition From Slug To Wavy Transition Results

5.5.2 Slug to Wavy Transition

A transition from slug to wavy flow is presented in Figure 5.13, with the time trace for the wavy flow showing a significant difference to that of the slug flow. The slug flow characteristics were discussed in the previous section; and therefore are not addressed here. The mean capacitance decreases from 0.4 to 0.3 pF as the transition occurs, which is expected because air is the larger phase by volume in wavy flow. This wavy flow was also very uniform, with relatively small waves (about 3 mm high) passing the sensor at timed intervals of less than 1 second. A high-speed video was used to determine the height and frequency of the waves. The PSD reflects this uniformity,

showing no dominant frequency. Transition between the two regimes again shows characteristics of both slug and wavy flow, with some frequency data on the PSD but no dominant frequency.

For this transition, the PDF is more useful than the PSD, as it provides more detail on the flow regimes. The wavy flow has a single large peak with low variance at an approximate void fraction of 0.6, while the transition shows a dominant peak at a void fraction of about 0.5, but with a much wider variance over lower values. The transition from slug to wavy flow results in an increase in the amount of air present in the tube, and therefore an increase in the void fraction. This result is in agreement with capacitance sensor PDF results presented in the literature (Lowe and Rezkallah, 1999; Das and Pattanayak, 1994)

5.5.3 Slug to Annular Transition

Figure 5.14 shows the third transition, slug to annular flow, examined in order to evaluate the capacitance sensor. As with the previous two flow transitions, the same slug flow data is being used to provide consistency in the comparisons. The annular flow regime, which is predominantly air, is clearly shown in the time trace and PSD results. The time trace signal is steady with a very low variance. The mean capacitance of the annular flow is 0.27 pF, which is approaching the lower limit of 0.18 pF for all air. There is no dominant frequency, as shown in the PSD; and the PDF shows only one, very pronounced peak at a void fraction of about 0.75. As expected, the transition regime has characteristics of both flow regimes, with a slightly dominant frequency of 20 Hz (with

slug flow having 10 Hz and annular flow having no dominant frequency) on the PSD.

The peak void fraction for the transitional zone occurs at about 0.65, which lies between

the 0.5 of slug flow and the 0.75 of annular flow. Unlike annular flow, which has a very

narrow PDF variance, the transitional flow has a wider variance similar to the slug PDF.
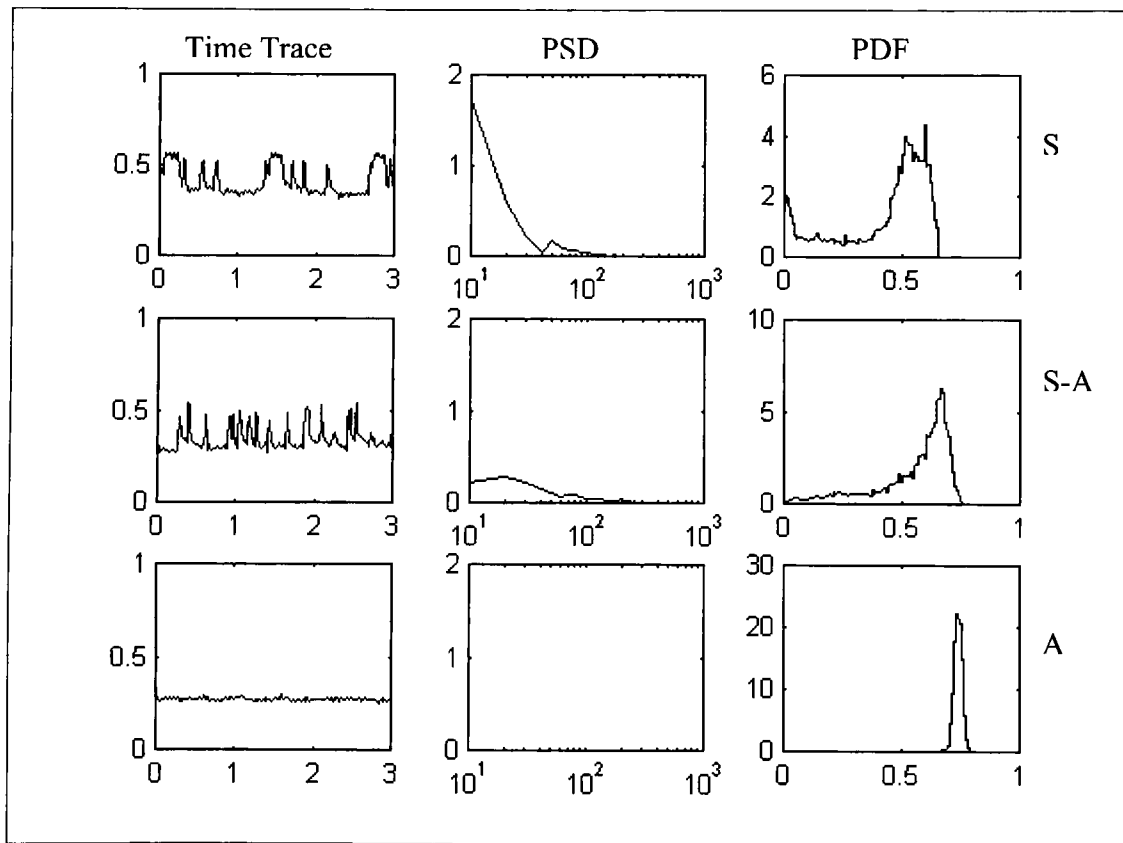
Figure 5.14: Transition From Slug To Annular Results

5.6 Preliminary Recommendations

The capacitance sensor was developed as a tool for measuring instantaneous void fraction and identifying flow regimes. Equation 5.5 provides a simple method to determine the instantaneous void fraction from the capacitance signal. Using the mean, variance, power spectral density (PSD), and probability density function (PDF) of the capacitance signal, flow regimes can be identified. A computer algorithm or a Neural Network could be developed as a tool for flow regime identification. A flow chart of a possible algorithm is illustrated in Figure 5.15. The PSD could first be used to separate the data based on the peak power density of the signal. Based on the flow regime data studied to date, a suggest range is proposed. The mean and variance could then be used to further separate the data into possible flow regimes, with a PDF qualifier providing the final decision on the flow regime. The development of such an algorithm is left for a future project.
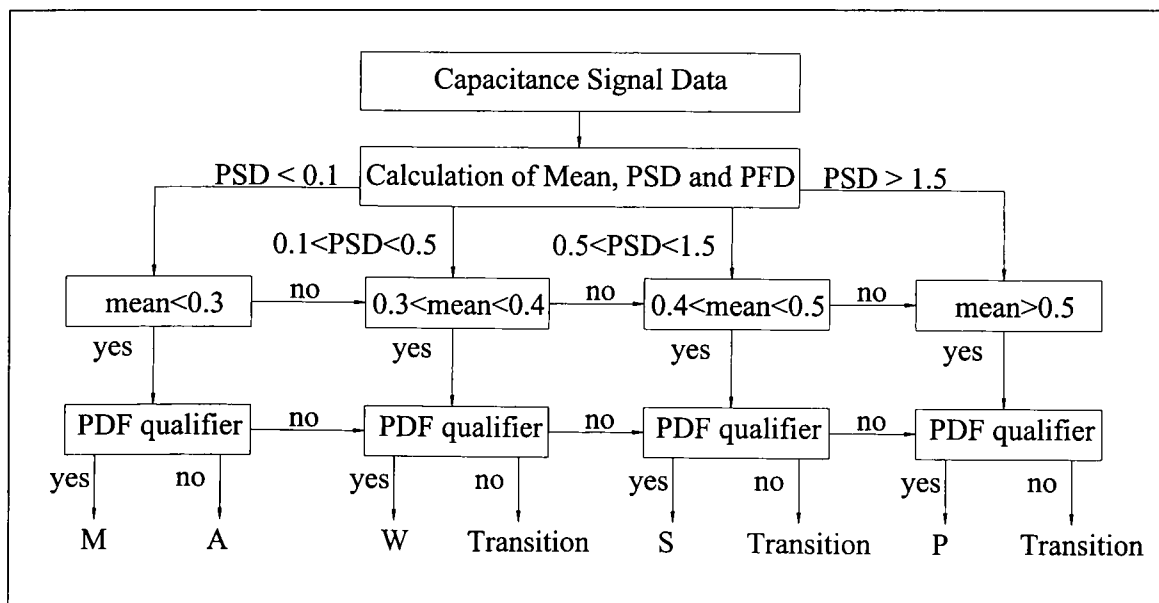
Figure 5.15: Form Of Possible Algorithm For Flow Regime Identification

Chapter Six: Flow Map Results

The flow regime mapping results obtained with the aid of the Kodak EKTAPRO high-speed video camera and software are reported in this chapter. The volumetric flow rates of both phases were recorded and converted into superficial velocities. Each data point was assigned to a flow regime, based on the visual observations made using the high-speed imaging system. A total of 244 data points were collected and Table 6.1 shows the flow regime breakdown of these points. The results are plotted on the three flow regime maps, and the accuracy of each map in predicting transition boundaries discussed.

Table 6.1 Number of Data Points For Each Flow Regime

Flow Regime	No. Data Points	Flow Regime	No. Data Points
P	35	SBZ	13
W	9	S-D	12
S	34	P-S	34
D	1	P-ST-W	12
A	24	W-A	2
M	11	W-BTS	2
BTS	38	W-S	3
FS	13	SBZ-BTS	1

6.1 Mandhane et. al. (1974) Flow Regime Map

The first map examined is the Mandhane et. al. (1974) flow regime map, which is the most recommended empirical map (Hetsroni, 1982). Figure 6.1 shows the present data on the Mandhane et. al. (1974) map. For simplicity, three of the slug flow regimes

78
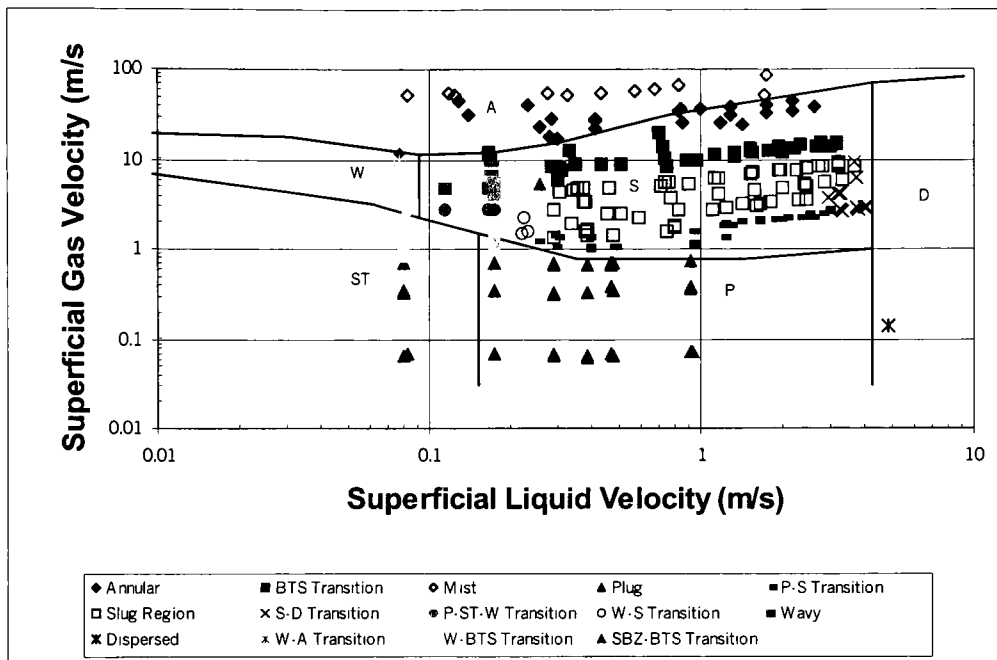
Figure 6.1: Mandhane et. al. (1974) Flow Regime Map Results
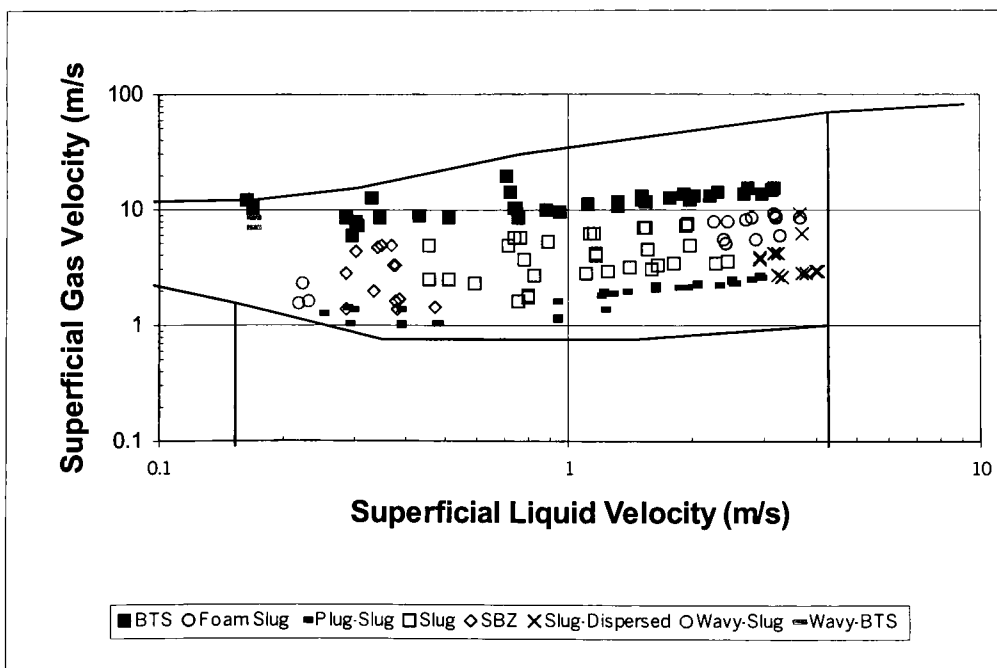
Figure 6.2: Details of Slug Region on Mandhane et. al. (1974) Map

(SBZ, S, FS) have been combined a single 'Slug Region', however details of the slug region are shown in Figure 6.2. No transition between the annular and mist flow regimes is suggested by Mandhane et. al. (1974), preventing evaluation of the map in predicting the mist region. Only one point was taken in the dispersed flow regime, as this region is very difficult to reach using the present experimental facility set-up.

The slug flow regime is well predicted by the flow map, with all data points falling within the suggested 'slug area' of the map. Transition between slug flow and annular flow is represented by the blow through slug data, which occurs at air superficial velocities in the range of 6 – 20 m/s. This transition is clearly over-predicted by the map, which suggests the transition occurs at higher air superficial velocities of 11 – 70 m/s (with increasing oil velocity). The map also poorly predicts the plug to slug transition, with the current data indicating the transition occurs at higher superficial gas velocities (1.2-2.5 m/s) over the range of liquid superficial velocities (0.25-4.3 m/s) than suggested by the map. All of the other transition boundaries are found to have transition data points on both sides of the predicted line. This does not necessarily indicate a problem with the transition boundary, as transition between flow regimes occurs more gradually than suggested by most flow regime maps (Barnea et. al., 1979).

In an attempt to correct for the apparent inaccuracy in predicting the transition boundaries, the suggested physical property correction factors were applied and the results are shown in Figure 6.3. Results of this correction are varied. The transition boundary for dispersed flow shifted to the right to an oil superficial velocity of 10 m/s, which results in an inability of the map to predict the slug to dispersed transition. The air

superficial velocities of the slug to annular transition boundary shifted up by 5-15 m/s but the oil superficial velocities remained relatively unchanged. This leads to a small decrease in the accuracy of the map to predict for this transition. All other boundaries showed some improvement in prediction. While the suggested air superficial velocities for both the wavy to slug and the stratified to plug transitions appear to be off by a factor of 3, the new oil superficial velocities are more representitive of the transitions. Finally the plug to slug transition shows the most improvement, correctly predicting the transition between oil superficial velocities of 0.25 – 1 m/s. In the upper range of oil superficial velocities for this transition, the air superficial velocities are still under-predicted by a factor of 4. A possible reason for the presence of inaccuracies in the corrected map could be the transition boundary corrections suggested by Mandhane et. al. (1974). The general equation used has the form:

$$j_i' = Mj_i \qquad\qquad 6.1$$

where M represents the correction applied. Each transitional boundary is based on a set of co-ordinates (see Table 2.1) and one of several alternative correction factor equations. An improved correction might be found by applying the Mandhane et. al. (1974) physical property factors to the transitional boundary co-ordinates in the form suggested by Glovier and Aziz (1972).

$$j_g' = X' j_g \qquad\qquad 6.2$$

$$j_l' = Y' j_l \qquad\qquad 6.3$$

$$X' = (\frac{\rho_g}{0.0808})^{0.2} (\frac{72.4\rho_l}{62.4\sigma})^{0.25} (\frac{\mu_g}{0.018})^{0.2} \qquad\qquad 6.4$$

$$Y' = (\frac{\mu_l}{1.0})^{0.2} (\frac{72.4\rho_l}{62.4\sigma})^{0.25} \qquad\qquad 6.5$$

Figure 6.4 shows that the result of using this form of correction is again varied. The plug to slug transition boundary is now over-predicted in the 0.25 – 1 m/s oil superficial velocity range; however, below 0.25 m/s it shows improvement in predicting the stratified to wavy transition. The slug to annular transition boundary has shifted to the left by a factor of 2, having the effect of moving the boundary to lower air superficial velocities at higher oil superficial velocities. A further shift of the air superficial velocities by a factor of 2 and the corresponding oil superficial velocities by a factor of 1.2 would have the effect of predicting the transition accurately. Both the slug to dispersed and the stratified to slug transition boundaries are shifted to the left by approximately 5 m/s and are thus less accurately predicted by the proposed corrections. Interestingly, the wavy to slug flow transition is at relatively the same oil superficial velocity as in Figure 6.3; however, the air superficial velocities are now in the expected range of 3-14 m/s.

Overall, the two suggested methods of correction for physical properties improve the prediction of the map only marginally. The accuracy gained in adjusting one transition line is lost in adjusting another. For example, in Figure 6.3 the plug to slug transition correction now accurately predicts the 0.25 – 1 m/s range. Unfortunately, the slug to dispersed transition correction accuracy observed in the original map (Figure 6.2) is lost. A similar argument can be made for the corrections shown in Figure 6.4.
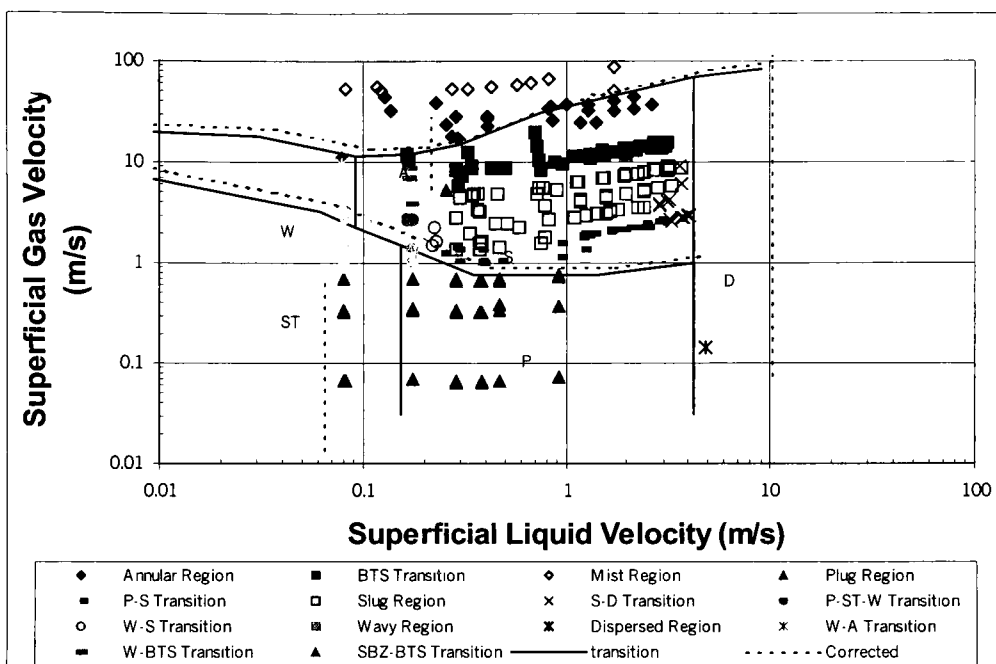
Figure 6.3: Mandhane et. al. (1974) Property Corrections for Map
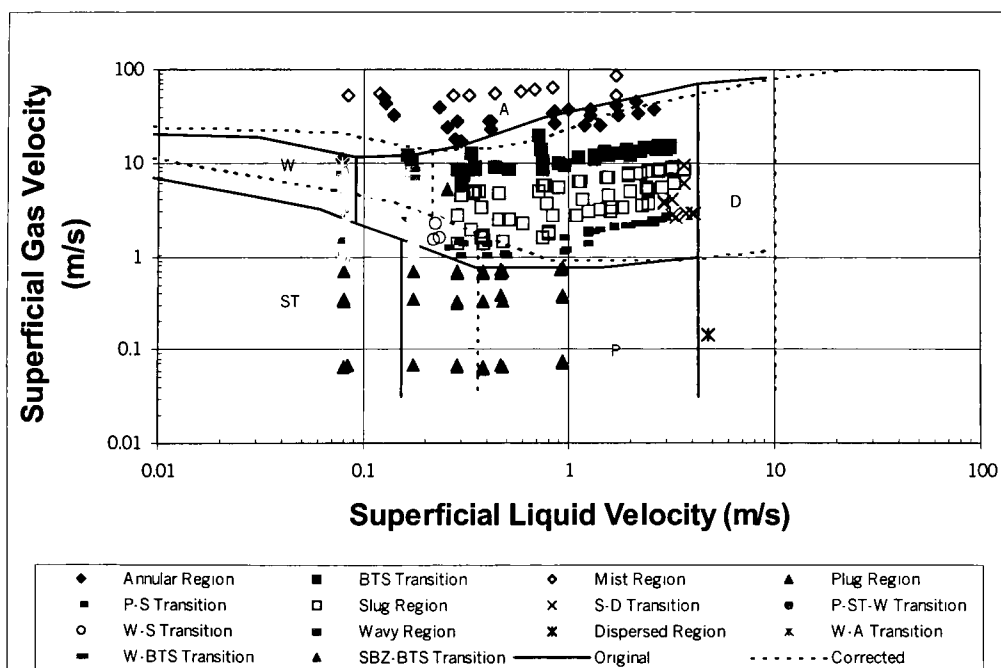
Figure 6.4: Alternative Property Correction for Mandhane et. al. (1974) Map

It is apparent that more study is required on the form the physical property factors should take in order to obtain more accurate transition boundaries. As a first recommendation, a combination of the two correction factor forms is suggested (Table 6.2). The resulting flow map is shown in Figure 6.5. While more corrections are required, this map serves as a relatively accurate improvement upon the original Mandhane et. al. (1974) flow regime map.

Table 6.2: Suggested Transition Boundary Correction Factors

Transition Boundary	Physical Property Correction Equation
Stratified to Plug	$j_i' = Y^{r-1} j_i$
Wave to Slug	$j_l' = Y' j_l$
	$j_g' = 0.5 X' j_g$
Plug and Slug to Dispersed	No Change
Stratified and Plug to Wave and Slug	$j_i' = X j_i$
Wave and Slug to Annular-Mist	$j_l' = 1.2 Y' j_l$
	$j_g' = 0.4 X' j_g$
Dispersed to Annular-Mist	$j_l' = Y' j_l$
	$j_g' = 0.4 X' j_g$

6.2 Taitel and Dukler (1976) Flow Regime Map

The Taitel and Dukler (1976) flow regime map is evaluated using the current data in this section. In order to represent all of the transition boundaries with one set of plotting parameters, the map is presented using superficial velocities (Figure 6.6). The transition boundaries between plug and slug flow, and annular and mist flow, were not developed by Taitel and Dukler and therefore cannot be evaluated. As with the Mandhane et. al. (1974) map, three of the slug flow regimes have been combined and classified as 'slug region' for simplicity.
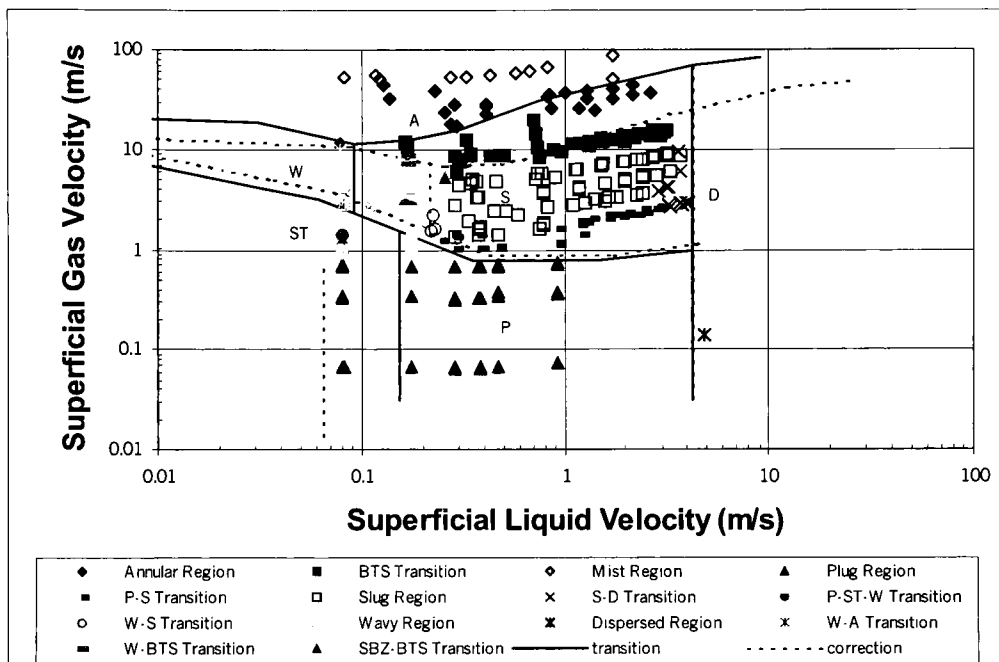
Figure 6.5: Suggested Correction for Mandhane et. al. (1974) Map
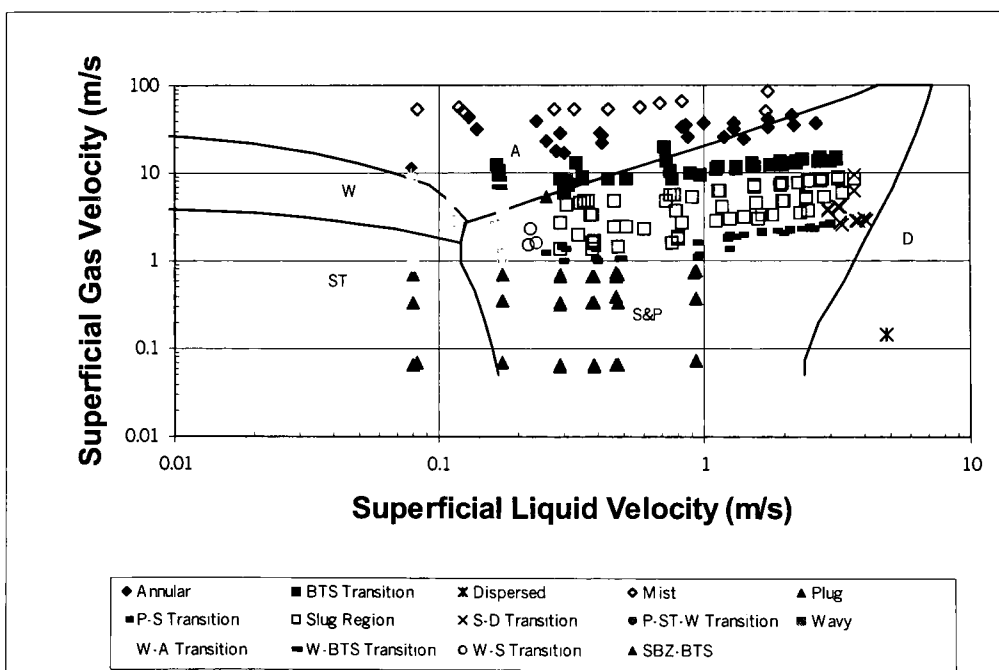
Figure 6.6: Taitel and Dukler (1976) Flow Regime Map Results

The transition between slug and annular flow, as represented by the blow through slug flow regime, is accurately predicted at oil velocities in the range of 0.3 – 0.7 m/s. At velocities greater than 0.7 m/s, the present data indicates transition occurs at lower gas velocities than those predicted by the map. Transition between wavy and annular flow regimes also appears to be well predicted at oil velocities below 0.1 m/s. All the other transitional boundaries require adjustment to better predict the transition between flow regimes. For example, the stratified to plug transition is predicted to occur at oil superficial velocities of 0.12 – 0.16 m/s, but plug flow was observed at an oil superficial velocity of 0.08 m/s. Similarly, the slug to dispersed flow regime transition range for the oil superficial velocity is over-predicted by 1.5 m/s.

Like most flow regime maps, the Taitel and Dukler (1976) map is based on the properties of air and water. The transitional boundaries in Figure 6.6 are determined using the properties of air and water, which allows direct comparison between the different flow maps presented in this chapter. In order to correct the flow map to reflect the properties of oil instead of water, the original transitional boundaries must be recalculated. This is a very tedious process due to the fact that several of the plotting parameter equations include both the air and oil superficial velocities, requiring an iterative solution. In addition, Taitel and Dukler (1976) use the phase velocities and hydraulic diameter to determine Reynolds number, and therefore whether the friction factor is laminar or turbulent. Without knowing these values, transformation of the original map to superficial velocities for air-oil two-phase flow will result in large errors.

Taitel and Dukler (1976) present their map converted into superficial velocities for crude oil-natural gas two-phase horizontal flow at 38°C, 68 atm in a 5.0 cm pipe. While this type of flow has different physical properties compared to the air-oil two-phase flow presented here, the shift of the transition boundaries actually improves the prediction for the blow through slug transition regime (Figure 6.7). The intermittent to annular transition (Curve B) is shifted downwards, with the superficial gas velocity range changing from 3.5-144 m/s to 2.6-50 m/s. Unfortunately, the new positions for the other transition boundaries decrease the accuracy of the map. Clearly the ability of the map to predict flow regime transitions can be improved by correcting for the correct physical properties, but this process requires more property data than was collected for this thesis. The Taitel and Dukler map with transitional boundaries based on air and water properties is therefore the better choice for predicting flow regimes in this case.

6.3 Spedding and Nguyen (1980) Flow Regime Map

The final map examined is the dimensionless plotting parameter map of Spedding and Nguyen (1980). In order to compare their flow map to other maps, Spedding and Nguyen (1980) used air and water two-phase flow results to obtain the transition boundaries. As discussed in chapter two, the definitions for the flow regions are different than those of the previous two maps. For example, the blow through slug flow regime is represented as a flow region and not a transitional boundary. The same is true for the wavy to slug flow transition. Figure 6.8 shows the present results using the dimensionless parameters of Spedding and Nguyen. It can be seen that the map predicts
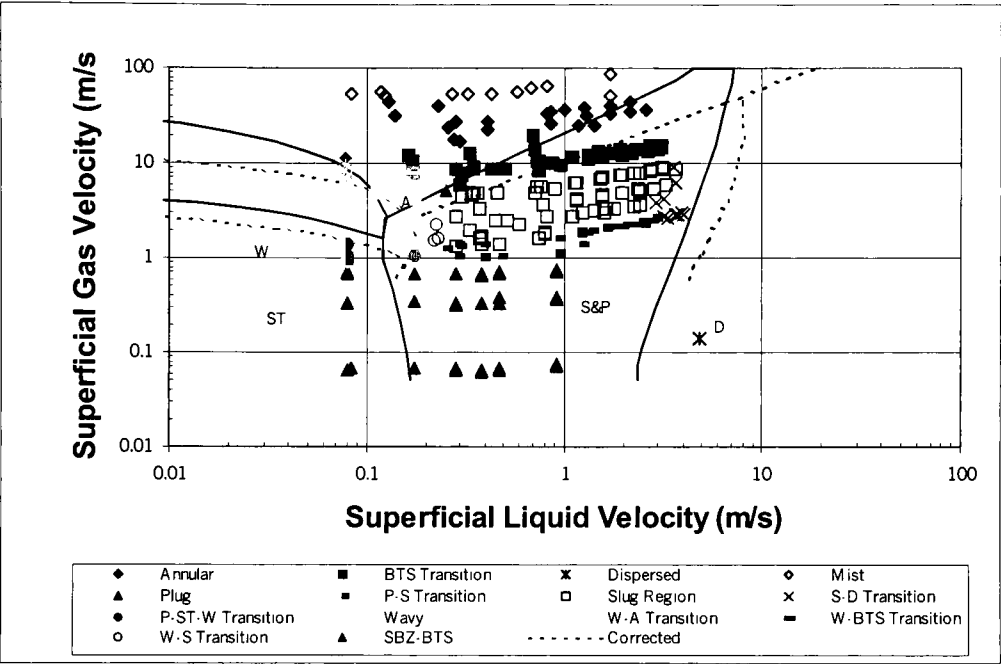
Figure 6.7: Taitel and Dukler (1976) Map Physical Property Effect
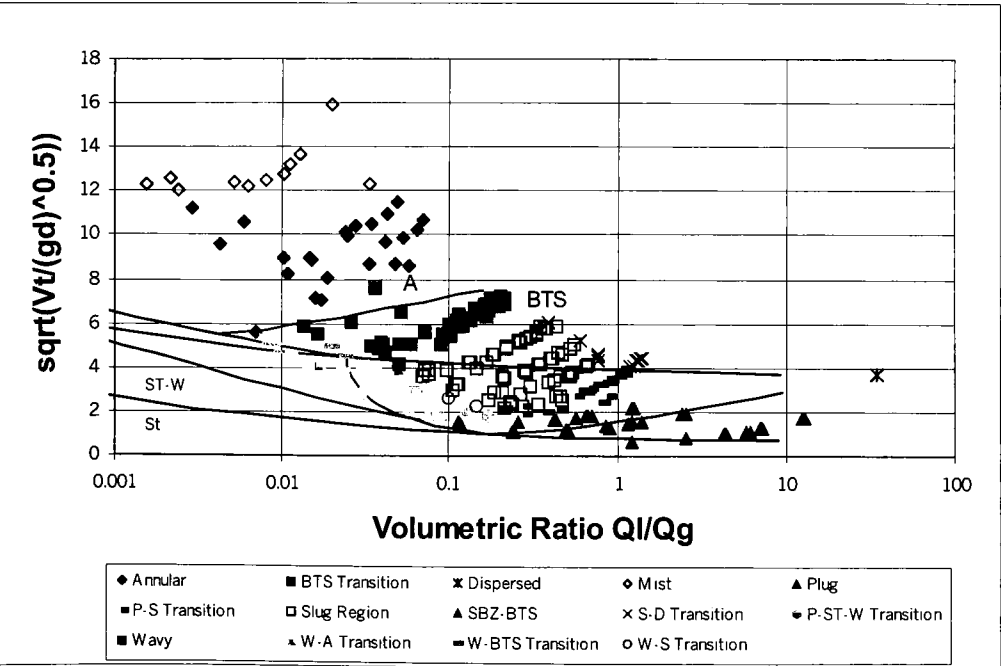
Figure 6.8: Spedding and Nguyen (1980) Flow Regime Map Results

the blow through slug and annular flow regime data with a great deal of accuracy. Unfortunately, the slug region is not well predicted by the flow regime map, which decreases the usefulness of the map when working with oil, as slug flow is often encountered.

Unlike the other two flow maps presented here, the dimensionless numbers used for the plotting parameters rely on the physical properties of the two phases indirectly. Spedding and Nguyen (1980) suggest that transitional boundary prediction errors are more likely to result from differences in test facilities than from use of different two-phase systems. They do caution, however, that the use of alternative two-phase systems may lead to a decrease in accuracy for their map (Spedding and Nguyen, 1980). This is due to the fact that some flow regimes appear only for certain gas-liquid combinations. Due to the poor results of adjusting the Mandhane et. al. (1974) and Taitel and Dukler (1976) flow regime maps to account for oil properties, no attempt is made to adjust Spedding and Nguyen's map.

6.4 Comparison of Flow Regime Maps

In order to evaluate the overall usefulness of the three flow regime maps presented, the maps were compared against one another. The ability of each map to predict correctly the flow regimes was calculated using the method suggested by Mandhane et. al. (1974). The number of correctly predicted points in an individual flow regime is divided by the number of total observed points in the flow regime and converted to a percentage. The total number of correctly predicted points and the average

accuracy of the whole map can then be determined. Table 6.3 lists the results of this comparison. Several flow regimes have a limited number of collected data points, and are therefore included in the table but not considered in the comparison.

Table 6.3 Comparison Of Flow Regime Maps

Flow Regime	Number of Points	Mandhane Correct	Mandhane % Correct	T&D Correct	T&D % Correct	S&N Correct	S&N % Correct
A	24	13	54.2	16	66.7	23	**95.8**
M	11	11	**100.0**	10	90.9	0	0.0
D	1	1	100.0	1	100.0	0	0.0
S	60	60	**100.0**	60	**100.0**	29	48.3
W	9	3	33.3	3	33.3	4	44.4
P	35	29	**82.9**	29	**82.9**	19	54.3
BTS	38	1	2.6	6	15.8	37	**97.4**
P-S	34	2	0.0	0	0.0	0	0.0
P-ST-W	12	2	16.7	0	0.0	0	0.0
S-D	12	1	8.3	2	16.7	0	0.0
W-BTS	2	0	0.0	0	0.0	2	100.0
W-S	3	0	0.0	0	0.0	0	0.0
W-A	2	0	0.0	2	100.0	2	100.0
SBZ-BTS	1	0	0.0	1	100.0	0	0.0
Total	244	123	50.4	130	**53.3**	116	47.5

The Mandhane et. al. (1974) and Taitel and Dukler (1976) flow regime maps predict the slug region with 100% accuracy. While Taitel and Dukler (1976) do not define a transition boundary between plug and slug flow, most of the plug points still lie within the defined "intermittent" region. This is clear in Figure 6.9, where the Mandhane et. al.(1974) and Taitel and Dukler (1976) maps have been superimposed.
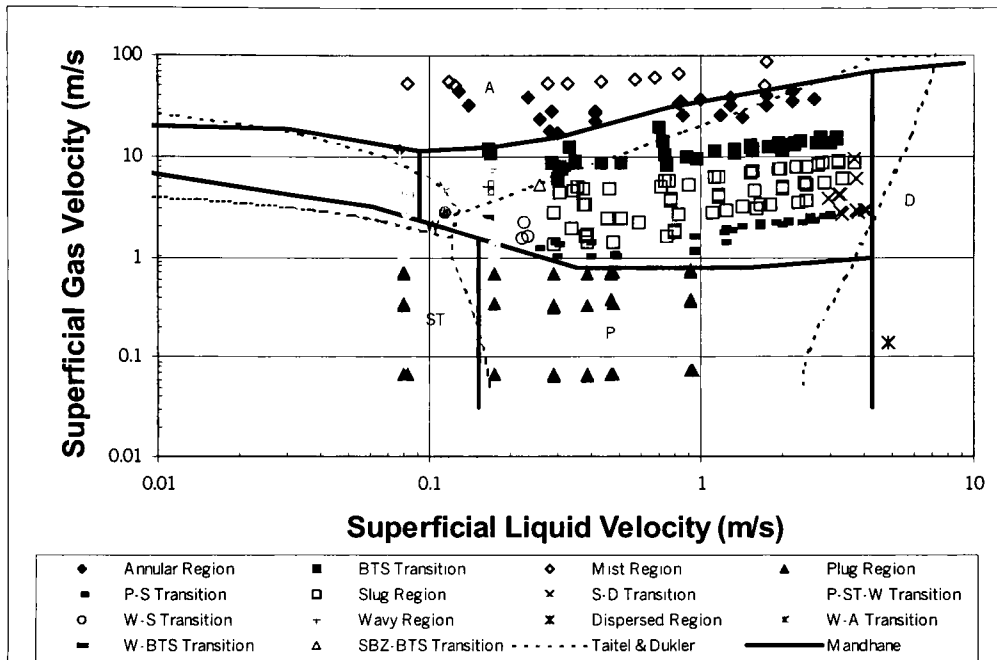
Figure 6.9: Mandhane and Taitel & Dukler Maps Compared

The small improvement in prediction accuracy for A, BTS, and P-S flow data observed in the Taitel and Dukler (1976) map is also shown in this figure. In comparison the Spedding and Nguyen (1980) flow regime map performs poorly in the slug region but has a high accuracy in predicting the BTS and A flow regimes. Overall the Taitel and Dukler (1976) flow regime map is found to have the highest prediction accuracy at 53%, which can be attributed to the high accuracy in predicting the flow regimes with the most collected data points. Further study of the wavy and dispersed flow regions might alter the overall accuracy of each map.

Corrections to the Mandhane et. al. (1974) flow regime map (Mandhane2) were suggested in Table 6.2. Applying the same analysis to this map, the improvement in accuracy is clear (Table 6.4).

Table 6.4 Comparison Of Mandhane et. al. (1974) Maps

Flow Regime	Number of Points	Mandhane Correct	Mandhane % Correct	Mandhane2 Correct	Mandhane2 % Correct
A	24	13	54.2	23	95.8
M	11	11	100.0	11	100.0
D	1	1	100.0	1	100.0
S	60	60	100.0	60	100.0
W	9	3	33.3	9	100.0
P	35	29	82.9	35	100.0
BTS	38	1	2.6	23	60.5
P-S	34	0	0.0	10	29.4
P-ST-W	12	2	16.7	3	25.0
S-D	12	1	8.3	1	8.3
W-BTS	2	0	0.0	2	100.0
W-S	3	0	0.0	3	100.0
W-A	2	0	0.0	0	0.0
SBZ-BTS	1	0	0.0	1	100.0
Total	244	121	49.6	182	**74.6**

Therefore the Taitel and Dukler (1976) map is recommended as the best predictive flow regime map without any correction factors applied, and the corrected Mandhane et. al. (1974) as the best overall map.

6.5 Effect of Mixer Design

As discussed in Chapter Four, two different mixer designs were used in the test facility. Forty data points were collected with the original mixer; however, concern over the effectiveness of the mixer resulted in a switch to the current design. All data presented in the flow regime map and pressure drop prediction model results were collected using the current mixer design. Twenty data points that exactly mimic twenty data points from the original mixer were taken in an effort to compare the two mixer designs. Air and oil flow rates were reproduced, and the inlet pressure and pressure drop

recorded. Of the twenty new points, only three were found to have different flow

regimes than the original (Table 6.5).

Table 6.5: Mixer Design Flow Regime Comparison

Point	Old Mixer	New Mixer	Point	Old Mixer	New Mixer
1	BTS	BTS	11	**S-D**	**BTS**
2	S	S	12	S	S
3	BTS	BTS	13	S	S
4	S	S	14	S	S
5	BTS	BTS	15	**FS**	**S**
6	S	S	16	**BTS**	**S**
7	BTS	BTS	17	BTS	BTS
8	S	S	18	**FS**	**S**
9	BTS	BTS	19	BTS	BTS
10	S-D	S-D	20	A	A

Of these three points (11,15,18), two are still in the slug flow region and are simply

different types of slug flows. Only point eleven had distinctly different flow regimes for

the two mixers. The old mixer produced a slug to dispersed transitional flow

characterized by very short, aerated slugs interspersed with tiny bubbles flowing down
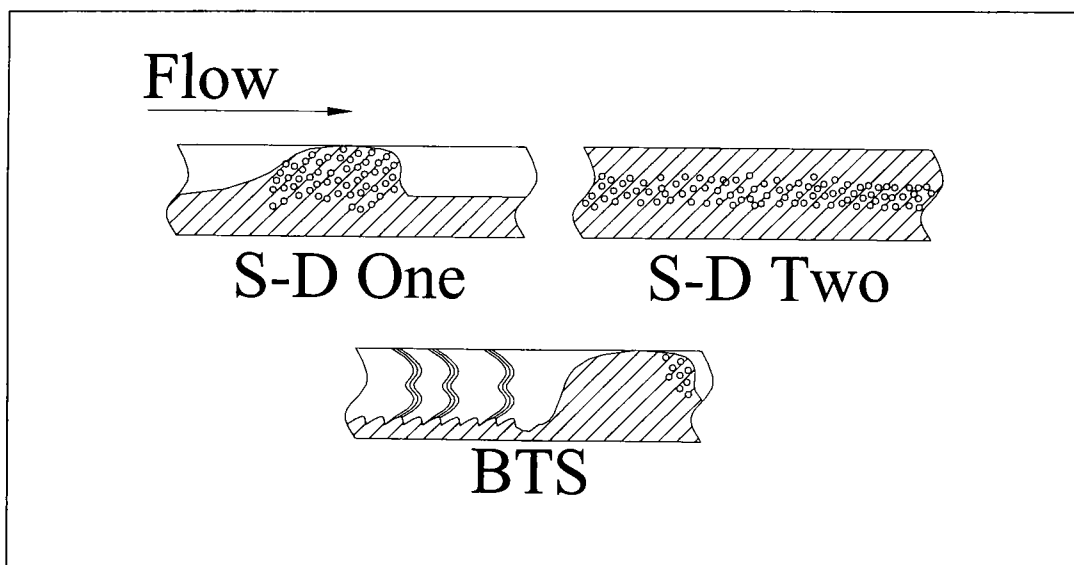
Figure 6.10: a) [Top] Slug to Dispersed Transition Regime
b) [Bottom] Blow Through Slug Transition Regime

the center of the liquid filled tube (Figure 6.10a). The new mixer produced classic blow through slug flow as depicted in Figure 6.10b. The difference is likely due to ineffective mixing caused by the original design, which at the air and oil flow rates for point eleven, would have retarded airflow at times.

The main difference between the two mixer designs was found in the recorded values for inlet pressure and pressure drop. Figure 6.11 shows the inlet pressure comparison for the two mixers. The original mixer consistently produced higher inlet pressures than the current mixer design. Pressure spikes upstream of the test section caused by ineffective mixing of the two phases could account for this difference. The lower pressure drops recorded for the original mixer (Figure 6.12) also illustrate the effect of mixer selection on the characteristics of the flow. Overall, the elimination of the upstream pressure spikes and the improvement in phase mixing by the current mixer design supports the decision to switch to the design.
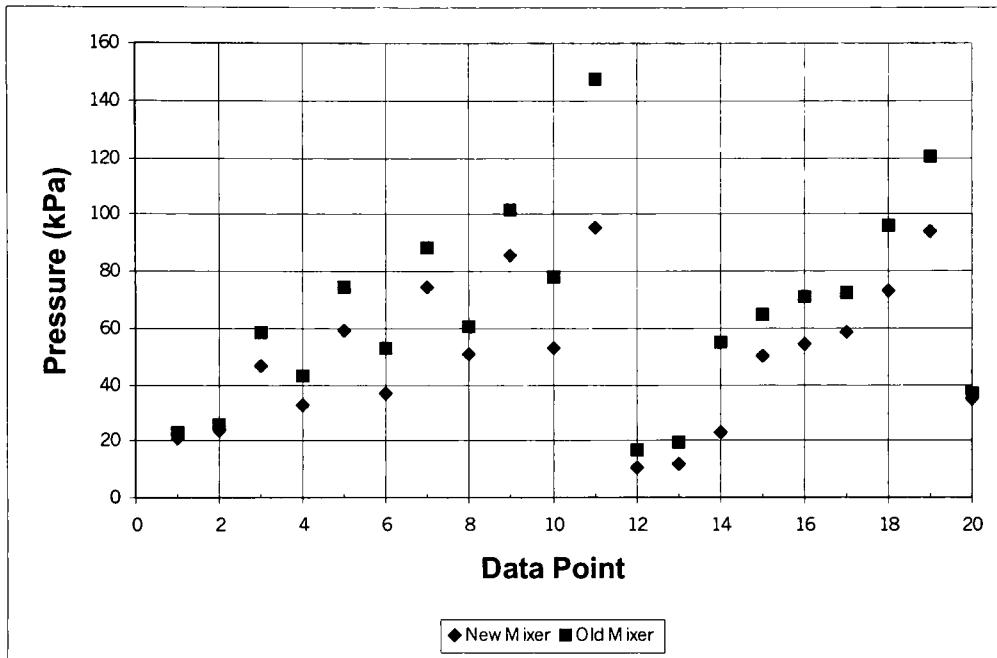
Figure 6.11: Inlet Pressure Comparison for Mixers
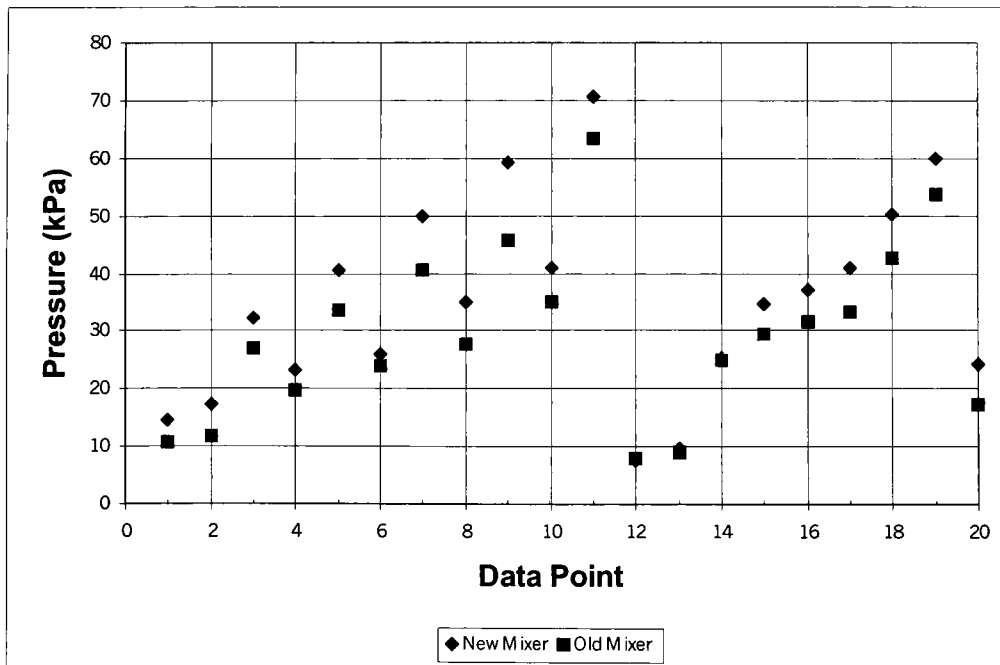
Figure 6.12: Pressure Drop Comparison for Mixers

Chapter Seven: Pressure Drop Results

Four frictional pressure drop models (Homogeneous, Martinelli, Chisholm, and Olujic) were compared against the measured pressure drop data over the entire range of flow regimes. Results for each model are presented and possible corrections to the models are discussed in this section. The overall performance of each model is presented, and the models compared using an error analysis. Finally, a pressure drop model (Chang and Tremblay) developed specifically for the mist flow regime is examined.

7.1 Homogeneous Model

The homogeneous model assumes that the two phases form a mixture with one set of physical properties. This assumption precludes the model from accurately predicting pressure drop in flow regimes that do not have a very low or very high void fraction (high oil or high air content). While the overall results for the homogenous model were found to under-predict the pressure drop by an average of 41% (Figure 7.1), the maximum under-prediction of 83% occurred in the wavy-slug region. Since the pressure drop in this flow regime is largely influenced by the passing slugs, oil properties would take precedence over the air properties. Using the homogenous model, which gives equal weight to both mass flow rates, cannot account for this influence. Figure 7.2 shows those flow regimes where the model performs the best. Mist flow and annular flow are the best
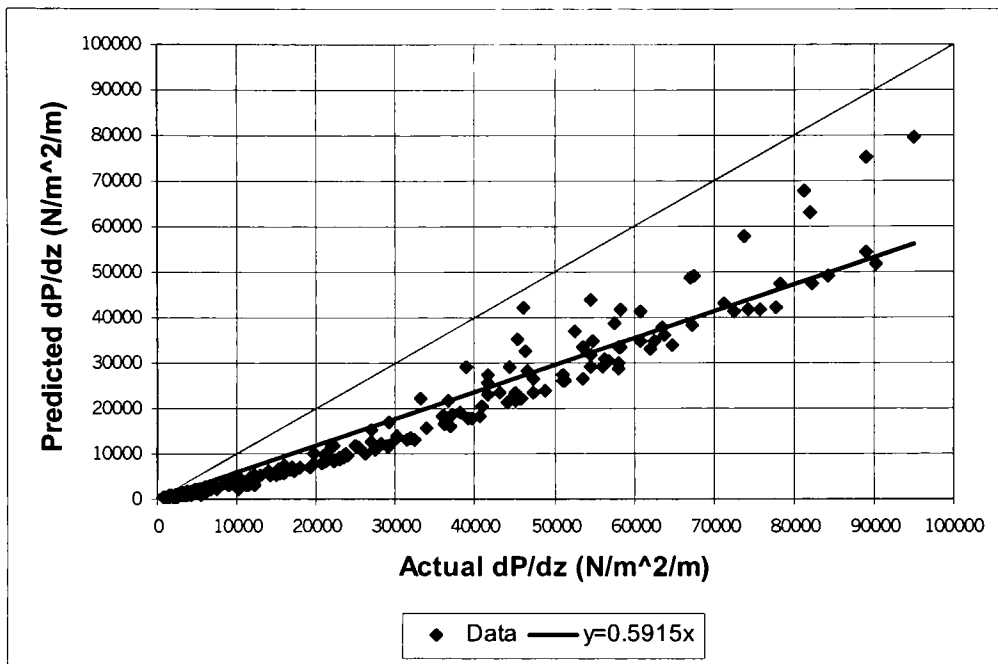
Figure 7.1: Homogeneous Model Pressure Drop Results
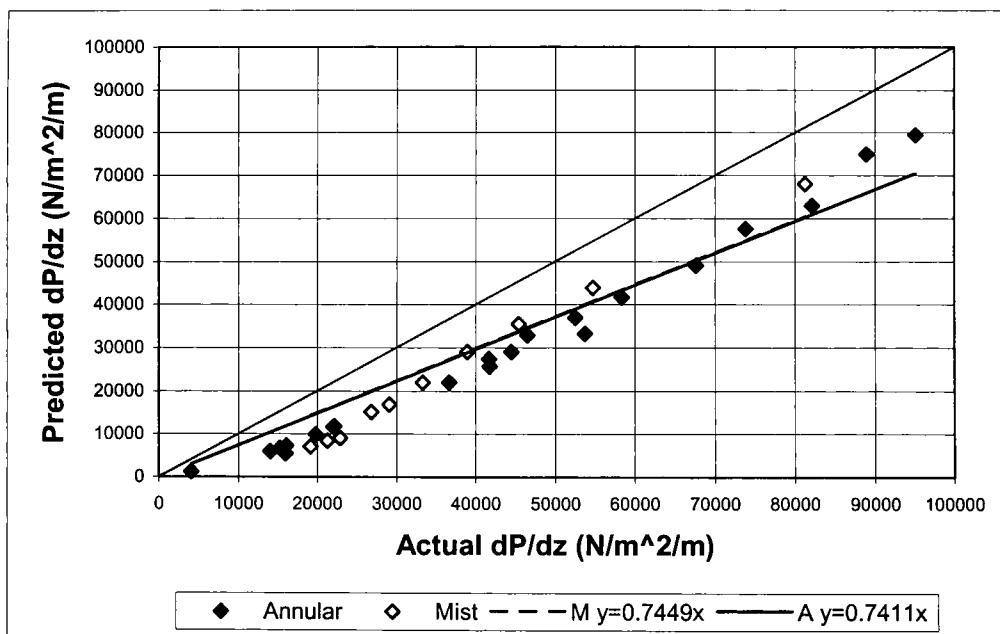
Figure 7.2: Homogenous Model Predictions For Specific Flow Regimes

predicted flow regimes with an average under-prediction of about 26%. Dispersed flow, though well predicted because it is mostly oil, is not included due to insufficient data collection.

The homogeneous model is relatively simple in terms of calculation and therefore is often used as a starting point for more complex model development. In this case, the homogeneous model had a wide spread of data, making it difficult to apply some form of correction factor. Generally, correction of the model occurs in the calculation of the friction factor, however laminar or turbulent flow was already taken into account in the results presented. Use of a more complex friction factor is not warranted, as the tube is smooth. Thus no correction is suggested for the homogeneous model at this time.

7.2 Martinelli Model

The Martinelli model was found to consistently under-predict the pressure drop by an average of 47% across all flow regimes (Figure 7.3). The one anomaly is the dispersed flow data point, which is very accurately predicted by the model (2.5%). A maximum under-prediction of 70% occurred in the annular flow regime, which averaged a 56% under-prediction (Figure 7.4). A minimum under-prediction of 18% occurred in the slug-building zone, which averaged a 35% under-prediction (Figure 7.5). Since the Martinelli model has been found to be applicable for flows with a total mass flux less than 100 kg/m^2s, it is not surprising that the slower moving flow regimes (Plug and Wavy regions) are best predicted by this model.
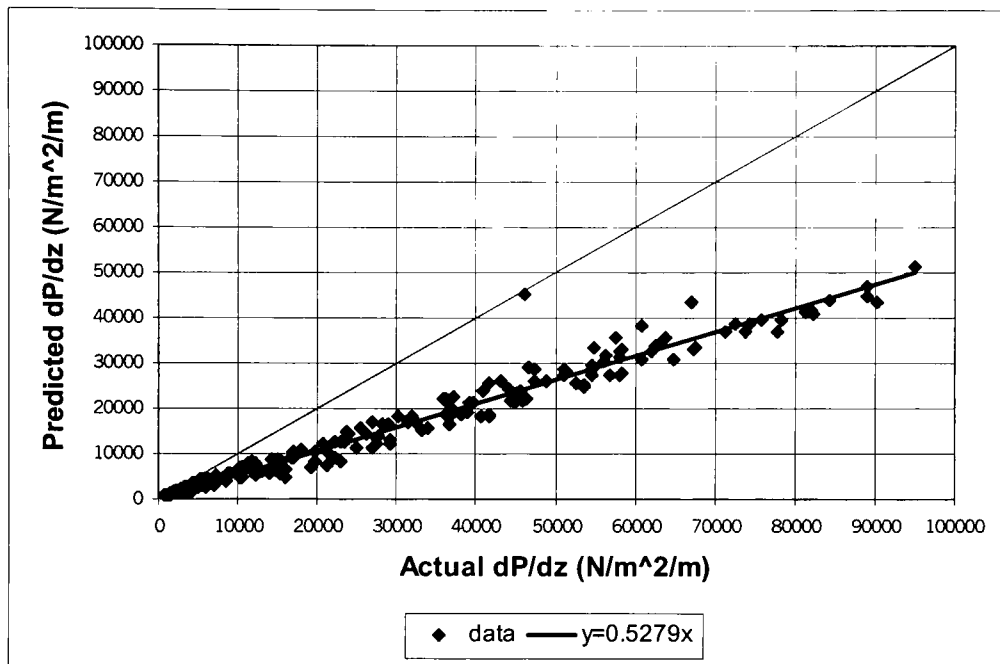
Figure 7.3: Martinelli Model Pressure Drop Results
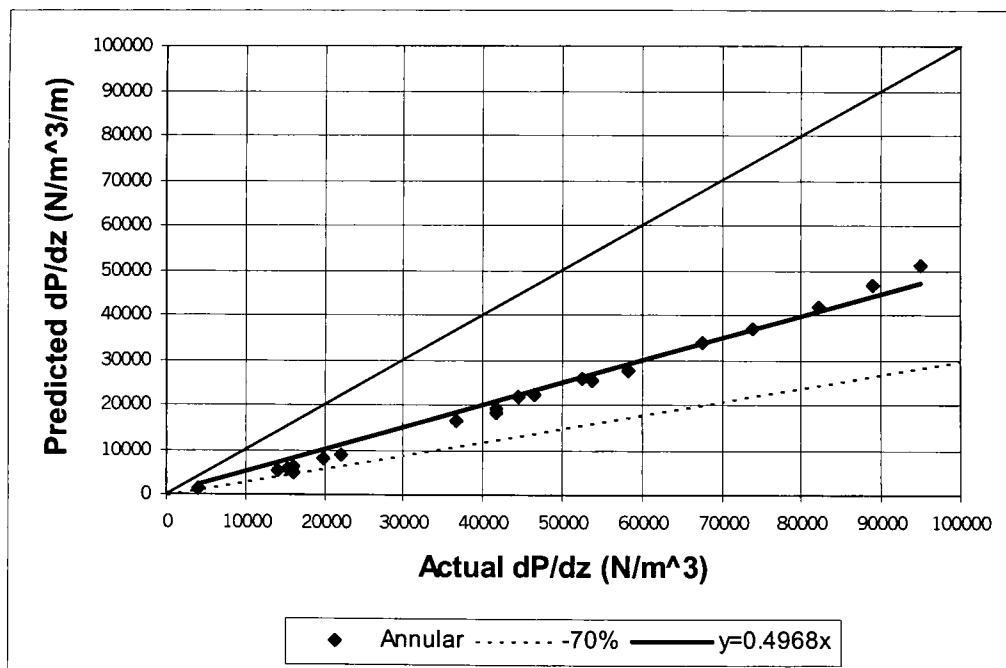
Figure 7.4: Martinelli Model – Annular Flow Regime
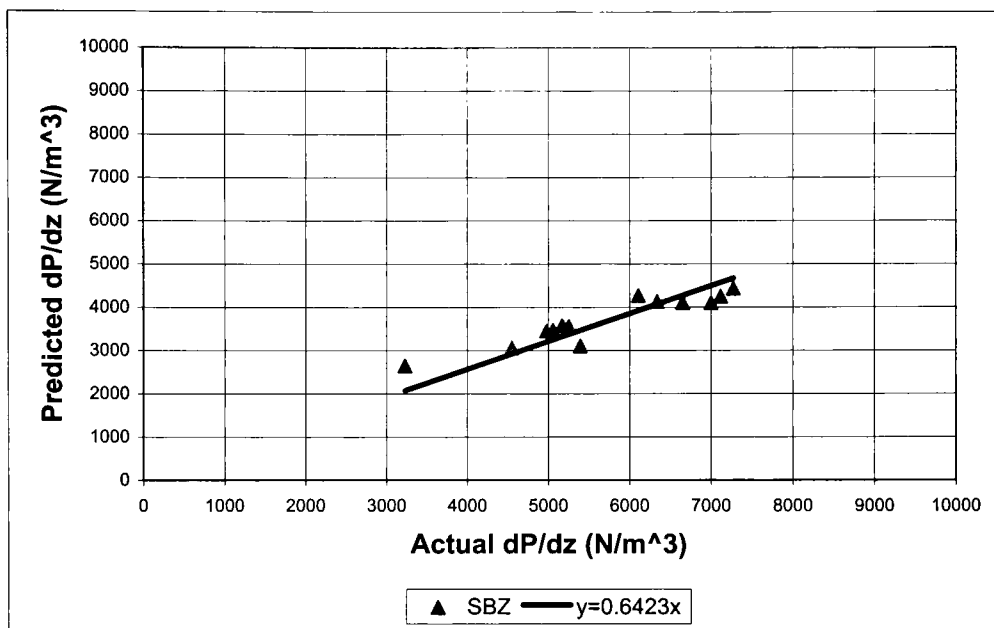
Figure 7.5: Martinelli Model – Slug Building Zone Flow Regime
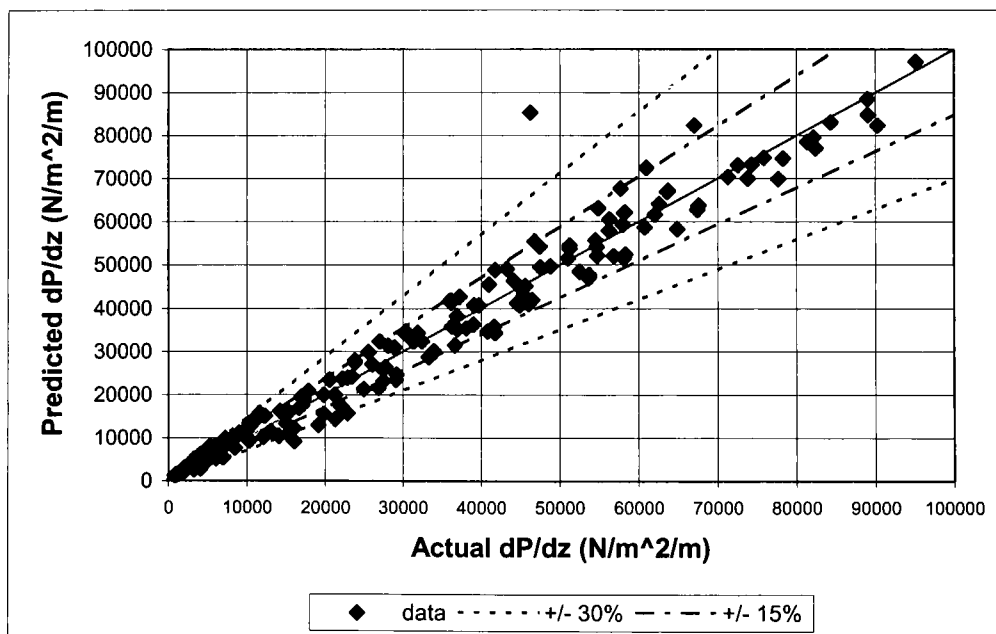
Figure 7.6: Corrected Martinelli Model Pressure Drop Results

The relatively small scatter in the data from the Martinelli model allows for a simple single correction factor to be applied for all flow regimes. Taking the inverse of the slope of the trendline, the model is multiplied by a factor of 1.9, resulting in the data distribution shown in Figure 7.6. With the exception of the dispersed data point, the corrected model predicts the frictional pressure drop within ±30% of the measured pressure drop. The accuracy improves to ±15% for pressure drops above 15000 N/m^2/m.

7.3 Chisholm Model

The Chisholm model (Figure 7.7) predicted the pressure drop with an average of 43% under-prediction; however, several of the flow regimes were predicted with a much higher accuracy (<30%). The twelve data points separated from the general trendline represent two annular and ten mist flow regime points. Figure 7.8 shows the annular and mist flow regimes in detail. The annular flow regime data shows an overall under-prediction trend of 43%; however, the mist flow regime is much less consistent. The flow regimes predicted with high accuracy include plug, slug, slug building zone and the slug to plug transition. Figures 7.9 and 7.10 show the four regimes and the trendlines, with the slug building zone flow regime having almost no deviation from the measured values. Three other transition regimes (W-S, W-BTS, SBZ-BTS) were also very well predicted (<20% deviation); however, there is insufficient data from which to draw conclusions.

Unlike the Martinelli frictional pressure drop model, the Chisholm model does not closely follow one trendline, making a simple correction to the model difficult.
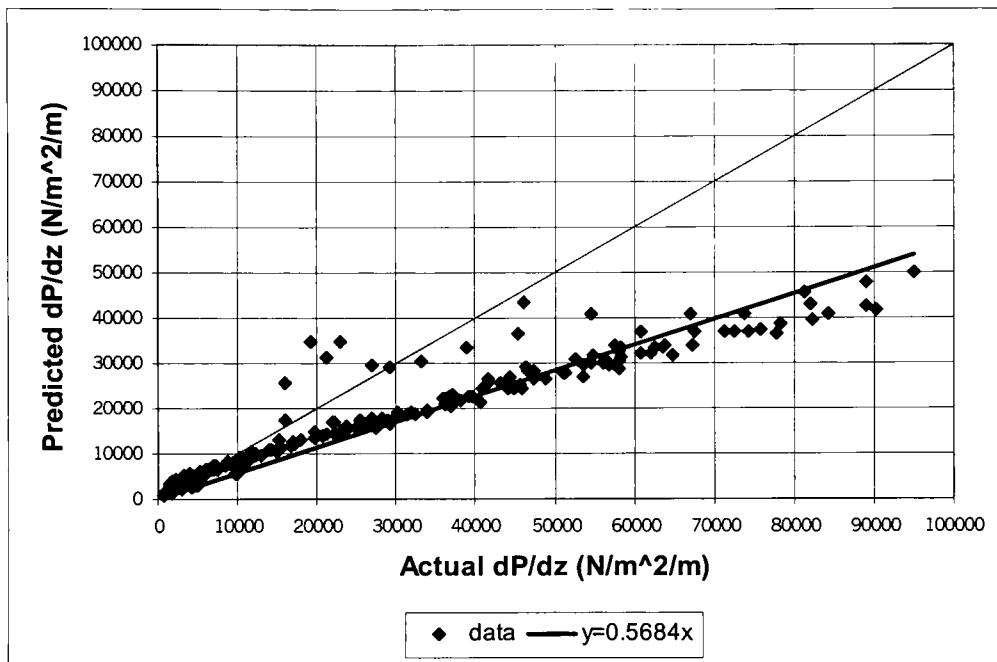
Figure 7.7: Chisholm Model Pressure Drop Results
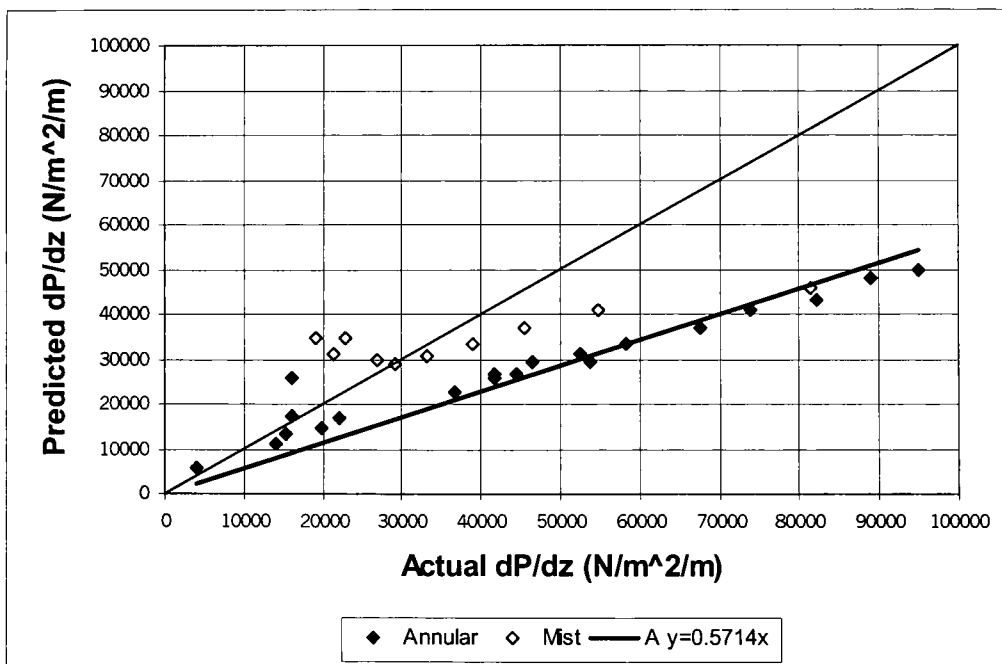
Figure 7.8: Chisholm Model Results For Specific Flow Regimes (1)
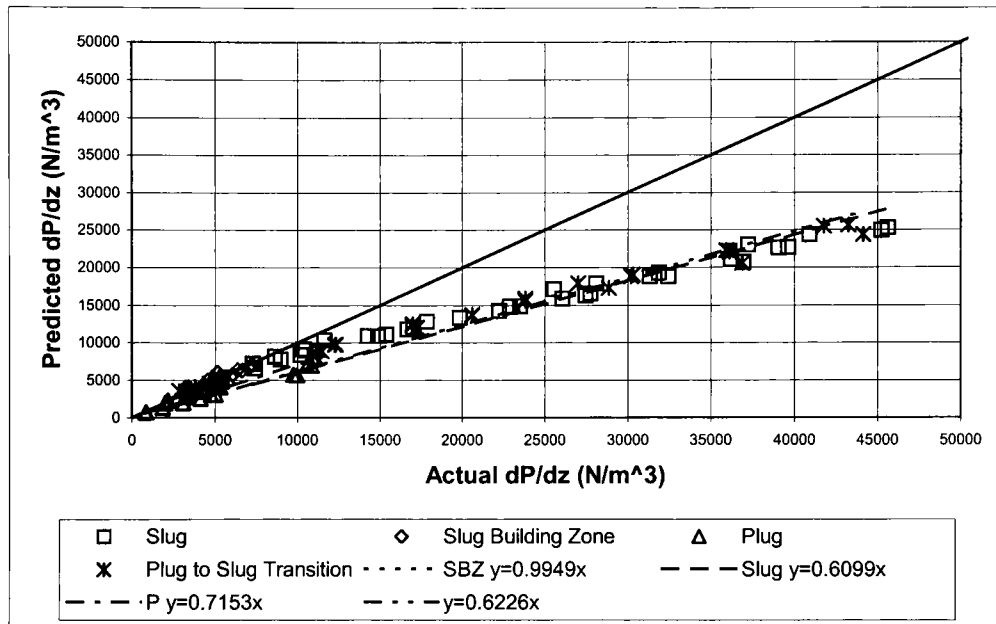
Figure 7.9: Chisholm Model Results For Specific Flow Regimes (2)
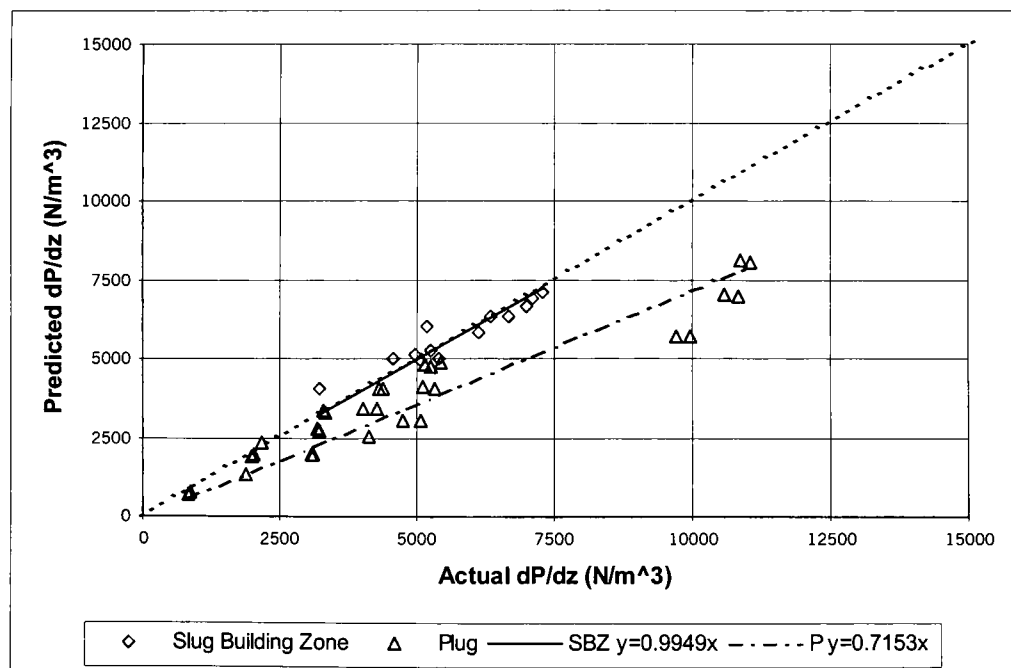
Figure 7.10: Chisholm Model Results For Specific Flow Regimes (3)

The relatively accurate prediction (within 35%) of many of the flow regimes also indicates correction of the model may not be necessary. This model may be useful as a first step in developing a new model that predicts pressure drop based on flow regime. Section 7.5 will discuss this in more detail.

7.4 Olujic Model

Ferguson and Spedding (1995) examined the accuracy of 14 different frictional pressure drop models with respect to individual flow regimes, and found the Olujic model to perform the best over the largest number of identified flow regimes. The Olujic model was therefore investigated using the current air-oil data. Following the guidelines set out by Olujic (1985) for predicting the flow region and selecting the appropriate pressure drop model, it was found that the performance for the current data varies. In the beta region, the model under-predicted the data by an average of 45% (Figure 7.11). This was as a result of applying the suggested friction factors (3.49 and 3.50). Attempting to apply the Olujic (1985) friction factor (equation 3.48) resulted in over-prediction of the pressure drop by a factor of at least 50.

In the alpha region, the model produced good results below an actual pressure drop of 25000 $N/m^2/m$, as shown in Figure 7.12. Above this value, the alpha region model greatly over-predicted the pressure drop (Figure 7.13); with all over-predicted points representing data in the blow through slug, annular, or mist flow regimes. The RMSE for the two models will be discussed in the next section, however, it is clear that using the beta model with the friction factor based on equations 3.49 and 3.50 predicts the pressure drop with an acceptable accuracy. The reason for the alpha model producing

such large over-predictions is not clear. Attempts to correct the model only decreased the accuracy of those flow regimes already acceptably predicted by the model. It was also found that some flow regimes contained points falling in both the alpha and beta regions, suggesting that the model was not correctly identifying the specific flow regimes. Therefore, it is suggested that the criteria used to select which region model is applied is not sufficiently separating the current data by flow regime. The Olujic model is useful, however, for an example of how to develop a pressure drop model based on flow regime. This will be discussed further in the next section.
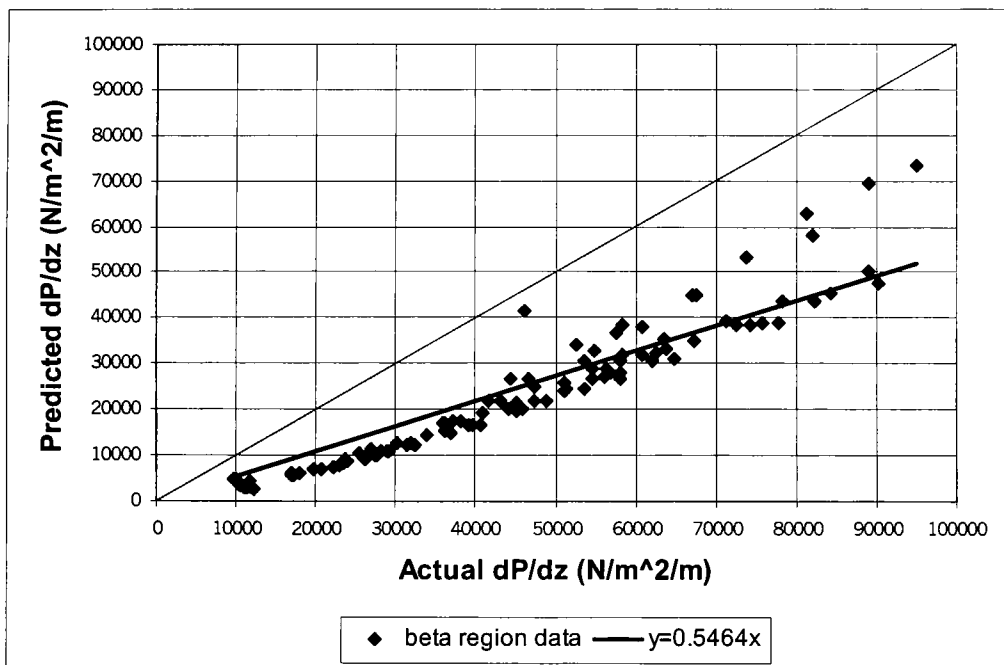
Figure 7.11: Corrected Olujic Model – Beta Region Pressure Drop Results
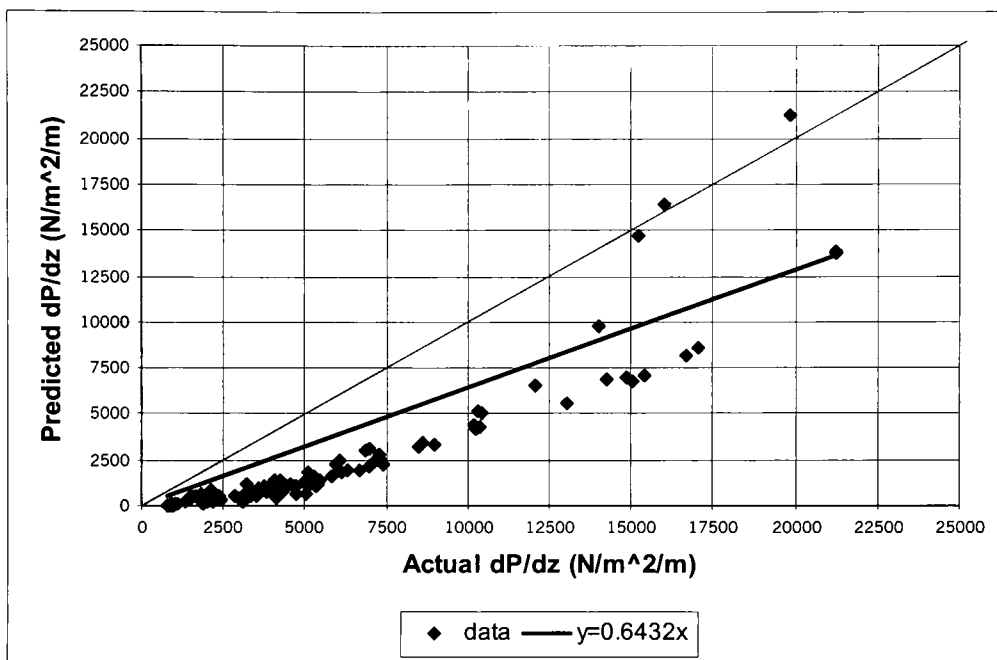
Figure 7.12: Olujic Model – Alpha Region Pressure Drop Results (1)
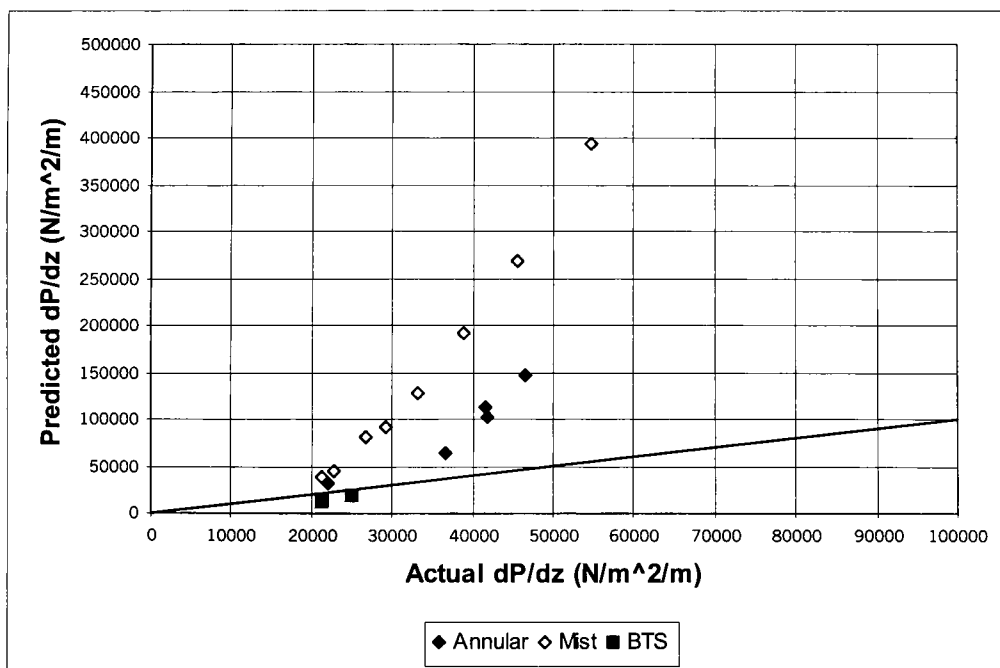
Figure 7.13: Olujic Model – Alpha Region Pressure Drop Results (2)

7.5 Model Error Analysis and Comparison

In order to determine the most accurate frictional pressure drop model, the root mean square error of each model was computed and compared against the other models. A root mean square error (RMSE) is computed as follows:

$$e_i = 100 \left[\frac{\left(\left(\frac{dP}{dz} \right)_{act} - \left(\frac{dP}{dz} \right)_{pred} \right)}{\left(\frac{dP}{dz} \right)_{act}} \right]$$ 7.1

$$rmse = \left[\frac{\sum_i e_i^2}{n} \right]^{0.5}$$ 7.2

Table 7.1: Pressure Drop Model Error Analysis Comparison

Flow Regime	R.M.S.E % Homog.	R.M.S.E % Chisholm	R.M.S.E % Martinelli	R.M.S.E % Olujic
A	42	38	56	78
BTS	52	40	52	53
M	42	39	57	311
FS	44	45	44	49
P	65	26	27	84
P-S	64	29	36	67
P-ST-W	74	49	31	87
S	60	33	43	59
SBZ	70	9	35	72
S-D	43	45	43	47
W	59	76	35	72
W-A	60	84	49	62
W-BTS	59	19	47	65
W-S	80	8	45	84
SBZ/BTS	59	11	39	69
D	9	6	3	10
Total	55	35	40	79

Table 7.1 compares the results for the four models without any corrections to the models.

For each flow regime, the model that best predicts the pressure drop has been highlighted. The foam slug and slug-dispersed regimes are predicted to the same accuracy by the Homogeneous and Martinelli models, while the plug flow regime is predicted with almost the same accuracy by the Chisholm and Martinelli models. Of the sixteen flow regimes, the Chisholm model most accurately predicts ten. These include the intermittent (plug and slug) flow regimes, as well as the high-speed air flow rate (annular, mist and blow through slug) flow regimes. All regimes associated with high oil flow rates, including foam slug, dispersed flow, and the slug-dispersed transition, are well predicted by the Martinelli model. The Homogeneous model also predicted the foam slug and slug-dispersed transition well.

Table 7.2: Results For Olujic Flow Region Models

Flow Regime	Alpha %R.M.S.E	Beta %R.S.M.E
A	100	33
BTS	53	53
M	327	23
FS	n/a	49
P	87	64
P-S	77	63
P-ST-W	87	n/a
S	56	61
SBZ	72	n/a
S-D	N/a	47
W	72	n/a
W-A	62	n/a
W-BTS	65	n/a
W-S	85	n/a
SBZ/BTS	69	n/a
D	N/a	10

As described in section 7.4.1, the Olujic alpha region model gives large prediction errors for the blow through slug, annular and mist flow regimes. Of these three regimes,

the most affected is the mist flow regime, which has an error of 311%. The errors for the other two regimes are acceptable due to the influence of the beta region model. Table 7.2 provides the breakdown of RSME results for the alpha and beta region models. The criterion used by Olujic for the demarcation of the two regions is not satisfactory, as shown in both the beta and alpha regions (Table 7.2). With the exception of the slug flow regime (56% for alpha, 61% beta), the beta region model more accurately predicts all of the shared regimes. Mist flow regime results for both region models are not acceptable; the beta region represents only one data point and the alpha region shows the large over-prediction. The alpha region model predicts all wavy related flow regimes with lower accuracy (62-85%) than the other models presented in Table 7.1 (8-49%). Overall, the Olujic model does not perform as well as the other three models in Table 7.1, however, the beta region model does produce reasonable results for certain flow regimes (annular, foam slug, and slug-dispersed). Applying the beta region model to all data is suggested.

Table 7.3: Range of Pressure Drop Prediction Errors

Flow Regime	Number Points	Max Value Homog.	Min Value Homog.	Max Value Chisholm	Min Value Chisholm	Max Value Martinelli	Min Value Martinelli
A	21	69	16	61	9	70	46
BTS	35	63	39	54	1	60	36
M	10	63	16	82	0.3	65	49
FS	13	51	27	50	39	48	35
P	35	75	50	46	1	38	18
P-S	30	77	45	45	2	45	19
P-ST-W	12	79	59	95	12	42	23
S	34	77	50	45	1	50	28
SBZ	13	82	58	25	0.04	42	18
S-D	12	49	33	51	39	48	37
W	9	64	53	117	23	41	26
W-A	2	66	54	106	55	57	40
W-BTS	2	60	58	23	14	50	44
W-S	3	83	76	12	1	47	41
SBZ/BTS	1	59	59	11	11	39	39
D	1	9	9	6	6	3	3
	233	83	9	117	0.04	70	3

To more closely examine the prediction accuracy, Table 7.3 presents the minimum and maximum prediction error ranges. The Olujic beta region model is applied to all the current data, and is presented as Olujic2 in Table 7.4. While the Chisholm model was found to most accurately predict ten of the sixteen flow regimes, as shown in Table 7.1, it is clear from Table 7.3 that the Martinelli model has the smallest error deviation. This fact was illustrated in Figure 7.3, which showed the smallest data scatter along one trendline. It is also the reason that a simple correction factor could be applied to the model, as shown in Figure 7.6.

The corrected Martinelli and Olujic model results are shown in Table 7.4, along with the original model results.

Table 7.4: Results For Corrected Martinelli and Olujic Models

Flow Regime	R.M.S.E % Martinelli	R.M.S.E % Martinelli2	R.M.S.E % Olujic	R.M.S.E % Olujic2
A	56	27	78	46
BTS	52	13	53	56
M	57	29	311	46
FS	45	7	49	49
P	27	28	84	68
P-S	36	20	67	67
P-ST-W	31	24	87	77
S	43	12	59	64
SBZ	35	21	72	73
S-D	43	9	47	47
W	35	19	72	63
W-A	49	19	62	64
W-BTS	47	6	65	63
W-S	45	6	84	82
SBZ/BTS	39	14	69	64
D	3	46	10	10
Total	40	**19**	79	59

For the corrected Martinelli Model, only the plug and dispersed flow regimes, which were already well predicted by the model, had a loss in accuracy. The corrected

Martinelli Model more accurately predicts all other flow regimes. The Olujic model improves from 79% to 59% total error, with the mist flow regime showing the greatest improvement (311% to 46%). Several flow regimes experience a small decrease in accuracy, with the biggest decrease of 5% occurring for slug flow. Overall, the Olujic model is also improved by applying only the beta region model to all data; however, the model still performs with less accuracy than the Chisholm and Martinelli models.

In summary, it can be concluded that the Chisholm model and Martinelli model are the best choices for predicting frictional pressure drop. If the Martinelli model is corrected, the prediction accuracy greatly improves; however, the corrected model may only apply to the current air-oil test facility. Using the model for another two-phase system may result in significant prediction errors, as has been shown with other corrected models in the literature (Hetsroni, 1982; Ferguson and Spedding, 1995).

An alternative and potentially more effective approach would be the use of the Chisholm and uncorrected Martinelli models based on flow regime. Combination of pressure drop prediction with some flow regime determination factor, perhaps void fraction, could result in a more accurate prediction model. This approach has been suggested but not attempted in the literature (Ferguson and Spedding, 1995; Levy, 1999). One possible method would be to use the capacitance sensor flow regime identification technique discussed in Chapter Five to determine the appropriate pressure drop model. If a flow regime that is well predicted by the Chisholm model (for example slug building zone regime) is identified, the model would be applied. Similarly, if a flow regime well predicted by the Martinelli model is identified, then that model would be used. Taking

wavy flow as an example, the Chisholm model predicts the flow regime with an error of 76%. Comparing this value to the Martinelli model prediction for wavy flow of 35% suggests the Martinelli model would be the choice for wavy flow. If the corrected Martinelli model is used, the prediction for wavy flow improves to 19%. Unfortunately, as mentioned previously, the corrected Martinelli model may only predict well for the specific two-phase test facility used in this research. Since initial results are promising, it is recommended that more research be conducted on linking flow regime identification to pressure drop prediction models.

7.6 Mist Flow Regime Pressure Drop Models

One flow regime that is commonly encountered in industry, but has been largely ignored in previous investigations, is the mist flow regime (George et. al., 1991; Schrama, 1993). The Chang and Tremblay (1976) model, which was specifically developed for the mist flow regime, was also evaluated using the current mist flow data. Table 7.5 summarizes the RMSE for the five models, while Figure 7.14 illustrates the predictive trends. In the case of the Olujic model, the corrected form of the model has been applied. For the Martinelli model, both the original and corrected results are shown.

Table 7.5: Mist Flow Regime Prediction Error Results

Model	R.M.S.E.%
Homog.	42
Martinelli	57
Chisholm	39
C&T	49
Martinelli2	21
Olujic2	46

The offset data point observed in all flow regimes represents the highest air density recorded in the test section (Figure 7.14).

Without any correction, the Chisholm model has the lowest prediction error (39%), however it is clear from Figure 7.14 that the Martinelli model has the most consistent prediction trend. The corrected Martinelli model has the lowest overall prediction error (21%), as expected. Both the homogenous and Chang and Tremblay models are designed to predict the mist flow regime accurately, however average errors of 42% and 49% respectively, are less than expected. The homogenous model consistently under-predicts the pressure drop, while the Chang and Tremblay model consistently over-predicts. In the case of the Chang and Tremblay model, however, the original results had a general over-prediction of 22% (Chang and Tremblay, 1976), so the current over-prediction of 28% is consistent (Figure 7.15). Based on the very limited data available for the mist flow regime, the corrected Martinelli or Chisholm model are recommended.
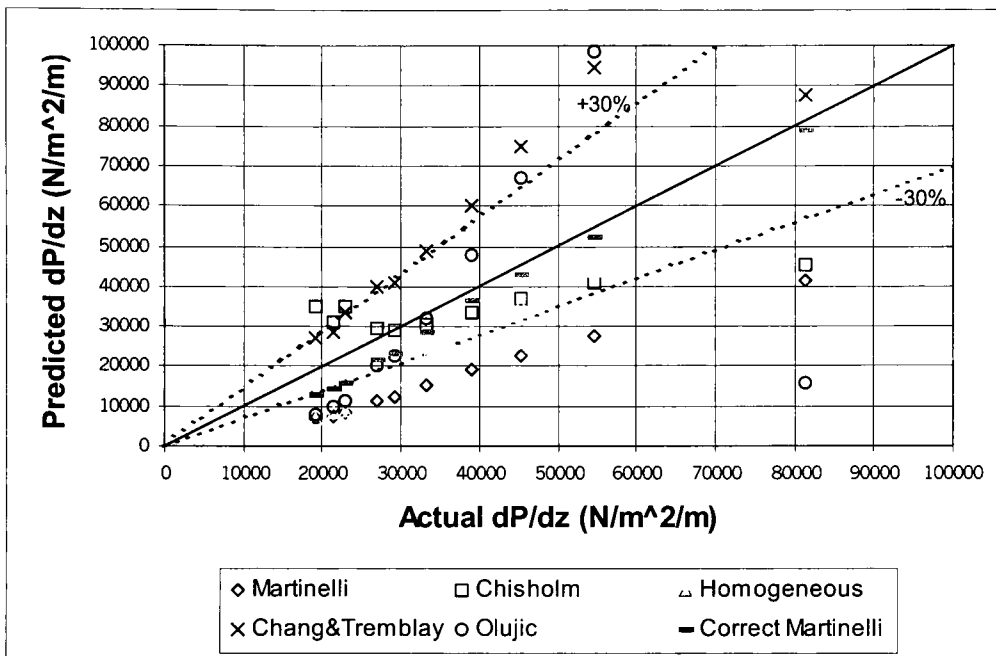
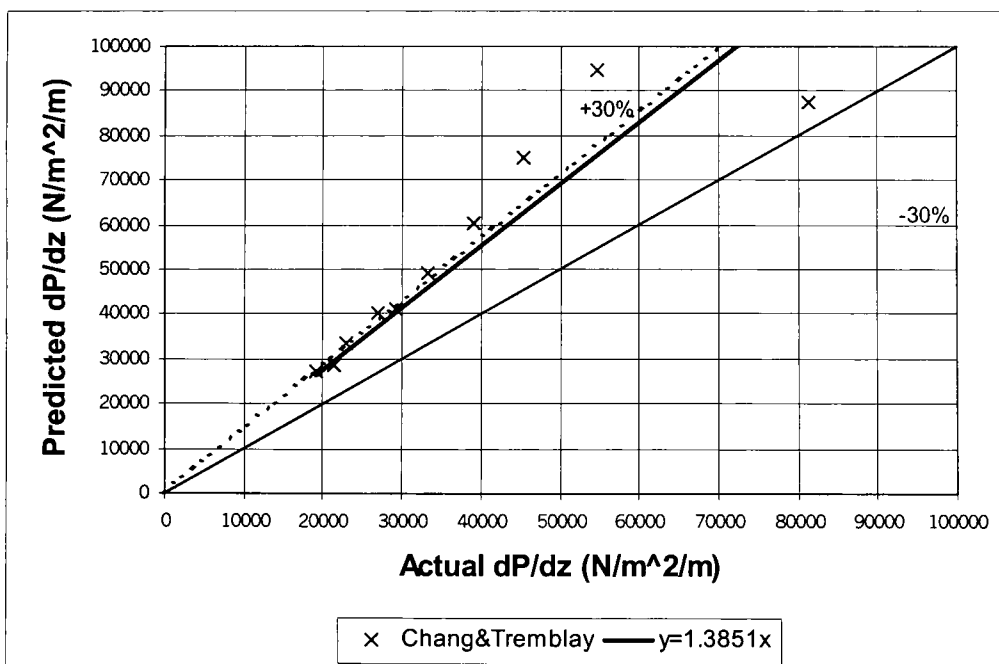Figure 7.14: Mist Flow Regime - Comparison Of Pressure Drop Models

Figure 7.15: Chang and Tremblay Model Trendline

Chapter Eight: Conclusions And Recommendations

The overall goal of this thesis was to gain a better understanding of air-oil two-phase flow in a horizontal straight pipe in order to improve flow regime identification techniques and pressure drop prediction models. This chapter presents a summary of the work completed, draws conclusions based on the current findings for the key objectives, and recommends directions for future work.

8.1 Conclusions

Previous two-phase flow research indicates a need for a detailed investigation of air-oil two-phase flow. Application of possible findings to several areas of industry, in particular lubrication technology using oil mist, provided motivation for the current research. A new air-oil two-phase flow test facility was designed and commissioned as a first step towards achieving the overall goal of the research. The current air-oil mixer and test section designs were found to provide reliable, repeatable results for pressure drop and flow regime conditions. Two air-oil mixer designs were evaluated and the results indicated there is a small relationship between the method of mixing chosen and the flow conditions achieved.

A ring-type capacitance sensor was designed and developed for measuring the instantaneous void fraction of the two-phase flow. The capacitance sensor signal was also used to obtain useful information about the nature of the flow, and to develop methods for flow regime identification. Specifically, the mean, variance, power spectral

114

density, and probability distribution function were found to provide criteria upon which a flow regime identification algorithm could be based.

As a second component of developing flow regime identification techniques, three flow maps: Mandhane et. al. (1974), Taitel and Dukler (1976), and Spedding and Nguyen (1980), were evaluated for the current data. Using the original forms of the maps, the corrections to the transitional boundaries in order to accurately predict air-oil two-phase flow regimes were identified. The Taitel and Dukler (1976) flow regime map produced the highest accuracy (53 %) of prediction for the uncorrected maps. Where possible, recommended physical property corrections were applied to the transitional boundaries, and the corrected maps re-evaluated. An overall decrease in the accuracy of the Mandhane et. al. (1974) map was noted when the recommended physical property corrections were applied to the transition boundaries. Alternative forms for the physical property corrections were then examined, and new forms presented that improved the prediction accuracy of the map from 50 to 75%.

The ability of four pressure drop models: Homogenous, Martinelli (1948), Chisholm (1973), and Olujic (1985), to predict the frictional pressure drop in horizontal pipes were evaluated. Of the four models, the Chisholm and Martinelli were found to provide the most accurate predictions (35% and 40% RMSE overall). Additionally, the Martinelli model was found to have the smallest data scatter along one trendline, allowing for the application of a simple correction factor to the model. The resulting correction improved the model to 19% RMSE. As an alternative to a simple correction factor, the fact that the Chisholm and uncorrected Martinelli models provide the most

accurate predictions for all identified flow regimes was used to suggest a more comprehensive approach to pressure drop prediction. By using flow regime identification techniques, a set of criteria could be developed for selection of the most accurate model for each particular flow regime.

In addition to the four frictional pressure drop models, a fifth model Chang and Tremblay (1976) specifically developed for mist flow was evaluated for prediction of the frictional pressure drop in the regime. Of the five models, the Chisholm model was found to have the most accurate predictions (39% RMSE). The Martinelli and Homogeneous models were both observed to have very small data scatter. Applying the corrected Martinelli model resulted in a 29% RMSE, which was the highest observed accuracy. The Chang and Tremblay model was found to have the second smallest prediction accuracy (49% RMSE), which is much lower than the reported 15% RMSE found by Chang and Tremblay (1976). Original test conditions used in the development of the Chang and Tremblay model were not reproduced in the data collection, however, preventing a full comparison of findings.

8.2 Recommendations

This thesis represents the first phase of a comprehensive air-oil two-phase flow research program at McMaster University. As such, there are a number of areas recommended for further study. The test facility can be used to continue studies on the existing horizontal test geometry or to conduct a study for a more complex geometry. Several key areas that should be further investigated as a follow up to this study are:

1) The development of objective flow regime identification techniques incorporating both the capacitance sensor signal processing tools and the flow regime maps.

2) Evaluation of additional frictional pressure drop models, and comparison of those models with the results of the Chisholm and Martinelli models.

3) Development of a pressure drop model that accounts for the flow regime effects.

4) Additional pressure drop data collection for the mist flow regime in order to extensively compare the prediction models. This may require the use of a mixer more capable of generating oil mist flow.

Application of a series of criteria based on the capacitance mean, variance, power spectral density, and probability density function to identify flow regimes appears promising. Extending the current flow regime data to include flow regimes not yet evaluated is necessary to continue the development of a flow regime identification algorithm. Linking the use of a flow regime map to the identification process will further strengthen the technique. The corrected Mandhane et. al.(1974) flow regime map proposed in this thesis is recommended for this purpose. Additional evaluation of the proposed flow regime transitional boundaries for the map is suggested. Using the results of the flow identification techniques to develop a comprehensive frictional pressure drop is also suggested.

Appendix A

Experimental Uncertainty Analysis

The multivariate Taylor Series method was used for the calculation of experimental uncertainties. For a given experimental result ER, the general uncertainty can be determined from:

$$\frac{U_{ER}}{ER} = \left[\left(\frac{\partial ER}{\partial Z_1} U_{x_1} \right)^2 + \left(\frac{\partial ER}{\partial Z_2} U_{x_2} \right)^2 + ... + \left(\frac{\partial ER}{\partial Z_i} U_{x_i} \right)^2 \right]^{0.5} \quad \text{A.1}$$

where $ER = f(Z_1, Z_2, ..., Z_i)$

The value U_x represents the uncertainty in any measured variable Z. If the uncertainty is for a measuring instrument, then U_x is calculated as:

$$U_x = \left[e_1^2 + e_2^2 \right]^{0.5} \quad \text{A.2}$$

where e_1^2 = interpolation error = $\pm\frac{1}{2}$ x Resolution

e_2^2 = instrument error

Example Calculation: Air Mass Flow Rate

$$m = \rho_{air} Q = \frac{PQ}{RT} \text{(kg/s)}$$

$$\frac{U_m}{m} = \left[(\frac{\partial m}{\partial Q} U_Q)^2 + (\frac{\partial m}{\partial P} U_P)^2 + (\frac{\partial m}{\partial T} U_T)^2 \right]^{0.5}$$

$$\frac{U_{\dot{m}}}{\dot{m}} = \left[(\frac{P}{RT}U_Q)^2 + (\frac{Q}{RT}U_P)^2 + (-\frac{PQ}{RT^2}U_T)^2 \right]^{0.5}$$

$U_Q = 7.34E - 05 \text{ m}^3/\text{s}$ $Q = 4.64E - 03 \text{ m}^3/\text{s}$

$U_P = 5 \text{ kPa}_{\text{gauge}}$ $P = 72 \text{ kPa}_{\text{gauge}}$

$U_T = 1.4 \text{ K}$ $T = 293 \text{ K}$

$\therefore U_{\dot{m}} = 7.1\%$

REFERENCE

Abdul-Razzak, A., Shoukri, M, and Chang, J.S. 1995. "Characteristics of Refrigerant R-134A Liquid-Vapor Two-Phase Flow In A Horizontal Pipe". ASHRAE Transactions 101:1-13.

Andritsos, N. 1989. "Effect of Liquid Viscosity on The Stratified-Slug Transition in Horizontal Pipe Flow". Int. Journal of Multiphase Flow. 15:877-897.

Baker, A., Nielson, K., and Gabb, A. 1988. "Pressure loss, liquid holdup calculations developed". Oil and Gas Journal. 86. March 14:55-59, March 21:78-86, March 28:44-48.

Baker, O. 1954. "Simultaneous Flow of Oil and Gas". Oil Gas Journal, July. 53:185-195.

Barnea, D., Shoham, O., Taitel, Y., and Dukler, A.E. 1979. "Flow Pattern Transition for Gas-Liquid Flow in Horizontal and Inclined Pipes: Comparison of Experimental Data With Theory". Int. Journal of Multiphase Flow. 5:217-225.

Baroczy, C.J. 1965. "A Systematic Correlation for Two Phase Pressure Drop". Chemical Engineering Progress Symposium Service. 62:232-249.

Chang, J.S., Myint, T.A., Donevski, B., Berezin, A.A., Irons, G.A., and Lu, W.K. 1985. "Determination of The Interfacial Parameters in Gas-Solid Two-Phase Pipe Flow By Capacitance Transducers". Particulate and Multiphase Processes-Colloidal and Interfacial Phenomena. Ariman, T. and Nejat Veziroglu, T. eds. Hemisphere Publishing Corporation. 173-287.

Chang, M.A. and Tremblay, I. 1976. "Two-Phase Flow for a Turbine Engine Scavenge System". United Technologies: PWC Engineering Report 848, June.

Chen, X., and Guo, L. 1999. "Flow patterns and pressure drop in oil-air-water three-phase flow through helically coiled tubes". Int. Journal of Multiphase Flow. 25:1053-1072.

Chisholm, D. 1967. "A Theoretical Basis for The Lockhart-Martinelli Correlation for Two-Phase Flow". Int. Journal of Heat and Mass Transfer. 10:1767-1778.

Chisholm, D. 1972. "An Equation For Velocity Ratio in Two-Phase Flow". NEL Report 535.

Chisholm, D. 1973. "Pressure Gradients Due to Friction During The Flow of Evaporating Two-Phase Mixtures in Smooth Tubes and Channels". Int. Journal of Heat and Mass Transfer. 16:347-348.

Cotton, J., Abdul-Razzak, A., Shoukri, M., and Richter, M. 1997. "Pressure drop during two-phase flow of R-134a in a horizontal tube". Internal Paper - Department of Mechanical Engineering, McMaster Uninversity.

Dukler, A.E., Wicks, M, and Cleveland, R.G. 1964. "Frictional Pressure Drop in Two-Phase Flow: An Approach Through Similarity Analysis". A.I.Ch.E. Journal, January. 10:1:44:51.

Dukler, A.E., Wicks, M., and Cleveland, R.G. 1964. "Pressure Drop and Hold-up in Two-Phase Flow". AIChE Journal. 10:2:38-51.

Ferguson, M.E.G. and Spedding, P.L. 1995. "Measurement and Prediction of Pressure Drop in Two-Phase Flow". Journal of Chemical Technology and Biotechnology. 62:262-278.

Friedel, L. 1979. "Improved Friction Pressure Drop Correlations for Horizontal and Vertical Two Phase Pipe Flow". European Two Phase Flow Group Meet., Ispra, Italy, paper E2.

Friedel, L. 1980. "Pressure Drop During Gas-Liquid Flow in Pipes". Int. Chemical Engineering. 20:3:352-367.

George, C.M., Poulikakos, D. and Boman, J. 1991. "High Speed Flow of Air-Oil Mixtures in Converging-Diverging Ducts". Int. Communications in Heat and Mass Transfer, May. 18:3:361-372

Glahn, A., and Wittig, S. 1996. "Two-Phase Air/Oil Flow in Aero Engine Bearing Chambers: Characterization of Oil Film Flows". Transactions of the ASME, July. 118:578-583.

Glahn, A., Kurreck, M., Willmann, M., and Wittig, S. 1996."Feasibility Study on Oil Droplet Flow Investigations Inside Aero Engine Bearing Chambers – PDPA Techniques in Combination With Numerical Approaches". Journal of Engineering for Gas Turbines and Power, October. 118:749-755.

Glovier, G.W. and Aziz, K. 1972. The Flow of Complex Mixtures in Pipes. New York: Van Nostrand-Reinhold.

Hand, N.P., and Spedding, P.L. 1993. "Horizontal Gas-Liquid Flow At Close To Atmospheric Conditions". Chemical Engineering Science. 48:12:2283-2305.

Harvel, G.D., Hori, K., Kawanishi, K., and Chang, J.S. 1999. "Cross-Sectional Void Fraction Distribution Measurements in a Vertical Annulus Two-Phase Flow by High Speed X-ray Computed Tomography and Real-Time Neutron Radiography Techniques". Flow Measurement and Instrumentation. 10:259-226.

Herm-Stapelberg, H., and Mewes, D. 1994. "Pressure drop calculation in three-phase slug flow of water, oil and air". Int. Chemical Engineering Journal, July. 34:3:295-314.

Hetsroni, G. 1982. The Handbook of Multiphase Flow. Toronto: McGraw-Hill Book Company.

Hubbard, M.G. and Dukler, A.E. 1966. "The Characterization of Flow Regimes for Horizontal Two-Phase Flow: I. Statistical Analysis of Wall Pressure Fluctuations". Proc. Heat Transfer and Fluid Mechanics Institute. 385-400.

Jones, A.B. and Zuber, N. 1975. "The Interrelation Between Void Functions Fluctuation and Flow Patterns in Two-Phase Flow". Int. Journal of Multiphase Flow. 2:273-306.

Levy, S. 1999. Two-Phase Flow in Complex Systems. Toronto: John Wiley & Sons, Inc. 2nd ED.

Lin, P. and Hanratty, T. 1987. "Effect of Pipe Diameter on Flow Patterns for Air-Water Flow in Horizontal Pipes". Int. Journal of Multiphase Flow. 13:4:549-563.

Lockhart, R.W., and Martinelli, R.C. 1949. "Proposed Correlation of Data for Isothermal Two-Phase, Two-Component Flow in Pipes". Chemical Engineering Progress. 45:39-48.

Lowe, D. and Rezkallah, S. 1999. "A capacitance sensor for the characterization of microgravity two-phase liquid-gas flow". Measurement Science Technology. 10:965-975.

Mandhane, J.M., Gregory, G.A., and Aziz, K. 1974. "A Flow Pattern Map for Gas-Liquid Flow in Horizontal Pipes". Int. Journal of Multiphase Flow. 1:537-553.

Martinelli, R.C. and Nelson, D.B. 1948. "Prediction of Pressure Drop During Forced-Circulation Boiling of Water". Trans. ASME. 70:695-702.

McAdams, W.H., Woods, W.K., and Heroman, L.C. 1942. "Vaporization inside Horizontal Tubes, 2: Benzene-Oil Mixtures". Trans. ASME. 64:193-200.

Moussalli, G. and Chawla, J. 1976. Forsch. Ing. Wes. 42:149-153.

Nadler, M., and Mewes, D. 1996. "Effects of The Liquid Viscosity on The Phase Distributions in Horizontal Gas-Liquid Slug Flow". Int. Journal of Multiphase Flow. 21:2:253-266.

Nicholson, M.K., Aziz, K., and Gregory, G.A. 1978. "Intermittent Two-Phase Flow in Horizontal Pipes: Predictive Models". Canadian Journal of Chemical Engineering, December. 56:653-663.

Olujic, Z. 1985. "Predicting Two-Phase Flow Friction Loss in Horizontal Pipes". Chemical Engineering, June 1985. 45-50.

Olujic, Z. and Chawla, J. 1979. Kem. Ind. (Zargreb). 28:305-312.

Ramkrishna, D., and Pattanayak, S. 1994. "Measurement of void fraction in different flow regimes of a vertical gas-liquid flow through narrow tubes". Measurement Science and Technology, December. 5:12:1538-1545.

Rouhani, S.Z., and Sohal, M.S. 1983. "Two-Phase Flow Patterns: A Review of Research Results". Progress in Nuclear Energy. 11:3:219-259.

Schrama, R.C. 1993. "Oil Mist vs. Air-Oil for Consumable Lubrications Systems". Lubrication Engineering, January. 49:1:9-17.

Spedding, P.L. and Nguyen, V.T. 1980. "Regime Maps for Air-Water Two-Phase Flow". Chemical Engineering Science. 35:779-793.

Spedding, P. and Spence, D. 1993. "Flow Regimes in Two-Phase Gas-Liquid Flow". Int. Journal of Multiphase Flow. 19:2:245-280.

Souza, A.L., Chato, J.C., Wattelet, J.P, and Christoffersen, B.R. 1993. "Pressure Drop During Two-Phase Flow of Pure Refrigerants and Refrigerant-Oil Mixtures in Horizontal Smooth Tubes". Heat Transfer With Alternative Refrigerants, ASME. HTD-243:35-41.

Taitel, Y. and Dukler, A.E. 1976. "A Model for Predicting Flow Regime Transitions in Horizontal and Near Horizontal Gas-Liquid Flow". AIChE Journal. 22:1:47-55.

Taitel, Y. and Dukler, A.E. 1987. "Effect of Pipe Length on The Transition Boundaries for High-Viscosity Liquids". Int. Journal of Multiphase Flow. 13:4:577-581.

Weisman, J., Duncan, D., Gibson, J., and Crawford, T. 1979. "Effects of Fluid Properties and Pipe Diameter on Two-Phase Flow Patterns in Horizontal Lines". Int. Journal of Multiphase Flow. 5:437-462.

Whalley, P.B. 1990. Boiling Condensation and Gas-Liquid Flow. Oxford: Clarendon Press.

Xie, C.G., Plaskowski, A.B., and Beck, M.S. 1989. "Eight-Electrode Capacitance System For Two-Component Flow Identification". IEE Proceedings Pt. A. 184-190.